Title
Nitrous Acid Chemistry in Two Polluted Environments: Urban Boundary Layers and Biomass Burning Plumes

Author
Tuite, Kathleen

Publication Date
2022

Peer reviewed|Thesis/dissertation

UNIVERSITY OF CALIFORNIA

Los Angeles

Nitrous Acid Chemistry in Two Polluted Environments: Urban Boundary Layers and Biomass Burning Plumes

A dissertation submitted in partial satisfaction
of the requirements for the degree
Doctor of Philosophy in Atmospheric and Oceanic Sciences

by

Kathleen Barbara Tuite

2022

ABSTRACT OF THE DISSERTATION

Nitrous Acid Chemistry in Two Polluted Environments: Urban Boundary Layers and Biomass Burning Plumes

by

Kathleen Barbara Tuite
Doctor of Philosophy in Atmospheric and Oceanic Sciences
University of California, Los Angeles, 2022
Professor Jochen Peter Stutz, Chair

Nitrous acid (HONO) is an important radical precursor that can influence secondary pollutant levels, especially in areas impacted by urban emissions and wildfire smoke. Due to uncertainties in its emissions and heterogeneous formation mechanisms, models often under predict HONO concentrations. A number of heterogeneous sources at the ground and on aerosols have been proposed but there is no consensus about which play a significant role in these polluted environments. In this thesis, a new one-dimensional chemistry and transport model (PACT-1D) is used to interpret field measurements and analyze the HONO budget. PACT-1D performs surface chemistry based on molecular collisions and chemical conversion, allowing the addition of detailed HONO formation chemistry at the ground and on particles.

Model runs were conducted for the 2010 CalNex campaign, finding good agreement with observations of key species such as O_3, NO_x, and HO_x. With the ground sources implemented, the model captures the diurnal and vertical profile of the HONO observations. Primary HO_x production from HONO photolysis is 2-3 times more important than O_3 or HCHO photolysis at mid-day, below 10 m. The HONO concentration, and its contribution

to HO_x, decreases quickly with altitude. Heterogeneous chemistry at the ground provided a HONO source of 2.5x10 ^{11} molecules $cm^{-2}\,s^{-1}$ during the day and 5x10 ^{10} molecules $cm^{-2}\,s^{-1}$ at night. The night time source was dominated by NO_2 hydrolysis. During the day, photolysis of surface HNO_3/nitrate contributed 45-60% and photo-enhanced conversion of NO_2 contributed 20-45%. Sensitivity studies addressing the uncertainties in both photolytic mechanisms show that, while the relative contribution of either source can vary, HNO_3/nitrate is required to produce a surface HONO source that is strong enough to explain observations.

Two wildfire smoke plumes from the 2019 FIREX-AQ experiment were also successfully simulated. Both plumes show high levels of HONO, with concentrations exceeding 20 ppb in young smoke. PACT-1D captures the rapid decay of HONO with smoke age, due to a mix of chemical loss and dilution. Vertical profiles show highest levels in the plume center that quickly decrease towards the plume top and bottom. The decrease occurs more rapidly than less-reactive species, creating a narrower vertical distribution of HONO. The large quantities of HONO emitted from fires provide the dominant source and result in HONO providing 80% of the total HO_x formation in young smoke. Sensitivity studies show that emissions also drive O_3 production, with O_3 levels reduced up to 10 ppb when HONO emissions are omitted. Low photolysis rates and minimal vertical mixing in the plumes allow these emissions to be transported hours downwind, continuing to provide a source of OH. HONO's contribution to the HO_x budget decreases as emissions are lost and by 6 hours downwind, HCHO photolysis becomes the dominant HO_x source. Secondary sources of HONO are minor compared to emissions but pNO_3 photolysis becomes significant in older smoke and helps HONO continue to contribute at least 5% to HO_x production.

The dissertation of Kathleen Barbara Tuite is approved.

Ann Marie Carlton

Pablo Saide Peralta

Suzanne E. Paulson

Jochen Peter Stutz, Committee Chair

University of California, Los Angeles

2022

TABLE OF CONTENTS

LIST OF FIGURES

LIST OF TABLES

ACKNOWLEDGMENTS

I would like to first express gratitude to my advisor, Dr. Jochen Stutz, for his guidance and support through my graduate study. His knowledge, patience, and constant scientific curiosity helped me grow as a researcher. I also thank my committee members, Dr. Suzanne Paulson, Dr. Pablo Saide, and Dr. Ann Marie Carlton for their suggestions and advice. The successful development of the model presented in this thesis would not have been possible without my collaborators, Dr. Jennie Thomas and Shaddy Ahmed. I appreciate the countless discussions, advice, and work they did over the years.

I would also like to acknowledge current and past members of my research group, Dr. Nathaniel Brockway, Dr. Fedele Colosimo, Zoe Pierrat, Sarah Johnson, James Yoon, Katie Harding, Dr. Catalina Tsai, Dr. Katja Grossman, and Dr. Ross Cheung. Their assistance with analysis and suggestions on presentations and papers helped advance my research and they provided great companionship during field campaigns. I thank the other students in the AOS Department and at UCLA who made my graduate years fulfilling. Finally, I am incredibly grateful to my parents, family, and friends for their nonstop love, patience, and encouragement. I especially thank my husband Dave for moving to California with me and standing by my side as a constant source of support.

VITA

2007–2011 BS in Chemistry, University of Pittsburgh

2015–2017 MS in Atmospheric and Oceanic Sciences, University of California, Los Angeles

2016-2017 Teaching Assistant, Atmospheric and Oceanic Sciences Department, University of California, Los Angeles

2016-2022 Graduate Student Researcher, Atmospheric and Oceanic Sciences Department, University of California, Los Angeles

PUBLICATIONS

S. Ahmed, J. L. Thomas, **K. Tuite**, J. Stutz, F. Flocke, J. J. Orlando, R. S. Hornbrook, E. C. Apel, L. K. Emmons, D. Helmig, P. Boylan, L. G. Huel, S. R. Hall, K. Ullmann, C. A. Cantrell, A. Fried. (2022). The Role of Snow in Controlling Halogen Chemistry and Boundary Layer Oxidation During Arctic Spring: A 1D Modeling Case Study. *Journal of Geophysical Research Atmospheres*, 127, e2021JD036140. https://doi.org/10.1029.2021JD036140.

K. Tuite, J. L. Thomas, P. R. Veres, J. M. Roberts, P. S. Stevens, S. M. Griffith, S Dusanter, J. H. Flynn, S. Ahmed, L. Emmons, S. Kim, R. Washenfelder, C. Young, C. Tsai, O. Pikelnaya, J. Stutz. (2021). Quantifying Nitrous Acid Formation and Mechanisms Using Measured Vertical Profiles During the CalNex 2010 Campaign and 1D Column Modeling. *Journal of Geophysical Research Atmospheres*, 126, e2021JD034689. https://doi.org/10.1029/2021JD034689.

L. Marelle, J. L. Thomas, S. Ahmed, **K. Tuite**, J. Stutz, A. Dommergue, W. R. Simpson, M. M. Frey, F. Baladima. (2021). Implementation and Impacts of Surface Blowing Snow Sources of Arctic Bromine Activation Within WRF-Chem 4.1.1. *Journal of Advances in Modeling Earth Systems*, 13, e2020MS002391. https://doi.org/10.1029/2020MS002391.

K. Tuite, N. Brockway, S. F. Colosimo, K. Grossmann, C. Tsai, J. Flynn, S. Alvarez, M. Erickson, G. Yarwood, U. Nopmongcol, J. Stutz. (2018). Iodine Catalyzed Ozone Destruction at the Texas Coast and Gulf of Mexico. *Geophysical Research Letters*, 45, 7800-7807. https://doi.org/10.1029/2018GL078267.

CHAPTER 1

Introduction and Background

1.1 Motivation

Secondary pollutants, which are formed chemically in the atmosphere, can have serious impacts on human health. Two of the most important secondary pollutants are ozone (O_3) and secondary organic aerosols (SOA), which are major components of photochemical smog. When inhaled, both can cause respiratory and/or cardiovascular problems and are associated with illnesses such as asthma and even increased mortality rates (Beelen et al., 2015; Brook et al., 2010; Fleming et al., 2018; Karanasiou et al., 2021; Landrigan et al., 2018; Lippmann, 1991). Although strict mitigation steps have resulted in significantly lower pollution levels in many regions throughout the United States, air quality standards are still often exceeded. Urban areas and regions downwind of wildfires are two examples of environments that regularly experience high concentrations of O_3 and SOA.

Large emissions of nitrogen oxides ($NO_x = NO_2 + NO$) and volatile organic compounds (VOCs) from urban sources and biomass burning (BB) are largely responsible for the high levels of pollution associated with these environments. Both NO_x and VOCs are precursors for O_3, which is formed through a series of chain reactions. NO_x is primarily emitted as NO which is converted to NO_2 through oxidation. NO_2 photolyzes to produce NO and atomic oxygen (O^3P) (Reaction 1.1), which can subsequently react with molecular oxygen (O_2) and form O_3 (Reaction 1.2). Since NO reacts with O_3 to reform NO_2 (Reaction 1.3) however, this cycle does not lead to an overall increase in O_3 concentrations.

$$NO_2 + h\nu \rightarrow NO + O(^3P) \tag{1.1}$$

$$O_2 + O(^3P) \xrightarrow{M} O_3 \tag{1.2}$$

$$NO + O_3 \rightarrow NO_2 + O_2 \tag{1.3}$$

When VOCs are present, though, their oxidation by the hydroxyl radical (OH) forms HO_2, which can convert NO to NO_2 without destroying O_3 (Figure 1.1). OH therefore plays a key role in net O_3 production in the troposphere. Additionally, the oxidation of VOCs by OH produces lower volatility species that can condense to form SOA, so OH is important in the formation of both pollutants.

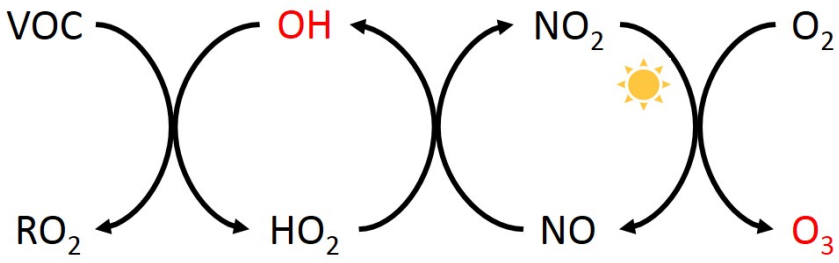

Figure 1.1: Schematic of tropospheric O_3 formation, highlighting the role of OH in the photochemical process.

Better predicting formation of these secondary pollutants consequently requires an understanding of how OH is formed. One important OH precursor relevant to urban regions and biomass burning is nitrous acid (HONO), which photolyzes to produce OH (Reaction 1.4).

$$HONO + h\nu(\lambda < 400nm) \rightarrow OH + NO \tag{1.4}$$

Since it was first measured in the atmosphere by Platt and Perner (1979), HONO has been

an important research topic. In urban areas, HONO photolysis can contribute up to 55% of daily primary OH production (Alicke et al., 2002, 2003; Kleffmann et al., 2005; Kleffmann, 2007; Ren et al., 2003; Volkamer et al., 2010; Young et al., 2012; Elshorbany et al., 2009; Mao et al., 2010), thus playing a significant role in both the oxidative chemistry of the atmosphere and secondary pollutant formation. Similarly, in early BB plume chemistry, HONO is also an important source of OH since it is directly emitted from wildfires and photolyzes more efficiently than other radical precursors (Trentmann et al., 2005; Alvarado and Prinn, 2009; Alvarado et al., 2009; Neuman et al., 2016; Peng et al., 2020). Correctly predicting pollutant levels in these environments therefore requires an accurate understanding of the HONO budget. However, there are still large uncertainties in HONO sources. This often leads to an underestimation of HONO concentrations in air quality models.

As government regulations in the United States become increasingly strict, more accurate air quality models are required to identify pollutant exceedances and guide future policy decisions. Mitigation steps have largely focused on reducing primary emissions from traditional mobile and point sources, many of which are located in or near urban regions. For example, the light duty vehicle NO_x emissions standard for 2025 is a 98% decrease compared to 1975 (https://www.epa.gov/greenvehicles/light-duty-vehicle-emissions). Despite these efforts, several cities, such as Los Angeles, have seen a stagnation in O_3 pollution decreases over the past decade (Figure 1.2). This is largely due to the complicated nonlinear relationship between O_3 production and concentrations of VOCs, radicals, and NO_x. Since HONO provides a source of radicals and NO_x (Reaction 1.4), a better description of its formation and chemistry in models will lead to more accurate predictions of future urban O_3 trends.

While great efforts have been made to reduce anthropogenic emissions, emissions from wildfires, particularly in the western United States, have increased in recent decades. The combination of warming temperatures and increased drought conditions due to climate change, along with forest management practices, have increased the size and frequency of wildfires (Westerling, 2016; McClure and Jaffe, 2018; Williams et al., 2019; Marlon et al.,

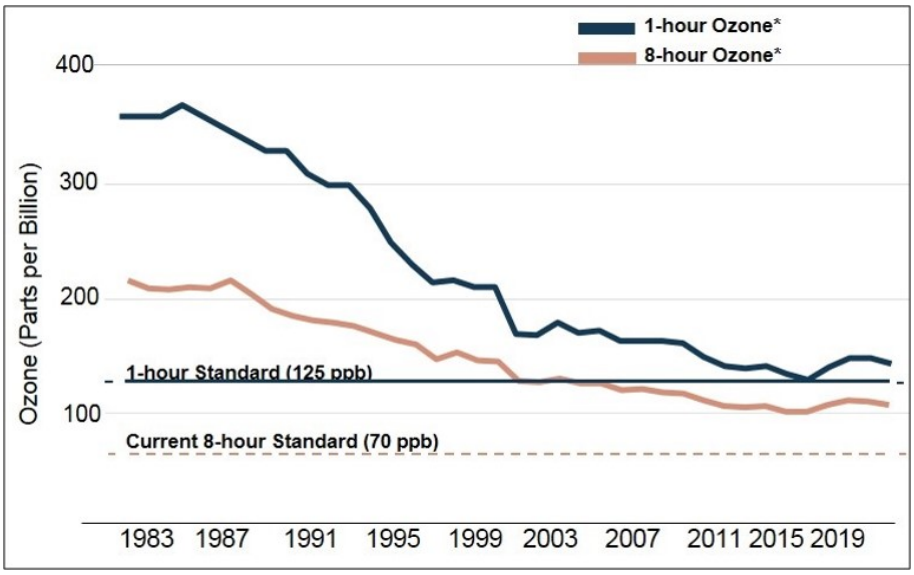

Figure 1.2: Trends in the average 1 hour and 8 hour O_3 mixing ratios in Los Angeles, CA over the past 4 decades. The plot shows significant O_3 decreases in earlier years and a leveling off recently. Figure from the South Coast Air Quality Management District (SCAQMD) Nov 2020 Board Meeting (http://www.aqmd.gov/docs/default-source/Agendas/Governing-Board/2020/2020-nov6-025.pdf

2012; Parks et al., 2015). Biomass burning is therefore becoming an increasingly important source of air pollution (Figure 1.3). The ability of smoke to travel far distances, especially if the plume is lofted into the free troposphere, means that wildfires influence air quality on a regional or even global scale.

Although substantial quantities of O_3 precursors are emitted from wildfires, there is considerable variability in O_3 production between plumes (Jaffe and Wigder, 2012; Robinson et al., 2021; Xu et al., 2021). Differences in fuel type, burning conditions, and plume dynamics make it difficult to predict downwind O_3 concentrations. Further complicating this is the limited understanding of HONO chemistry within smoke, which drives photochemistry in young plumes (Peng et al., 2020; Robinson et al., 2021). In particular, uncertainties in

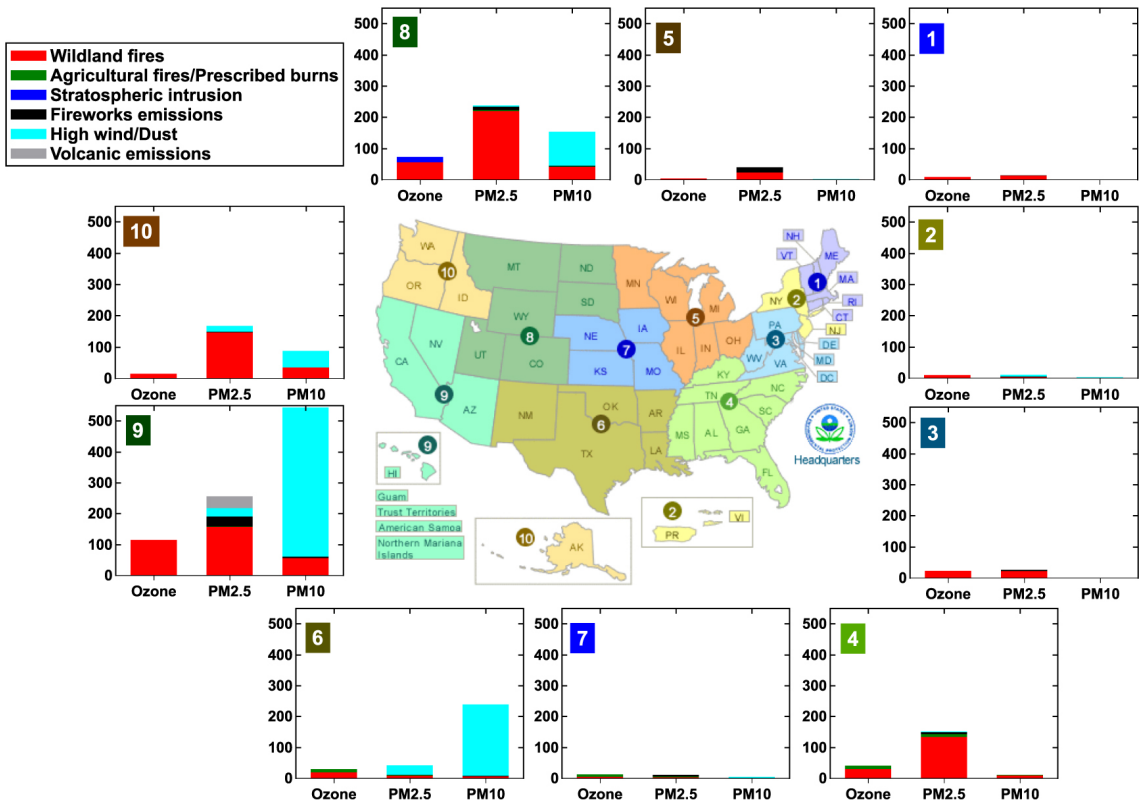

Figure 1.3: The center map shows 10 regions defined by the U.S. EPA. Surrounding plots show the number of days from 2000-2017 when the air quality standard was exceeded due to an exceptional event, with each color representing a different cause for the exceedance. In particular, wildland fires (in red) are a significant cause of poor air quality in the western U.S. Figure is from David et al. (2021).

HONO emissions and secondary production limit the ability to accurately predict O_3 and SOA formed from wildfires.

The goal of this thesis is to better quantify sources of HONO in these two polluted environments - the urban boundary layer and wildfire smoke plumes. By combining field measurements and modeling studies, the HONO chemical budget, including heterogeneous formation mechanisms and emissions, can be constrained more accurately. With a more complete understanding of HONO chemistry, these processes can be incorporated into regional

models that are used to study air quality trends and identify harmful pollution events.

1.2 Overview of HONO chemistry in urban regions

HONO chemistry includes homogeneous and heterogeneous reactions, biological processes, and direct emission from combustion sources (Figure 1.4).

1.2.1 Homogeneous chemistry

The main gas phase reactions include loss via photolysis (Reaction 1.4) and reaction with OH (Reaction 1.5), and production through the NO + OH reaction (Reaction 1.5). HONO photolysis occurs at higher wavelengths than other OH precursors (e.g., O_3 and HCHO), making it an especially important source in low light conditions, such as the early morning and in thick smoke plumes.

$$\mathrm{HONO} + \mathrm{OH} \rightarrow \mathrm{NO_2} + \mathrm{H_2O} \tag{1.5}$$

$$\mathrm{NO} + \mathrm{OH} \xrightarrow{M} \mathrm{HONO} \tag{1.6}$$

1.2.2 HONO trends in urban regions

In urban areas, HONO shows a consistent diurnal profile, with mixing ratios gradually increasing throughout the night and quickly decaying in the morning once photolysis becomes active. Nocturnal surface levels can reach several parts per billion (ppb) (Kleffmann et al., 2006; Stutz et al., 2010; Wong et al., 2011), while daytime levels have been reported up to a few hundred parts per trillion (ppt) (Acker et al., 2006; Kleffmann et al., 2005; Wong et al., 2012; Zhou et al., 2007). A strong HONO source is required to maintain these levels, particularly during the day when the HONO lifetime is only 10-20 minutes.

It was originally thought that HONO reached a pseudo-steady state (PSS) during the

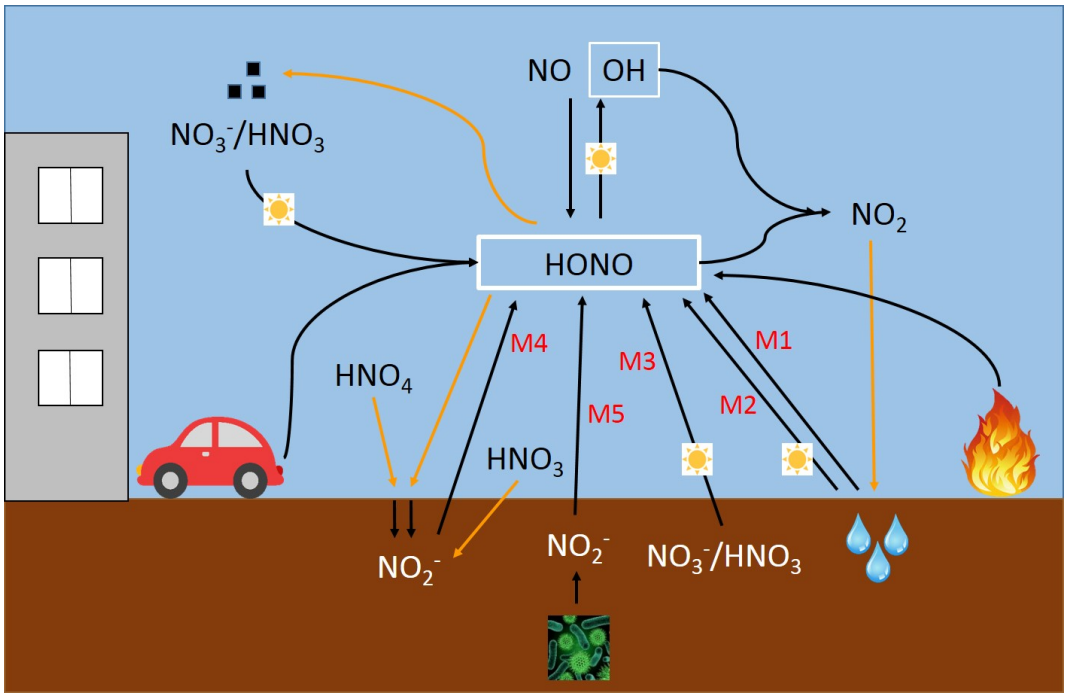

Figure 1.4: Cartoon of common HONO sources and sinks to the atmosphere. M1-5 in red indicate proposed surface source mechanisms.

day that was regulated by the gas phase reactions listed above (Reactions 1.4, 1.5, 1.6).

$$[HONO]_{SS} = \frac{k_{OH+NO}[NO][OH]}{j_{HONO} + k_{HONO+OH}[OH]} \tag{1.7}$$

Recent PSS calculations and models, however, show that HONO levels are greatly underestimated (by 10-100 times) when only homogeneous chemistry is considered (Zhou et al., 2002; Kleffmann et al., 2005; Kleffmann, 2007; Tsai et al., 2018; Sarwar et al., 2008; Li et al., 2011; Czader et al., 2012). HONO is directly emitted by anthropogenic combustion processes, but this is less than 1% of NO_x emissions (Kirchstetter et al., 1996; Kurtenbach et al., 2001; Neuman et al., 2016; Kramer et al., 2019) and cannot explain atmospheric levels either. Measured vertical profiles show HONO concentrations are greatest near the ground (Kleffmann et al., 2003; Villena et al., 2011; Wong et al., 2011, 2012; Vandenboer et al., 2013).

Since HONO is quickly lost during transport, this indicates a ground source is likely present. Multiple heterogeneous formation mechanisms have therefore been proposed to explain this missing HONO source.

1.2.3 Heterogeneous chemistry

Laboratory studies have found that HONO is produced from NO_2 conversion on humid surfaces (M1 in Figure 1.4), following a reaction mechanism (Reaction 1.8) which is first order with respect to both NO_2 and water vapor (Sakamaki et al., 1983; Svensson et al., 1987; Pitts et al., 1984; Jenkin et al., 1988; Lammel and Cape, 1996).

$$2NO_2 + H_2O \xrightarrow{surface} HONO + HNO_3 \tag{1.8}$$

There is significant evidence that this reaction is the main source of nocturnal HONO and allows for an accurate description of HONO mixing ratios and $HONO/NO_2$ ratios at night (Alicke et al., 2003; Kleffmann et al., 2003; Wong et al., 2011; Vandenboer et al., 2013). While Reaction 1.8 occurs during the day as well, it does not produce HONO at the rate needed to sustain daytime levels and many studies have shown evidence that a photolytic source is required (Alicke et al., 2002; Kleffmann et al., 2005; Acker et al., 2006; Wong et al., 2012).

Photo-enhanced heterogeneous conversion of NO_2 to HONO (M2 in Figure 1.4) has been found to occur on a variety of surfaces, including soot (Ammann et al., 1998; Aubin and Abbatt, 2007; Khalizov et al., 2010; Monge et al., 2010), humic acid (Stemmler et al., 2006, 2007; Bartels-Rausch et al., 2010), and organic films (Gutzwiller et al., 2002; George et al., 2005; Brigante et al., 2008). A mechanism proposed by Stemmler et al. (2006) suggests HONO formation from NO_2 conversion on humic acid surfaces is first order in NO_2 and linearly dependent on irradiance and surface area (SA).

$$P_{HONO} \propto SA \times [NO_2] \times irradiance \tag{1.9}$$

Multiple studies suggest that this conversion provides a major daytime source, showing that HONO correlates with NO_2 levels and/or NO_2 photolysis rates (Vogel et al., 2003; Wong et al., 2012, 2013; Laufs et al., 2017; Tsai et al., 2018).

Another daytime HONO source is the photolysis of surface adsorbed HNO_3/nitrate (M3 in Figure 1.4), which proceeds at a rate 1-4 orders of magnitude faster than gas phase or aqueous HNO_3 photolysis (Zhou et al., 2002, 2003; Ramazan et al., 2004; Baergen and Donaldson, 2013, 2016; Ye et al., 2016, 2019). Reactions 1.10 - 1.14 describe the mechanism proposed by Zhou et al. (2002). NO_2 in Reaction 1.12 is the dominant product over Reaction 1.11 in the actinic region of solar radiation. However, Reaction 1.12 further converts som adsorbed NO_2 into HONO. In Reaction 1.14, surface HONO desorbs into the gas phase.

$$\mathrm{HNO_{3(ads)}} + h\nu \rightarrow \mathrm{[HNO_3]^*_{(ads)}} \tag{1.10}$$

$$\mathrm{[HNO_3]^*_{(ads)}} \rightarrow \mathrm{HONO_{(ads)}} + \mathrm{O(^3P)_{(ads)}} \tag{1.11}$$

$$\mathrm{[HNO_3]^*_{(ads)}} \rightarrow \mathrm{NO_{2(ads)}} + \mathrm{OH} \tag{1.12}$$

$$\mathrm{NO_{2(ads)}} + \mathrm{H_2O_{(ads)}} \rightarrow \mathrm{HONO_{(ads)}} + \mathrm{HNO_{3(ads)}} \tag{1.13}$$

$$\mathrm{HONO_{(ads)}} \rightarrow \mathrm{HONO_{(g)}} \tag{1.14}$$

This mechanism has been shown to be important in low NO_x forested environments (Zhou et al., 2011; Zhang et al., 2012). Although photo-enhanced conversion of NO_2 is often considered the dominant HONO formation pathway in high NO_x areas, HNO_3 photolysis has also been confirmed as a significant source in the urban regions near Philadelphia (Sarwar et al., 2008) and Houston (Karamchandani et al., 2014). Enhanced photolysis is known to

occur on glass (Zhou et al., 2002; Ye et al., 2019), building materials (Ye et al., 2016), and urban grime (Baergen and Donaldson, 2013, 2016), indicating that this mechanism likely plays a role in urban HONO production.

Both of these proposed photolytic mechanisms can occur on aerosols in addition to the ground. Due to the much smaller aerosol surface area, however, and deactivation of reactive sites during aging, the aerosol source is considered minor in comparison under most conditions (Kalberer et al., 1999; Kleffmann et al., 2003; Vogel et al., 2003; Stemmler et al., 2007). This may not be true for heavily polluted environments though with high aerosol concentrations. Studies of extreme urban pollution events (Li et al., 2011; Ye et al., 2018), power plant plumes (Ye et al., 2018), and biomass burning plumes (Trentmann et al., 2005; Alvarado and Prinn, 2009; Alvarado et al., 2009) indicate that aerosol sources are needed to explain HONO and O_3 levels.

A recent HONO source proposed by Vandenboer et al. (2013) is the displacement of surface nitrite by strong atmospheric acids like HCl and HNO_3 (M4 in Figure 1.4). Throughout the night, the primary HONO sink is deposition to the surface, where it can react with carbonate material to form nitrite.

$$MCO_{3(s)} + 2HONO_{(g)} \rightarrow MNO_2 + CO_2 + H_2O \tag{1.15}$$

This nocturnally deposited HONO may form a surface reservoir that can be released the following day. Laboratory studies suggest that HCl and HNO_3 can displace surface nitrite with an efficiency of 1-20%, with 9% as the mean (Vandenboer et al., 2015).

Biological processes in soil provide another potential atmospheric HONO source (M5 in Figure 1.4) (Su et al., 2011; Oswald et al., 2013; Maljanen et al., 2013; Scharko et al., 2015; Meusel et al., 2018). Nitrification and denitrification produce nitrite, which undergoes acid-base reactions and partitioning between air and the aqueous phase in soil.

$$NO_2{}^-{}_{(aq)} + H^+_{(aq)} \rightarrow HONO_{(aq)} \rightarrow HONO_{(g)} \tag{1.16}$$

Reaction 1.16 depends on the pH and $NO_2{}^-$ concentration of the soil. Oswald et al. (2013) performed laboratory studies comparing HONO and NO soil emissions from a variety of ecosystems. They found that HONO can contribute up to 50% of the total reactive nitrogen released from soil, especially in arid and arable soils with water content below 20% water holding capacity.

Although HONO has been studied for many years, there is still no consensus about which of the proposed heterogeneous mechanisms play a significant role under varying environmental conditions. More research is therefore needed to quantify these sources in urban areas and to better understand HONO's overall impact to air quality.

1.3 Overview of HONO chemistry in biomass burning plumes

1.3.1 Trace gas quantification in smoke

As fire burns fuel, large quantities of heat, gases, and particles are emitted in a plume of smoke that rises and disperses. Since smoke mixes with background air as it moves away from the burning location, trace gas concentrations are often reported as normalized excess mixing rations (NEMRs). The trace gas amount is normalized against a relatively non-reactive tracer (usually carbon monoxide, CO), which helps distinguish if concentration changes are due to chemistry or dilution.

$$NEMR_X = \frac{\Delta X}{\Delta CO} = \frac{X_{smoke} - X_{bkgrd}}{CO_{smoke} - CO_{bkgrd}} \tag{1.17}$$

X_{smoke} and X_{bkgrd} represent the mixing ratios of trace gas X inside and outside of the plume, respectively. When measurements are taken close enough to the fire, ideally before significant chemistry has occurred, NEMRs are called emission ratios (ERs) and are used to quantify emissions. Emissions can also be reported as an emission factor (EF), which is the amount of a trace gas emitted per kilogram of dry fuel burned.

$$EF_X = \frac{\Delta \mathrm{X}}{\Delta(\mathrm{CO} + \mathrm{CO_2})} \times \frac{MW_X}{MW_C} \times F_C \tag{1.18}$$

MW is the molecular weight of trace gas X and carbon (12 g/mol) and F_C is the fraction of carbon in the burned fuel (typically 0.45 - 0.5).

The burning temperature of the fire has a significant impact on the break down of fuel into gas phase molecules and particles. The modified combustion efficiency (MCE) is used to describe how efficiently, i.e. how hot, a fire is burning.

$$MCE = \frac{\Delta \mathrm{CO_2}}{\Delta(\mathrm{CO} + \mathrm{CO_2})} \tag{1.19}$$

High temperatures lead to flaming fires that burn more efficiently and produce a higher ratio of CO_2 versus CO. Purely flaming fires have an MCE close to 0.99. Smoldering fires are a result of lower temperatures and have lower MCE values, anywhere between 0.65-0.85 but typically near 0.8 for pure smoldering (Akagi et al., 2011; Andreae, 2019). For many trace gases, there is a good correlation between MCE and emissions. For example, CO_2, shorter chain VOCs, NO_x, and black carbon have higher emissions at high MCE, whereas CO, longer chain VOCs (with lower volatility), and NH_3 are emitted at lower MCE (Andreae, 2019; Sekimoto et al., 2018).

1.3.2 HONO emissions

Biomass burning emissions of reactive nitrogen species, including HONO, depend on the fuel nitrogen content and temperature. Pyrolysis of the fuel produces small molecules such as hydrogen cyanide (HCN), isocyanic acid (HNCO), and ammonia (NH_3), which are converted to N_2, N_2O, NO, NO_2, and HONO through radical flame chemistry (Roberts et al., 2020; Lobert and Warnatz, 1993; Glarborg et al., 2018). In addition to fuel N content, fuel moisture and combustion conditions (i.e., flaming versus smoldering) also impact N emissions. Generally, NO_x and NH_3 are most strongly correlated with MCE. NO_x is primarily a flaming combustion product, increasing nonlinearly with MCE, whereas NH_3 is emitted in smoldering fires and decreases linearly with MCE.

HONO shows a more interesting relationship. Similar to NO_x, HONO emissions occur in the flaming stage and increase with MCE. The chemistry that produces HONO, however, is less efficient at very high temperatures so emissions start to decay slightly at MCE values above 0.95 (Roberts et al., 2020). Burling et al. (2010) also found that HONO emissions correlate more strongly with MCE when normalized against fuel N content. A recent analysis of global satellite data found a strong dependence between HONO emissions and vegetation type, emphasizing the importance of fuel (Theys et al., 2020). Because of this, HONO emissions are often reported normalized to NO_x in addition to CO.

Laboratory and field studies report a wide range of HONO emission ratios, with $ER_{HONO/CO}$ values ranging from 0.26 to 17.2 pptv $ppbv^{-1}$ (Yokelson et al., 2007; Veres et al., 2010; Akagi et al., 2011, 2012; Andreae, 2019; Peng et al., 2020) and $ER_{HONO/NOx}$ ranging from from 0.03-0.54 pptv $pptv^{-1}$ (Burling et al., 2010; Keene et al., 2006; Yokelson et al., 2007, 2009; Theys et al., 2020). Many estimates come from laboratory studies, which cannot replicate the complex combustion of natural wildfires. Fuels in these studies are often drier and real world wind conditions cannot be simulated, typically leading to higher MCE values than natural fires (Andreae, 2019).

Field studies also have limitations. The strong convection and heat associated with burning make sampling near the fire a serious safety concern and the earliest measurements are usually taken at least 30 minutes downwind. As mentioned above, HONO photolyzes very efficiently, with a 10-20 minute lifetime in clear sky conditions. Even though high aerosol concentrations in smoke plumes reduce the available light and increase the HONO lifetime, some of the initially emitted HONO is likely lost prior to observations. Complex plume dynamics and variable particle and gas emissions make very young smoke a complicated radiative environment. Estimates of photolysis rates at this stage are therefore difficult so there are uncertainties when trying to back calculate HONO emissions from downwind measurements.

Many studies have found that plume O_3 levels and early chemistry are dependent on HONO emissions (Trentmann et al., 2005; Alvarado and Prinn, 2009; Alvarado et al., 2009; Theys et al., 2020; Wang et al., 2021; Peng et al., 2020). In addition to impacting local air quality, NO_x and HONO emitted from wildfires can also influence the reactive nitrogen budget in regions thousands of kilometers downwind (Jaffe et al., 2013; McClure and Jaffe, 2018; Westerling, 2016). TROPOMI satellite measurements indicate HONO emissions across all ecosystems may be 2-4 times higher than current estimates (Theys et al., 2020). This would obviously have a significant impact on our current understanding of plume chemistry and emphasizes the need for more detailed and better constrained emissions estimates.

1.3.3 Downwind HONO chemistry

Similar to HONO emissions, in-plume HONO chemistry is also extremely variable with a dependence on emissions, sunlight, plume opacity, cloud cover, and plume dilution. Measurements are again sparse so there is limited knowledge on how HONO levels change as plumes age and mix with ambient air. Multiple field and modeling studies indicate HONO is the main OH source in early plumes since it is directly emitted from fires and quickly photolyzes (Reaction 1.4) (Trentmann et al., 2005; Alvarado and Prinn, 2009; Alvarado et al., 2009;

Peng et al., 2020; Wang et al., 2021). Peng et al. (2020), for example, measured HONO during the recent WE-CAN campaign in the western United States and found that, as a campaign-average, HONO contributed over 90% to the primary HO_x production during the first hour after emission. HCHO, O_3, and other VOCs become more important as plumes age but early plume chemistry is clearly controlled by initial HONO concentrations.

It has been suggested that HONO is formed within plumes in addition to being directly emitted. With the large concentration of aerosols in plumes, heterogeneous formation on aerosol is much more likely than in urban areas. Some modeling studies have found that a secondary HONO source is required to predict accurate O_3 and OH levels downwind (Trentmann et al., 2005; Alvarado and Prinn, 2009; Alvarado et al., 2009). By adding NO_2 conversion to HONO on aerosol, they report increased photochemistry in early plumes and increased O_3 formation. These studies lack reliable HONO measurements, however, so it is difficult to evaluate model performance.

The recent modeling study by Wang et al. (2021), however, found that including NO_2 conversion on aerosols led to better agreement between modeled and observed HONO. The earliest measurement in this study was at 10 km downwind of the fire location, corresponding to about a 1 hour smoke age. Ground based measurements also suggest that HONO is formed from NO_2 conversion on the ground (Chai et al., 2021; Kaspari et al., 2021). As discussed in the Section 1.2.3, HONO can also be formed through photolysis of HNO_3/nitrate in aerosol. Isotopic analysis of HONO observations at the ground suggest that this pathway plays a minor role in the HONO budget downwind (Chai et al., 2021), but there have not been any detailed studies of these formation processes within lofted plumes so their relative importance is currently unknown.

Plume structure and dilution are also important aspects that influence HONO chemistry. As plumes mix with ambient air, aerosol concentrations and light extinction decrease, leading to faster HONO photolysis. This occurs more quickly at the plume edges, causing lower HONO levels. Studies have also seen enhanced photolysis rates at the plume top due to

mixing and enhanced scattering from below (Peng et al., 2020; Wang et al., 2021). These factors give HONO complex spatial variations which make sampling location within a plume an important aspect to consider when determining overall HONO levels and OH chemistry. Wang et al. (2021), for example, found most of the HONO loss occurred at the plume top and edged. This correlated to enhanced OH concentrations in these regions which drove the overall plume photochemistry. Most in-situ measurements of smoke are performed via aircraft at a single altitude flying through the plume. This probes only a small portion of the overall plume, which is especially problematic for fast reacting species like HONO. This type of sampling, along with the limited number of observations, lead to a lack of understanding of HONO chemistry in biomass burning plumes.

1.4 Science questions

Despite years of research, HONO chemistry is often excluded from or simplified in air quality models due to uncertainties in its emissions and formation mechanisms. This leads to an underestimation of HONO, which consequently impacts concentrations of radicals and pollutants like ozone (Czader et al., 2012; Elshorbany et al., 2012; Alvarado and Prinn, 2009). Implementing accurate HONO chemistry is needed to improve air quality modeling, especially as air quality standards become more strict. The goal of this dissertation is to better constrain HONO sources and understand its impact on air quality by answering the following questions.

- Which heterogeneous HONO formation mechanisms play a significant role in the HONO budget in urban areas?
- How do heterogeneous HONO sources influence the OH budget over the entire urban boundary layer?
- What role does HONO play in the radical budget and ozone formation in biomass

burning plumes?

- Can secondary HONO formation on aerosols help explain HONO concentrations in biomass burning plumes downwind from the fire source?

1.5 Thesis outline

In Chapter 2, I will introduce the two field experiments used here to study HONO chemistry. I will first describe the Differential Optical Absorption Spectroscopy (DOAS) technique which is used to measure HONO. The CalNex campaign, conducted in the city of Los Angeles in 2010, is used as a case study for HONO chemistry in the urban boundary layer. HONO in biomass burning plumes is investigated using data from the FIREX-AQ campaign, where multiple wildfire plumes in the western United States were sampled during the summer of 2019. The PACT-1D model, developed for this thesis to help interpret field observations, is described in Chapter 3. I discuss the logic and general aspects of the model and then describe the specific model setup and input parameters for both studies.

Model results from the CalNex and FIREX-AQ study are presented and discussed in Chapters 4 and 5, respectively. I first compare the model results to in-situ and remote sensing field measurements. I investigate the HONO budget to determine the relative importance of emissions and secondary production in both environments. Sensitivity studies to address uncertainties in the secondary formation mechanisms are also presented. Lastly, the production of OH from HONO is compared against other radical precursors and the overall impact on air quality and O_3 levels is discussed. Chapter 6 includes conclusions and outlook.

CHAPTER 2

Instrumentation and Field Campaigns

2.1 Differential Optical Absorption Spectroscopy (DOAS)

Differential Optical Absorption Spectroscopy (DOAS) is a remote sensing technique that identifies and quantifies atmospheric trace gases based on their absorption structure. While many atmospheric components exhibit broad spectral absorption features, DOAS separates these from the narrow-band absorptions (i.e., varying strongly with wavelength) associated with specific trace gases. This differential absorption is used to quantify trace gas concentrations. Some common gases measured using DOAS are O_3, NO_2, HONO, HCHO, and halogen oxides (Platt and Stutz, 2008).

The DOAS technique is based on the Lambert-Beer law.

$$I(\lambda) = I_0(\lambda) \times \exp(\Sigma\tau_i(\lambda)) \tag{2.1}$$

$I(\lambda)$ is the intensity of light observed at wavelength λ, which passes through a medium of specific length L; $I_0(\lambda)$ is the intensity of light emitted by a source; and $\Sigma\tau_i(\lambda)$ is the sum of optical depths describing all light attenuation along the light path L. The intensity of light passing through a medium, therefore, decreases exponentially as a function of the light path length and the properties of the medium.

The optical depth, τ, of a trace gas is a function of its concentration (c), its wavelength dependent absorption cross section ($\sigma(\lambda)$), and the light path length (L).

$$\tau_j(\lambda) = c_j \times \sigma_j(\lambda) \times L \tag{2.2}$$

In addition to trace gas absorption, other light extinction processes need to be considered in $\Sigma\tau_i(\lambda)$, including molecular (Rayleigh) and aerosol (Mie) scattering.

$$\Sigma\tau_i(\lambda) = [(c_j \times \sigma_j(\lambda)) + \epsilon_R(\lambda) + \epsilon_M(\lambda)] \times L \tag{2.3}$$

$\epsilon_{\mathrm{R}}(\lambda)$ and $\epsilon_{\mathrm{M}}(\lambda)$ describe the light attenuation from Rayleigh and Mie scattering, respectively.

Since the absorbing trace gas cannot be removed from the atmosphere to directly measure $\mathrm{I}_0(\lambda)$, DOAS uses a modified I_0'(λ) that is described by broad spectral structures, including Rayleigh and Mie scattering. Trace gas absorption cross sections can be separated into narrow-band (σ_j'(λ)) and broad-band ($\sigma_{j0}(\lambda)$) absorption features (Equation 2.4), and $\sigma_{j0}(\lambda)$ can be combined with $\epsilon_{\mathrm{R}}(\lambda)$ and $\epsilon_{\mathrm{M}}(\lambda)$ to define I_0'(λ) (Equation 2.5). In practice, instrumental and turbulence effects also influence the amount of light that reaches the observer and are typically included in the definition of I_0'(λ) as a combined attenuation parameter, $\mathrm{A}(\lambda)$.

$$\sigma_j(\lambda) = \sigma_{j0}(\lambda) + \sigma'_j(\lambda) \tag{2.4}$$

$$I'_0(\lambda) = I_0(\lambda) \times \exp(-L \times [\Sigma(\sigma_{j0}(\lambda) \times c_j) + \epsilon_R(\lambda) + \epsilon_M(\lambda)]) \times A(\lambda) \tag{2.5}$$

Taking the ratio of I_0'(λ) and the measured $\mathrm{I}(\lambda)$, we can define the differential optical density, D'.

$$D' = \ln \frac{I_0'(\lambda)}{I(\lambda)} = L \times \Sigma(\sigma_j'(\lambda) \times c_j) \tag{2.6}$$

Since absorption features are unique for trace gas, Equation 2.6 can be used to solve for the concentration of individual species if measurements are taken over a range of wavelengths.

HONO absorbs strongly in the UV-vis spectral region from 330-380 nm and can therefore be detected using DOAS. It is an advantageous measurement technique for multiple reasons and has been used in a number of field studies (Acker et al., 2006; Alicke et al., 2002; Tsai et al., 2018; Wong et al., 2011; Stutz et al., 2002; Volkamer et al., 2010). First, the ability to average over long light paths increases measurement sensitivity and allows for the detection of trace gases present at low concentrations, like HONO. Simultaneous measurements of the HONO precursor, NO_2, can also be recorded under the same conditions of HONO observations. Additionally, there are no sampling artifacts or chemical interferences (Platt and Stutz, 2008). The heterogeneous formation of HONO on surfaces, such as those described in Section 1.2.3, can occur in instrument sampling lines, giving unreliable results from other instruments if not considered in the analysis (Zhou et al., 2002; Kleffmann, 2007). DOAS was therefore used to measure HONO in both field campaigns discussed below.

2.2 California Research at the Nexus of Air Quality and Climate Change (CalNex) Experiment

The California Research at the Nexus of Air Quality and Climate Change (CalNex) experiment took place in southern and central California from May through July, 2010 (Ryerson et al., 2013). The goal of the study was to investigate issues that simultaneously impact air quality and climate change, with a focus on providing sound science to policy makers in the state of California. Specifically, the project aimed to assess the current understanding of emissions inventories, atmospheric transport and dispersion, atmospheric chemistry, and

aerosol radiative effects. Measurements were taken on multiple platforms, including two ground sites, a research ship, balloon-borne ozonesondes, and four aircrafts. These were analyzed in conjunction with satellite data. All CalNex observations are publicly available at www.esrl.noaa.gov/csd/projects/calnex/.

This thesis focuses on data collected from mid-May to mid-June at the ground site located on the California Institute of Technology (Caltech) campus in Pasadena, CA. Pasadena is only 18 km northeast of downtown Los Angeles so is a good representation of the urban boundary layer (Figure 2.1). Nearly 40 research teams participated in this portion of the experiment, providing an extensive dataset of trace gas, aerosol, and atmospheric property information. One component of the campaign's emissions and chemistry goals was to better understand chemical processes that impact O_3 formation and how these may differ between the more urban areas of southern California and the rural Central Valley. HONO measurements play a key role in this objective.

HONO data from two instruments is used: UCLA's long-path Differential Optical Absorption Spectroscopy (LP-DOAS) instrument and NOAA's negative-ion proton-transfer chemical ionization mass spectrometer (NI-PT-CIMS). The LP-DOAS was located on the roof of Caltech's Millikan library and probed air between 33-556 m above ground level (agl) in four different altitude intervals (Figure 2.1). NOAA's NI-PT-CIMS was located on a scaffolding tower and sampled air at 3 m agl. Other observations relevant for understanding the formation of HONO and its impact on atmospheric chemistry were also used. In-situ measurements of O_3, NO_x, HO_x, VOCs, and aerosol number distribution were collected at 10 m agl on top of a scaffolding tower. We concentrate on a four day period, May 26 - May 30, 2010, during which a variety of conditions were encountered, including cloudy days and the highest ozone levels of the experiment. This period also has the best coverage of all instruments, in particular the LP-DOAS.

Figure 2.1: Map of the CalNex Pasadena ground site, shown with a star, in relation to downtown Los Angeles. The LP-DOAS retroreflector array locations and light paths are also shown in the colored diamonds and lines. Figure from Tsai et al. (2014).

2.2.1 LP-DOAS

Figure 2.2 shows a schematic of the LP-DOAS setup. The instrument consists of a main telescope/spectrometer unit, which was located on top of Millikan Library on the Caltech campus at 33 m altitude. The LP-DOAS is an active DOAS system, meaning an artificial light source is used rather than natural light. In this setup, a xenon (Xe) arc lamp feeds light into a telescope where it is collimated and sent to an array of quartz corner-cube retroreflectors. The array returns the light back to the telescope where it is received by a quartz fiber mode mixer and sent into a spectrometer-camera system (Platt and Stutz, 2008; Tsai et al., 2014).

Four arrays of retroreflectors were mounted at different distances and altitudes at sites in the nearby San Gabriel Mountains (Figures 2.1 and 2.2). The retroreflectors and the associated air samples are labeled by their relative altitudes: lower (78 m), middle (121 m), high (255 m), highest (556 m). The instrument was aimed at the four reflectors using a cycle of measurements with a repeat interval of 15 - 30 min, depending on visibility.

The light received back was measured using the multichannel scanning technique (Platt and Stutz, 2008) in the 300-380 nm range with a spectral resolution of 0.6 nm. Trace gas path-averaged concentrations were retrieved using established DOAS techniques as described in Platt and Stutz (2008), with further detail in the next section. Average detection limits for NO_2 and HONO on a single absorption path were 0.16 ppb and 0.06 ppb, respectively. It should also be pointed out that the LP-DOAS, which was located about 550 m southeast of the other instruments, averaged over 5-7 km long absorption light paths.

The LP-DOAS measured continuously throughout CalNex, however, low visibility and low clouds blocked the light beams at some times. Low clouds were especially common during the night and often only the lowest light path data was available. The dates chosen for this study (May 26 - May 30) had good coverage along all light paths.

2.2.2 LP-DOAS analysis

When analyzing spectral data collected by the LP-DOAS system, it is necessary to consider how instrument limitations impact the measured light ($I(\lambda)$ in Equation 2.6). All spectroscopic instruments have a limited wavelength resolution, so the recorded light intensity is in reality a convolution of $I(\lambda)$ with an instrument function, H. This convolution changes the shape of $I(\lambda)$. Additionally, the instrument detector digitizes $I(\lambda)$, mapping the wavelength range to discrete pixels and integrating between them. The wavelength integral is given by the wavelength-pixel mapping parameter of the instrument, which can be approximated by a polynomial.

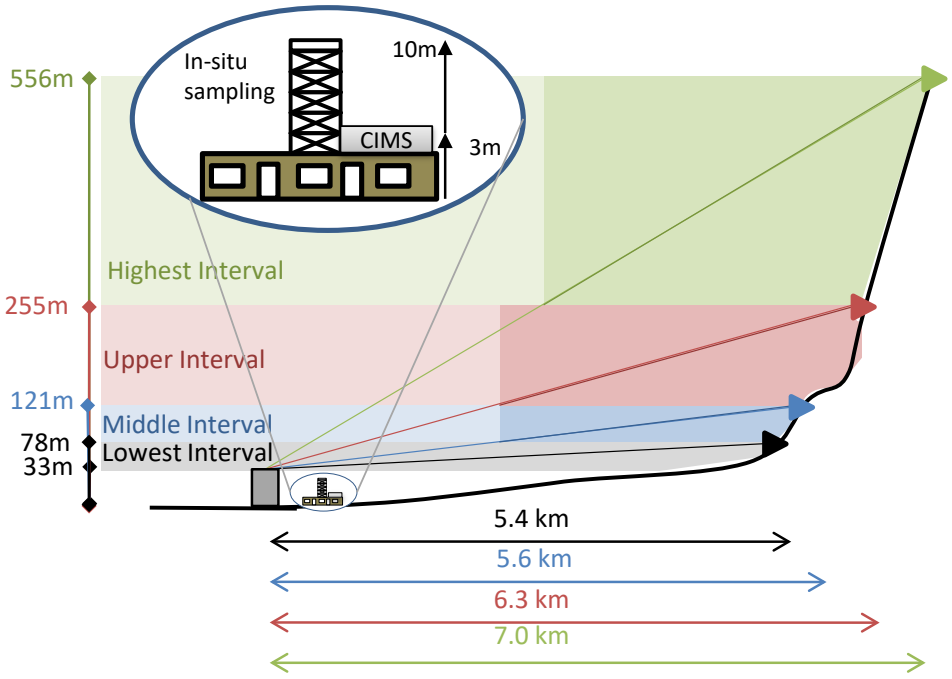

Figure 2.2: Sketch of the Pasadena ground site setup during the CalNex 2010 experiment. The LP-DOAS was located on top the Millikan Library at 33 m agl. The individual light paths and their corresponding length and heights are indicated. All other in-situ measurements were collected at 3 or 10 m agl.

Features from electrical components of the instrument, including dark current and the electronic offset, along with the lamp spectrum also impact the recorded light intensity and need to be considered in the analysis procedure. Diode sensitivity variations are reduced by implementing the multichannel scanning technique (MCST), described in Platt and Stutz (2008). The dark current and offset spectra are subtracted from the MCST spectrum to remove their influence.

To retrieve trace gas concentrations, the measured spectra are analyzed with a combination of linear and nonlinear least squares fit procedures, using references from a number of trace gases, the lamp spectra, and a polynomial to describe the broad spectral features. The trace gas reference spectra are taken from literature absorption cross sections and adapted

to the instrument function. The fit parameters describe the optical density and can be used to calculate the path averaged trace gas concentrations (Equation 2.6). The DOAS analysis calculates an error for each trace gas and absorption spectrum based on sound statistical principles, reported as 1σ statistical uncertainties. The two sources of systematic error include instrumental error (<3%) and those associated with the literature absorption cross sections (3-8%) (Tsai et al., 2014). The reported detection limits are calculated as twice the 1σ statistical error.

An important feature of the LP-DOAS is the ability to study the vertical variability of trace gas concentrations. Vertical profiles were therefore constructed from the path averaged mixing ratios. The path-averaged values were first linearly interpolated onto the time grid of the lowest light path and then converted to height interval-average mixing ratios (C_i) using the equation below (Tsai et al., 2014).

$$C_i = (\frac{H_i - h}{H_i - H_{i-1}} \times c_i) - (\frac{H_{i-1} - h}{H_i - H_{i-1}} \times c_{i-1}) \tag{2.7}$$

H_i is the top height of each light path (78, 121, 255, and 556 m), h is the measurement base height (i.e., the height of the instrument at 33 m), and c_i is the path-averaged concentration derived from the DOAS analysis. These new averages are reported at the midpoint of each height interval (55.5, 99.5, 188, and 405.5 m).

2.2.3 NI-PT-CIMS

A negative-ion proton-transfer chemical ionization mass spectrometer (NI-PT-CIMS) using acetate ions provided HONO and HNO_3 observations at 1-minute resolution during CalNex. The NI-PT-CIMS has been used in past field studies as well, including Roberts et al. (2010) and Veres et al. (2011). Ambient air was sampled through a 1.5 m PTFE inlet heated from a point approximately 3 m agl. Acidic molecules are ionized via proton abstraction reactions

with acetate ions (CH_3COO^-) and detected as the conjugate anion, using a quadrupole mass spectrometer. Instrument backgrounds using a sodium carbonate denuder were performed every 190 min for 30 min.

HONO calibrations were performed in-field approximately every two days using using a portable source described elsewhere (Roberts et al., 2010). Measurement of HONO by the NI-PT-CIMS required correction for NO_2. Correction factors were determined through laboratory additions of NO_2 as a function of relative humidity with NO_2 quantified by CRDS. Detection limits for HONO were 10 ppt, with an uncertainty of 30% + 20 ppt for 1-min measurements. Nitric acid calibrations were performed during post-field laboratory work using a permeation source calibrated with UV optical absorption (Neuman et al., 2003). HNO_3 was measured with a detection limit of 15 ppt, with a stated uncertainty of 30% + 30ppt for 1-min measurements.

2.2.4 Other measurements

A number of other observations from CalNex are also used in the analysis and model evaluation. Table 2.1 lists these parameters, the respective instruments, and literature references of the CalNex results.

2.3 Fire Influence on Regional to Global Environments and Air Quality (FIREX-AQ)

The Fire Influence on Regional to Global Environments and Air Quality (FIREX-AQ) experiment was conducted during the summer of 2019 in the western and southeastern United States. The overarching goals of the study were to better understand gas and aerosol emissions from North American fires, how these species change chemically during smoke transport, and the overall influence of fires on air quality and the climate. The campaign focused on two types of biomass burning: natural wildfires in the western U.S. and prescribed agri-

Species/ Parameter	**Instrument**	**Operator**	**Reference**
O_3	UV-absorption	Univ. Houston (UH)	Pollack et al. (2010)
NO, NO_2	Chemiuminescence with photolytic converter	Univ. Houston (UH)	Pollack et al. (2010)
NO_2	Cavity Ring-Down Spectroscopy (CRDS)	NOAA	Washenfelder et al. (2011)
OH, HO_2	Laser Induced Fluorescence (LIF-FAGE)	Indiana Univ.	Dusanter et al. (2009) Griffith et al. (2016)
VOC	GC-MS	NOAA	Gilman et al. (2010) Borbon et al. (2013)
Actinic Flux	Spectroradiometer	Univ. Houston (UH)	Shetter and Müller (1999)
Aerosol Number Ditribution	TSI SMPS	CU Boulder	Hayes et al. (2013)
HONO, HNO_3	NI-PT-CIMS	NOAA	Veres et al. (2008)

Table 2.1: Overview of CalNex measurements used in this thesis.

cultural burning in the southeast. Wildfires are expected to increase in size and frequency over the coming years, posing significant threats to air quality (Westerling, 2016; McClure and Jaffe, 2018; Williams et al., 2019). Agricultural fires, although much smaller, can have significant local impacts on air quality and their emissions have not been well studied or quantified (McCarty et al., 2009; Pouliot et al., 2017). For this thesis, only data from the wildfire portion of the study is used.

Multiple sampling platforms were utilized during the western wildfire portion of FIREX-AQ, including aircrafts, ground based networking sites, mobile labs, and satellites. All data is publicly available at https://www-air.larc.nasa.gov/missions/firex-aq/index.html. NASA's DC-8 flying laboratory, which was stationed in Boise, ID, provided the most comprehensive sampling of wildfire smoke plumes. 31 in-situ and remote sensing instruments were deployed on the DC-8 to collect measurements of trace gas concentrations, aerosol properties, meteorological data, and fire radiative power.

The DC-8 completed 15 research flights from Boise, sampling over 10 different fires (some over multiple days). A similar sampling pattern was used for each fire, combining remote sensing overpass segments with in-plume transects for in-situ smoke characterization. First, the DC-8 would approach the fire from downwind and fly above the smoke along the length of the plume towards the fire. During these flight portions, the remote sensing instruments observed the smoke from above. Aerosol extinction and backscatter data from the LIDAR instrument (NASA's DIAL/HSRL) detailed the location and altitude of the plume. The aircraft then descended to the plume altitude. An upwind transect was performed to establish background air concentrations before the aircraft began crossing perpendicularly through the plume, starting near the fire and continuing downwind. If time permitted, this pattern was typically repeated at least once.

One of the remote sensing instruments on board the DC-8 was UCLA's mini-DOAS. As mentioned above, DOAS is capable of measuring HONO and the mini-DOAS provided an opportunity to quantify HONO in smoke plumes. In particular, observations were taken

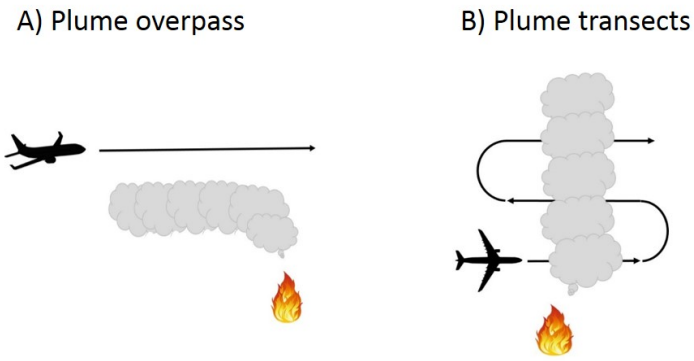

Figure 2.3: Cartoon of typical flight strategy during FIRE-AQ. Overpasses (A) were generally flown first to characterize the plume with remote sensing instruments, followed by transects (B) to collect measurements within the smoke.

during the overpass flight segments, providing a continuous view of HONO levels along the length of the plume. This also allowed measurements of HONO right above the burning location, proving emissions data that is inaccessible to in-situ instruments. This dataset, combined with in-situ HONO measurements taken within the smoke by the NOAA CIMS (Iodide Ion Time of Flight Chemical Ionization Mass Spectrometer) and NOAA ACES (Airborne Cavity Enhanced Spectrometer) instruments allow for a comprehensive analysis of HONO emissions and chemistry in wildfire smoke. Additional observations of trace gases, including O_3, NO_x, VOCs, CO, and HCHO are also used in this analysis and are detailed below.

2.3.1 Mini-DOAS

The mini-DOAS is a passive airborne remote sensing instrument with three spectrometer/telescope units (Figure 2.4). The spectrometers measure scattered sunlight in different wavelength ranges, covering the UV-vis, visible, and near-IR, and are housed in a vacuum sealed and thermally insulated box inside the aircraft. The ice water bath ensured stable temperatures throughout the flight. Each spectrometer was connected to a separate tele-

scope with fiber optic cable bundles. The telescopes were mounted on the outside of the DC-8 (Figure 2.5) and had the ability to measure at any angle between the nadir and the zenith. Different viewing geometries were chosen based on the plume location and sampling strategy. Generally, observations were taken in the nadir for plume overpasses and in the zenith or limb for plume transects.

Since HONO absorbs in the UV-vis spectral region, data from this spectrometer will be used in this work. Scattered sunlight was measured from 300-380 nm with a 0.5 nm full width half maximum (FWHM) resolution. A 5 second time resolution was typical throughout the campaign. In addition to HONO, NO_2 and HCHO were also measured by the UV-vis spectrometer.

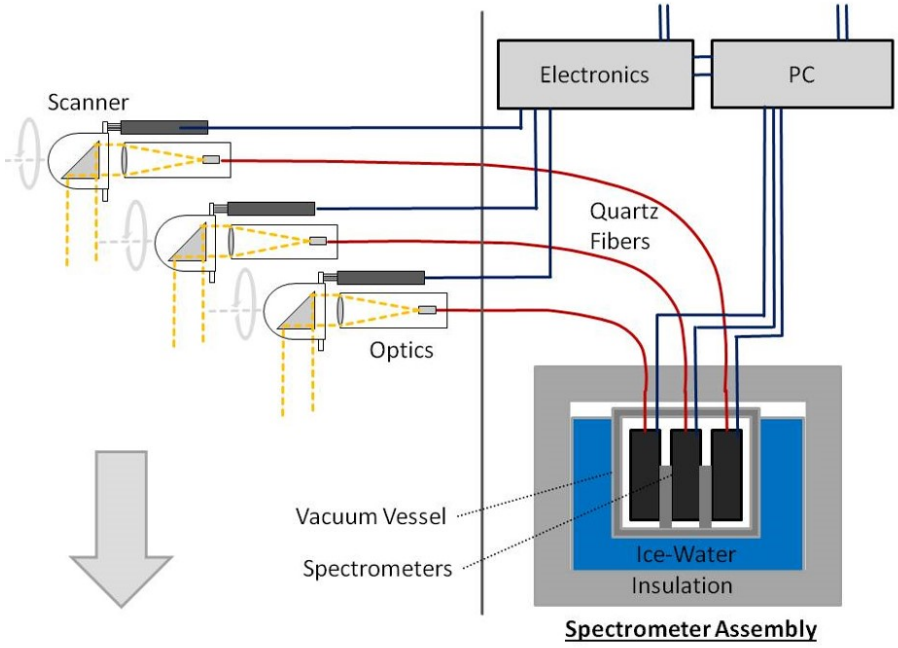

Figure 2.4: Sketch of the mini-DOAS instrument during FIREX-AQ. Three individual spectrometers were housed in an insulated and vacuum sealed box, and connected to a telescope that could measure at any angle between the zenith and nadir. Figure from Stutz et al. (2010).

Figure 2.5: Pictures of the DC-8 aircraft during FIREX-AQ, showing the three mini-DOAS telescopes on the left and the numerous instruments on board on the right.

2.3.2 Mini-DOAS analysis

Similar to the LP-DOAS described above, instrument limitations regarding wavelength resolution and wavelength-pixel mapping need to be considered in analysis of mini-DOAS data. The impact of dark current and electronic offset are also removed from the measured spectra. A significant difference between the two instruments is that the mini-DOAS is a passive system, using the sun as a natural light source instead of a lamp. The primary measurement in passive DOAS systems is still a path averaged concentration, referred to here as a slant column density (SCD), but instead of a single light path provided by a lamp, it is necessary to consider all of the complex paths sunlight may take to reach the instrument. Measurement geometry, surface albedo, aerosol extinction, and wavelength all impact how light travels in the atmosphere so a radiative transfer model (RTM) is required to define the path length. In the context of a biomass burning plume, this is even more complex due to the high concentration of gases and aerosols within a thin altitude range.

The sun's solar spectrum is highly structured and must be taken into account when us-

ing passive DOAS systems. A solar, or Fraunhofer, reference is therefore recorded under the same conditions which the trace gas measurements are taken. During FIREX-AQ, this involved taking a zenith measurement at a similar altitude and solar geometry as the target measurements, but prior to any influence of smoke. For plume overpasses, the zenith solar reference was typically recorded prior to measuring the plume in the nadir, and for plume transects, a reference was recorded during the upwind transect. Reference spectra were co-added, generally for at least a 1 minute period, which helped reduce measurement uncertainty. Since these reference spectra are influenced by trace gas absorptions in the background air, the DOAS retrieval is actually a differential slant column density (DSCD)

$$DSCD = SCD - SCD_0 \tag{2.8}$$

where SCD_0 is the solar reference spectrum.

DSCDs for HONO, NO_2, and HCHO were retrieved using a similar method as the LP-DOAS analysis. A combination of linear and nonlinear least squares fit is used with trace gas absorption cross sections from literature, a low order polynomial to describe broad band absorption from Rayleigh and Mie scattering, and the zenith solar reference. For young, thick smoke plumes, the median fit uncertainties were 12% for HONO, 17% for NO_2, and 15% for HCHO.

Since SCDs and DSCDs depend on the light path, a more useful and understandable parameter is the vertical column density (VCD), which sums all molecules of a trace gas in a vertical column from the surface to the top of the atmosphere (Equation 2.9). The VCD is related to the SCD using an air mass factor (AMF) (Equation 2.10), which describes the enhancement of the light path length through the atmosphere and is determined with a RTM.

$$VCD = \int_0^{TOA} C(z)dz \tag{2.9}$$

$$VCD = \frac{SCD}{AMF} \tag{2.10}$$

The VLIDORT-QuasiSperheical (VLIDORT-QS) vector RTM, which is based on the 2015 2.7 version of VLIDORT (Spurr, 2006) was used to calculate VCDs for each of the plume overpasses during FIREX-AQ. Data from a number of instruments on board the DC-8 was used to constrain the RTM. Further details on VLIDORT-QS and the FIREX-AQ analysis can be found in Brockway (2021). The VCDs retrieved from this analysis are compared to chemical modelling results later in this thesis (Chapter 5).

2.3.3 Other measurements

Many of the other measurements collected on board the DC-8 are used in the model intialization, validation, and analysis in this work. Table 2.2 lists these parameters, the respective instruments, references. In particular, both the NOAA ACES and NOAA CIMS instruments provided in-situ measurements of HONO.

Species/Parameter	**Instrument**	**Operator**	**Reference**
HONO, NO_2	ACES	NOAA	Min et al. (2016)
pNO_3	AMS	CU Boulder	Decarlo et al. (2006)
Photolysis rates	CAFS	NCAR	Shetter and Müller (1999)
HCHO, C_2H_6	CAMS	CU Boulder	Richter et al. (2015)
HONO	CIMS	NOAA	Veres et al. (2015)
CO	DACOM	NASA	Warner et al. (2010)
Aerosol extinction and backscatter	DIAL/HSRL	NASA	Hair et al. (2008)
HCHO	ISAF	NASA	Cazorla et al. (2015)
Particle size distribution	LARGE	NASA	Beyersdorf et al. (2016)
NO	LIF	NOAA	Rollins et al. (2020)
Met parameters (T, p, alt)	MMS	NASA	Chan et al. (1998)
NO_2, O_3	O_3-induced chemiluminescence	NOAA	Pollack et al. (2010)
VOCs	PTR	NOAA	Yuan et al. (2016)
Carbon emissions	Fuel2Fire analysis	NIA	Wiggins et al. (2021)
Smoke age	Trajectory analysis	FSU	

Table 2.2: Overview of FIREX-AQ measurements used in this thesis.

CHAPTER 3

Platform for Atmospheric Chemistry and Transport in One Dimension (PACT-1D) Model

3.1 Model overview

One of the challenges in modeling HONO chemistry is that the formation mechanisms are not well understood. It was therefore necessary to develop a model where different chemical mechanisms could be easily tested and results could be compared to field observations. One-dimensional chemistry and transport models are an ideal tool to study poorly constrained chemistry and have provided insight into a number of atmospheric systems, including snow-atmosphere interactions (Cao et al., 2014, 2016; Thomas et al., 2011, 2012; Toyota et al., 2014), forest canopies (Boy et al., 2011), and the marine boundary layer (von Glasow et al., 2002b,a). Only a few studies however have addressed the heterogeneous chemistry of HONO (Wong et al., 2011, 2013; Karamchandani et al., 2014; Tsai et al., 2018). A previous 1D model, RCAT, successfully reproduced HONO observations in polluted areas (Wong et al., 2011, 2013; Tsai et al., 2018), but was limited in its ability to test new mechanisms. There is thus a need for a model with the ability to easily perform mechanistic studies of these systems.

In order to study HONO chemistry in urban and biomass burning plume environments, a new one dimensional chemistry and transport model, the Platform for Atmospheric Chemistry and Transport in One Dimension (PACT-1D) has been developed as a major component of this thesis. The model was designed with a number of requirements:

1. To allow for comparison with field observations, the model needed the ability to ingest various environmental parameters, such as photolysis rates and turbulent exchange coefficients, derived from observations or meteorological models.

2. To test various mechanism changes to the chemical mechanism, it needed to be quick and efficient.

3. For a thorough mechanistic analysis, the model needed to output all chemistry and transport rates.

4. To accurately simulate transport limitation to the surface, the model had to be capable of using small, and even logarithmic, grid sizing.

5. The model had to run on any computer system without extensive user programming experience.

PACT-1D is a vertical column model used to study the interactions between chemical processing and vertical transport processes. It is based on the success of previous modeling (Wong et al., 2011, 2013; Tsai et al., 2018), but includes improved capability to perform mechanistic and sensitivity studies. Similar to past models of this type, chemistry is calculated online and dynamics and physics are provided as input (Geyer and Stutz, 2004b). PACT-1D solves both 1D transport and chemical kinetics resulting in the time evolution (t) of a chemical species (i) at altitude z. The continuity equation for the change in concentration C for the 1D chemical system is given by Equation 3.1.

$$\frac{dC_{(i,t,z)}}{dt} = P_{(i,t,z)} - L_{(i,t,z)} + F_{(i,t,z)} + E_{(i,t,z)} \tag{3.1}$$

P and L represent chemical production and loss, F refers to the flux due to vertical mixing, including loss to the ground (deposition), and E is the rate of emissions. We treat

each process including chemistry, vertical mixing, and emissions as separable using operator splitting.

Emissions are provided as input and are time and height dependent. Chemical production and loss are described using the Regional Atmospheric Chemistry Mechanism version 2 (RACM2) (Goliff et al., 2013), implemented with the Kinetics Pre-Processor (Sandu and Sander, 2006). RACM2 includes 363 reactions and 119 species, including 17 stable inorganics, 4 inorganic intermediates, 55 stable organic species, and 43 organic intermediates. Organic species are aggregated into groups based on emission rates, typical concentrations, reaction mechanism similarities, and reactivity. Additional reactions were added to the mechanism, including 51 chlorine reactions and 3 reactions to parameterize particle nitrate (pNO_3) chemistry. The pNO_3 reactions, which are relevant to HONO formation on aerosol surfaces, will be described below. Photolysis rates used in the mechanism are provided as input.

In addition to gas phase chemistry, non-reactive uptake of gases to aerosols and heterogeneous surface reactions on aerosols are included. For heterogeneous chemistry, the aerosol surface area (S) is calculated in each model level (z) at a given time (t) according to

$$S_{(z,t)} = 4\pi r_{(z,t)}^2 N_{(z,t)} \tag{3.2}$$

where r and N represent the radius and number concentration of a mono-disperse aerosol that best represents the surface area available for reactions. Aerosol physical properties (N and r) are given as model input. Therefore, no aerosol physics is calculated online within the model. Irreversible uptake to and heterogeneous reactions on aerosols are treated with the rate constant (k_T) given by

$$k_T = \frac{1}{4}\nu S \gamma f \tag{3.3}$$

where ν is the mean molecular speed, S is the aerosol surface area (per cm^3 air volume), and γ represents the probability of irreversible uptake or interfacial reaction. The flux of molecules to the aerosol surface in the transition regime, f, is calculated according to Fuchs and Sutugin (1971). This corrects the rate of diffusion for gas molecules towards an aerosol surface when the particle size is similar to the mean free path in air.

Vertical mixing and loss to the the ground are solved together in the vertical mixing term, given as $F_{(i,t,z)}$ in Equation 3.1. We treat vertical mixing and surface loss (i.e. deposition) for each species according to

$$F_{(i,t,z)} = \frac{\partial}{\partial t} C_{(i,t,z)} = \frac{1}{\rho_{(i,t,z)}} \frac{\partial}{\partial z} \left(\rho_{(i,t,z)} K_{D(i,t,z)} \frac{\partial}{\partial z} C_{(i,t,z)} \right) + R_{(1,t)} \tag{3.4}$$

where C_i is the species concentration in mixing ratio units, ρ is the air density, and R represents loss to the ground in the lowest model level. $K_{D(i,t,z)}$ is the sum of eddy diffusivity ($K_{Z(t,z)}$) plus molecular diffusion ($D_{(i,t,z)}$). For studies focusing on surface chemistry at the ground, the model levels below 1 meter should be discretized using a logarithmic scale grid. This ensures the lowest model level is appropriate for treatment of a laminar molecular diffusive layer in direct contact with the Earth's surface. $K_{Z(t,z)}$ decreases in a log profile towards the surface to a molecular diffusion coefficient in the lowest model level.

A unique feature of the model is that uptake and chemistry on the ground (R) are calculated using molecular collisions on the ground and applying an uptake probability (α) or reactive uptake coefficient (γ). Equation 3.4 is solved numerically using the Crank-Nicolson method (Brasseur and Jacob, 2017), which is numerically stable for a variety of non-uniform grids and time steps. Upon solving Equation 3.4, the deposition rate for each time step is calculated. This method allows for molecular level interaction with the surface, resulting in deposition without the need to prescribe a deposition velocity. Loss to the ground is considered for HNO_3, HNO_4, OH, HO_2, HONO, N_2O_5, NO_2, NO_3, O_3, and pNO_3.

Interactive surface chemistry is included as well, which can lead to release of species from the ground into the gas phase.

The specific model setup for the urban boundary layer and biomass burning plume studies are described in the next two sections.

3.2 Model setup for CalNex study

In urban areas, the largest uncertainty related to HONO chemistry is its heterogeneous formation on surfaces. A challenge in studying the link between chemical transformations on the ground and the chemistry in the overlying atmosphere is the role of vertical transport to and from the surface. This was illustrated in 1D modeling studies by Geyer and Stutz (2004a,b), who showed that concentrations change on the scale of one meter or less near the surface. Similar conclusions were derived in nighttime and daytime HONO modeling studies by Wong et al. (2011, 2013) and Tsai et al. (2018), which showed a strong concentration gradient near the surface. Many urban field studies however, focus on observations of trace gases taken at a single altitude. 1D chemistry and transport models, along with vertical profile measurements, can provide insight on how concentrations and chemistry vary with altitude in the boundary layer. PACT-1D is used here to investigate HONO vertical profiles, its formation mechanisms at the ground, and how these impact air quality in urban environments.

For the CalNex modelling study, PACT-1D was initialized using both model data (from WRF-Chem, CAM-Chem, and MEGAN) and observational data from the campaign (Table 2.1). The model run was started in the evening (18:00 on May 27, 2010) to ensure a well mixed boundary layer, and run for 3 days. The 24-hour period from May 26, 2010 18:00 through May 27, 2010 17:00 was used as model spin up, with initial concentration profiles from CAM-Chem model output (Emmons et al., 2020; Buchholz et al., 2019). PACT-1D subdivides the lowest 5000 m of the atmosphere into 26 grid cells, with the upper boundaries

of each grid box at: 1x10 $^{-3}$, 0.01, 0.1, 1, 3, 6, 10, 20, 33, 50, 78, 90, 110, 121, 150, 175, 255, 300, 556, 750, 1000, 1500, 2000, 3000, 4000, and 5000 m. A 20 second chemical time step was used and the typical computing time for a 1 day model run under these conditions was approximately 1 hour.

Time varying profiles of temperature, relative humidity, and pressure were extracted from a WRF-Chem model run for CalNex (Kim et al., 2016), which provided values above 180 m. These were interpolated onto the 1D vertical grid and measured meteorological data was used to create a profile to the surface. Below 180 m, temperature was calculated based on the 10 m measurements of wind speed and temperature, the measured boundary layer height, and atmospheric stability parameters. Relative humidity was given a constant value equal to the measurements at 10 m, and pressure was calculated using the surface pressure and scale height. Eddy diffusion coefficients (K_Z) are taken from WRF-Chem as well (Kim et al., 2016). These values start around 50 m and a log interpolation was implemented to parameterize K_Z values to the ground. The vertical mixing considered boundary layer height variation over the three day period, which is explicitly calculated via the planetary boundary layer (PBL) parameterization within WRF-Chem.

Aerosol number concentration profiles were initialized using data from the TSI Scanning Mobility Particle Sizer (SMPS) instrument. Within the boundary layer, the number concentration was set equal to the measurements at 10 m and then decreased exponentially to one fifth of this value in the top layer of the model. The aerosol radius was assumed to be constant at 150 nm, following the study by Tsai et al. (2014). Photolysis rates were initialized using the Tropospheric Ultraviolet-Visible (TUV) radiation model (v5.0) which was run for the specific dates and location for this study. To account for clouds, measured NO_2 photolysis rates were used to scale the TUV values for all species.

Input anthropogenic emissions are based on the U.S. Environmental Protection Agency (EPA) National Emission Inventory (NEI) and the Fuel-based Inventory for motor Vehicle Emission (FIVE), which have been processed for use in WRF-Chem (Kim et al., 2016).

Biogenic emissions are from the MEGAN model for May 2010. Anthropogenic NO_x was emitted between 0.1-1 m and VOCs were emitted between 0.1-10 m. The emissions were scaled so that model concentrations matched those observed by the LP-DOAS and in-situ observations, using realistic emission injection altitudes for different emission source types. In some cases, the emissions are scaled by up to 50% in order to reproduce realistic VOC and NO_x concentrations, as well as NO_2 concentration profiles.

Emissions scaling is needed to reproduce observations due to the fine model vertical resolution in PACT-1D, which employs a much higher vertical resolution grid than typical 3D chemical transport models. 3D models quickly dilute these emissions into larger volumes of air resulting in lower concentrations of directly emitted species that impact ozone chemistry and other non-linear atmospheric chemical cycling. In addition, the WRF-Chem emissions are general values for either weekday or weekend and have large uncertainties when modeling specific dates and events at high time resolution. The dates for this study includes the weekend (Saturday 5/29 and Sunday 5/30) before a major holiday (Memorial day), which is not necessarily captured in the general emissions used in WRF-Chem.

Soil NO emissions are taken from the Copernicus Atmospheric Monitoring Service (CAMS) global and regional emissions dataset, which considers surface type, for May 2012 near Pasadena, CA (Simpson et al., 2014; Granier et al., 2019). Anthropogenic HONO emissions were included using an emission ratio of $HONO/NO_x = 0.003$ (Kurtenbach et al., 2001). A range of 0.003-0.008 is reported in literature (Kirchstetter et al., 1996; Kurtenbach et al., 2001; Neuman et al., 2016; Kramer et al., 2019). Due to the lower number of diesel engine vehicles in the United States compared to Europe where many of these studies were conducted, a value at the lower end of this range was chosen.

To better simulate the urban atmosphere, chlorine chemistry and parameterized nitrate aerosol chemistry were added to the RACM2 mechanism. Aerosol nitrate is formed through uptake of HNO_3 and N_2O_5, with aerosol uptake coefficients of 0.1 and 0.02, respectively. Partitioning between gas phase HNO_3 and aerosol nitrate is based on the study by Guo

et al. (2017), who found a campaign average partitioning ratio, $\epsilon(NO_3^-)$, of 39% for PM1 during CalNex.

$$\epsilon(NO_3^-) = \frac{NO_3^-}{HNO_3 + NO_3^-} \tag{3.5}$$

Similar to photolysis of HNO_3 on the ground, nitrate in aerosol can also photolyze to produce HONO. This is added to the mechanism with a rate 45 times that of gas phase nitric acid photolysis (Zhou et al., 2003; Karamchandani et al., 2014).

3.2.1 Interactive treatment of surface chemistry

Since the proposed HONO formation mechanisms occur at the ground, detailed surface heterogeneous chemistry has been implemented within PACT-1D. Deposition is calculated from the number of molecular collisions with the ground and an uptake coefficient, allowing for molecular level chemical conversions and surface emissions. The deposited molecules create a surface reservoir of species available for reaction. This quantity was initialized using a model spin-up of four days to achieve near steady state conditions. The HONO formation mechanisms described in Section 1.2.3 were added to PACT-1D with model implementation described below.

3.2.1.1 NO_2 hydrolysis

Conversion of NO_2 to HONO on the ground is implemented into the model using Reaction 1.8. NO_2 deposition is tracked and for every two molecules deposited, one HONO molecule is released from the surface and one HNO_3 molecule is added to the surface storage term. The ground NO_2 uptake coefficient ($\gamma_{NO_2,dark}$) is set at $1x10^{-5}$ (Trick, 2004).

3.2.1.2 Photo-enhanced NO_2 conversion

The photo-enhanced conversion of NO_2 to HONO is included using the parameterization by Wong et al. (2013). In Wong et al. (2012) and Wong et al. (2013), daytime HONO concentrations in Houston, Texas correlated with solar irradiance and they determined that the reactive uptake coefficient for NO_2 could be parameterized with a cubic dependence on the NO_2 photolysis rate (Equation 3.6).

$$\gamma_{\mathrm{NO_2},photo} = 6x10^{-5} \frac{J^3_{\mathrm{NO_2}}}{J^3_{\mathrm{NO_2},noon}} \tag{3.6}$$

6x10 $^{-5}$ is the maximum reactive uptake coefficient. The average noontime photolysis rate for NO_2 ($J_{NO2,noon}$) during the four day study period (May 26-30, 2010) is 7x10 $^{-3}$ s^{-1}. This photo-enhanced NO_2 uptake occurs in addition to dark uptake, giving an effective NO_2 deposition rate ($\nu_{d,\mathrm{NO_2}}$) according to the following equation, where ν is the mean molecular speed. $\nu_{d,\mathrm{NO_2}}$ drives NO_2 deposition in the model.

$$v_{d,\mathrm{NO_2}} = \frac{1}{4} v \gamma_{\mathrm{NO_2},dark} + \frac{1}{4} v \gamma_{\mathrm{NO_2},photo} \tag{3.7}$$

3.2.1.3 Surface nitric acid/nitrate photolysis

Following the modeling study of Sarwar et al. (2008), photolysis of surface adsorbed HNO_3 is parameterized using the following reaction.

$$\mathrm{HNO_{3(ads)}} + h\nu \rightarrow 0.5\mathrm{HONO_{(ads)}} + 0.5\mathrm{NO_{2(ads)}} \tag{3.8}$$

Surface HNO_3 is initialized in the model and it's concentration is updated considering deposition and surface chemistry. HONO and NO_2 produced in Reaction 3.8 are released into

the lowest model layer via desorption. HNO_3 deposition to the ground is calculated using an uptake coefficient of 0.1.

The photolysis rate constant of this reaction ($J_{HNO_3,surf}$) is set to 45 times that of gas-phase HNO_3 (Zhou et al., 2003; Karamchandani et al., 2014), giving noon time values of 2.0x10 $^{-5}$ s^{-1} on May 27 and 2.5x10 $^{-5}$ s^{-1} on May 28 and 29. These rate constants are in accordance with the value of 2.5x10 $^{-5}$ s^{-1} reported by Zhou et al. (2003), and are also used for aerosol nitrate photolysis (described above). The scaling factor of 45 is also consistent with that used by Fu et al. (2019) and Liu et al. (2021), who calculate $J_{HNO_3,surf}$ with the following equation.

$$J_{HNO_3,surf} = \frac{3.4x10^{-5}}{7x10^{-7}} J_{HNO_3} \tag{3.9}$$

3.4x10 $^{-5}$ is the median $J_{HNO_3,surf}$ reported by Ye et al. (2016) and 7x10 $^{-7}$ is the average noontime $J_{HNO_3,gas}$.

3.2.1.4 HONO uptake, nocturnal storage, acid displacement

Uptake to the ground is an important loss for atmospheric HONO, especially at night. Once deposited, it forms surface nitrite through Reaction 1.15 and a similar reaction occurs with HNO_4. According to Vandenboer et al. (2015), this nitrite can be recycled back to gaseous HONO when displaced by a strong acid. In PACT-1D, it is assumed that all HONO and HNO_4 deposited to the ground is converted to nitrite. Every HNO_3 molecule deposited then results in a HONO molecule emitted to the lowest model layer. The uptake coefficients for HONO, HNO_4, and HNO_3 are 1x10 $^{-4}$, 0.01, and 0.1, respectively. To ensure there is a sufficient amount of nitrite present to be displaced, it's concentration is tracked and if it falls below a monolayer (~1x10 ^{13} molec cm^{-2}), the HONO source is scaled by $\frac{[NO_2^-]}{1x10^{13}}$.

3.2.1.5 Biogenic emissions

Oswald et al. (2013) determined that HONO can contribute up to 50% of reactive nitrogen released from soil, comparable to soil NO emissions. Soil NO emissions are included in the model as input. It is reasonable to assume that NO and HONO make up the majority of reactive nitrogen and therefore HONO emissions are set equal to NO, as an upper limit.

Results from the CalNex model runs are presented and discussed in Chapter 4. In particular, a HONO budget is constructed to evaluate the importance of the various heterogeneous mechanisms described in this section. The overall impact of HONO as an urban source of OH is also examined.

3.3 Model setup for FIREX-AQ study

As discussed in Section 1.3, HONO emissions from biomass burning and its chemistry within smoke plumes are not well constrained. PACT-1D is therefore used to simulate plumes sampled during the FIREX-AQ campaign in an attempt to better understand these processes. In particular, a major goal of this thesis is to determine the relative importance of HONO emissions versus secondary formation and how this changes as smoke is transported downwind. Additionally, plume measurements are generally recorded at a single altitude. PACT-1D can provide information on the vertical profile of HONO concentrations within smoke and help interpret observations. Since HONO plays such a key role in OH production, a detailed HONO budget can provide insight on the air quality impacts of biomass burning.

Simulations of two different fires from the campaign are performed and presented here. The Shady Fire was located at 44.54, -114.99 in Custer County, ID (36 km north of Stanley, ID) and sampled by the DC-8 on July 25, 2019. The Williams Flats Fire (WFF) was located at 47.94, -118.62 in Stevens County, WA (95 km northwest of Spokane, WA) and sampled on August 3, 2019. As with the CalNex model study, PACT-1D is initialized using

data from regional chemical and meteorological models (WRF-Chem, CAM-Chem) and from field measurements (Table 2.2). The vertical grid consists of 240 evenly spaced boxes of 25 m height, from the surface to 6000 m altitude. A top box of 1000 m height is also included, giving an upper boundary of 7000 m.

Each model run is started at the time of emission, which is calculated by subtracting the smoke age from the sample collection time (at the center of each transect). A trajectory analysis was performed by the Florida State University (FSU) team during FIREX-AQ using the HYSPLIT model (Stein et al., 2015) to determine smoke ages. HYSPLIT is run for all smoke measurements (on a 5 s time resolution) using 3 different meteorological datasets (NAM CONUS nest, HRRR, GFS). The trajectory closest to the fire is used to determine the smoke age. Although emission times vary between smoke sampled in consecutive transects, many measurements have an emission time within 1 hour of each other. An average emission time is therefore used for the PACT-1D model runs. The Shady Fire simulation starts at 23:15 UTC on July 25, 2019 and the WFF run starts at 23:30 UTC on Aug 3, 2019. A 20 second chemical time step is used and each fire is modeled for 6 hours, starting at the time of emission and following the plume downwind in a Lagrangian fashion.

The quick photolysis of HONO means that its cross-transect profile differs from many other species. Dilution occurs more readily at the plume edges, leading to lower aerosol concentrations and higher photolysis rates. This becomes more prominent as the plume ages and has been noted in other studies (Peng et al., 2020; Wang et al., 2021). Since there are differing chemical environments between the plume core and edges, this thesis focuses only on the plume center to better understand how HONO behaves with lesser influence from dilution. This can provide information on the transport of HONO emissions and whether they significantly impact downwind air quality. It also allows for a better comparison with mini-DOAS observations from the overpass flight segments, which generally attempted to fly along the plume center. The in-situ FIREX-AQ measurements used for PACT-1D initialization and validation are therefore from the plume center only. The center of each transect is

defined with the highest CO concentration and a 10 sec average is taken around this center point, corresponding to a distance of about 1500 m. Most DC-8 instruments used in this thesis have a 1 Hz time resolution.

In order to successfully model a biomass burning plume, modifications were made to PACT-1D, including the ability to simulate plume rise and dilution. Final model results are based on three consecutive model runs. First, a preliminary run was performed, initializing PACT-1D with background conditions to establish ambient trace gas concentrations over the 6 hour model period. Next, PACT-1D was run with CO fire emissions to establish the altitude of the plume and the dilution rate. Finally, fire emissions of all trace gases were included. Each model run is described below.

3.3.1 Background model run

WRF-Chem data is again used to define profiles of temperature, relative humidity, pressure, and the eddy diffusion coefficient (K_Z) over the 6 hour period for each model run. Biogenic emissions are based on the U.S. EPA's NEI dataset, which provides average monthly emissions of CO, VOCs, and NO_x (emitted solely as NO) for individual counties. These are emitted into the lowest box of the model. Since most of the fires sampled during FIREX-AQ were located in remote areas, anthropogenic emissions are not included. Background trace gas concentration profiles are initialized by combining observations from the upwind transect with data from the CAM-Chem model (Emmons et al., 2020; Buchholz et al., 2019). GOES-16 satellite images (https://www.nesdis.noaa.gov/content/imagery-data-0) were used to determine the start date of the fire and CAM-Chem data from the prior day was used to ensure background concentrations were not influenced by smoke.

The TUV radiation model (v5.0) was run for the specific location and time of each fire to calculate background air photolysis rates. Any influence of smoke (e.g., increased aerosol concentration) was excluded from the TUV model run. The NO_2 photolysis rate from TUV was scaled to the average value measured by the CAFS instrument during the

upwind transect. The same scaling factor was applied to all TUV output.

3.3.2 CO plume model run

A second run was performed, emitting only CO from the fire. A vertical advection scheme is implemented to loft the emissions to the correct plume altitude that was observed in the field. A horizontal mixing component is also added to PACT-1D, allowing the simulated plume to mix with background air.

3.3.2.1 CO emissions

CO emissions vary from fire to fire, depending on the fuel type, burning temperature, and fire size. The FIREX-AQ Fuel2Fire analysis team determined total carbon emissions (E_C) for each of the sampled fires using data from a number of sources. The Fuels Characteristics and Classification System (FCCS) (Ottmar et al., 2007) was used to determine fuel type, and fire detections from VIIRS, MODIS, and GOES satellite data were used to derive burned area. The diurnal profile of the emissions was defined using fire radiative power (FRP) from GOES. More analysis details are provided in Wiggins et al. (2021) and data is available on the FIREX-AQ website listed in Section 2.3. Figure 3.1 (top panels) shows the E_C diurnal profiles for the Shady Fire (left) and WFF (right). Most smoke sampled from the Shady Fire was emitted between 22:45 - 23:30 UTC on July 25, 2019 and for WFF, the emission times were primarily between Aug 3 23:15 and Aug 4 00:15 UTC. These time periods are shown in the bottom panels of Figure 3.1, with the red dashed line indicating the average value.

Most carbon in fuels is emitted as CO and CO_2 and their relative amounts are described by the modified combustion efficiency (MCE, Equation 1.19). In-situ measurements are used to determine the MCE for each fire, with an average of 0.90 for the Shady Fire and 0.91 for WFF. Starting with the average carbon emission values shown in Figure 3.1 (bottom panel),

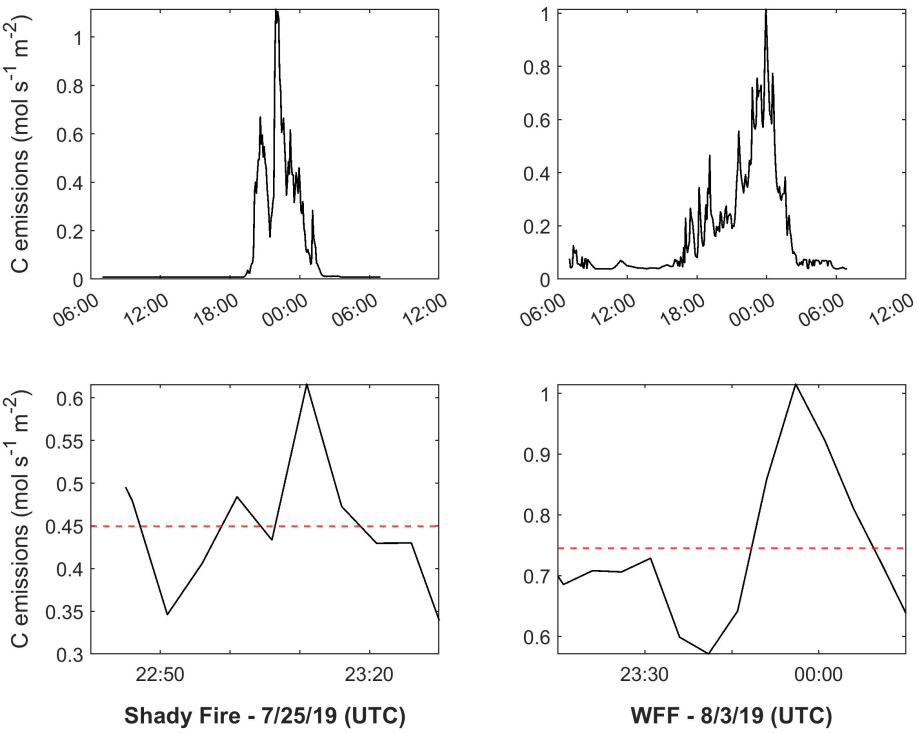

Figure 3.1: Carbon emissions calculated by the FIREX-AQ Fuel2Fire analysis team. The top panels show the entire diurnal profile for the Shady Fire (left) and Williams Flats Fire (right). Data starts at 6:00 UTC on the day of sampling. The bottom panels zoom in on the emission times relevant for the DC-8 sampling of each fire, with the average shown in the red dashed line

the MCE for each fire is used to calculate the PACT-1D CO emissions (E_{CO}). These were scaled until reasonable agreement was reached between the modeled and measured CO. E_{CO} was decreased by 10% for the Shady Fire and increased by 30% for WFF. The error reported in the Fuel2Fire data set is 40% for the Shady Fire and 37% for WFF so these adjustments are within the range of uncertainty.

3.3.2.2 Plume Rise

At the burning location, fires release a large quantity of heat along with trace gases and aerosols, creating a plume of hot and turbulent air that rises quickly. To simulate this process, an updraft speed (w) was added to PACT-1D's vertical mixing scheme (Equation 3.4). Vertical mixing, plume rise, and loss to the the ground (i.e. deposition) are now solved together in the new vertical mixing term.

$$F_{(i,t,z)} = \frac{\partial}{\partial t} C_{(i,t,z)} = \frac{1}{\rho_{(i,t,z)}} \frac{\partial}{\partial z} \left(\rho_{(i,t,z)} K_{D(i,t,z)} \frac{\partial}{\partial z} C_{(i,t,z)} \right) - w_{(t,z)} \frac{\partial}{\partial z} C_{(i,t,z)} + R_{(i,t)} \quad (3.10)$$

w is provided as an input parameter and estimated from field data, considering the altitude of the lofted plume and the time required to reach this height. For both fires studied here, a value of 7 m/s is used and applied during the first 6 minutes after emission, lofting the plumes 2-3 km above the ground surface which is consistent with observations. An updraft speed of 7 m/s is also supported by the FSU smoke trajectory analysis.

3.3.2.3 Plume dilution

As biomass burning plumes are transported away from the burning location, they are diluted through mixing with background air. This dilution is implemented in PACT-1D following Pugh et al. (2012), where the change in concentration with time is described as

$$\frac{DC}{Dt} = -\frac{2K_y}{D^2}(C - C_{bkgrd}) \quad (3.11)$$

where C is the concentration within the plume, c_{bkgrd} is the concentration in background air, D is the mixing depth (based on the model grid), and K_y is the horizontal turbulent diffusion coefficient. Results from the PACT-1D background run are combined with upwind transect

measurements to determine c_{bkgrd} for each species at each model time step and altitude. K_y is defined as an input parameter.

CO is a relatively inert tracer and often used to determine dilution rates of biomass burning plumes. K_y is therefore calculated from observed CO concentrations. Measurements taken during subsequent transects are used to determine the change in [CO] over time. Only transects at a similar vertical location within the plume are considered in this calculation to minimize the influence of vertical mixing. K_y strictly describes the horizontal mixing whereas K_Z describes the vertical mixing. The average [CO] from the upwind transect is used as the background.

Smoke measurements are only available at specific smoke ages, and in particular there is no CO data within the first 30-60 minutes after emission. To construct a K_y profile that varies with time, the calculated K_y values are interpolated to follow a similar dilution profile as the one reported in Wang et al. (2021). They performed high resolution large eddy simulation (LES) modeling for WFF and found that dilution rates decrease about an order of magnitude over the first few hours after emission. Tests were done in PACT-1D to ensure the model reasonably captured the observed decrease in CO with time, adjusting the K_y values slightly when needed. Figure 3.2 shows the temporal K_y profile used in the WFF PACT-1D model run. These values are for the free troposphere where the plume is lofted. Within the boundary layer, where mixing is stronger, K_y values are increased by a factor of 10 (Pugh et al., 2012). Similar values are used for the Shady Fire.

3.3.3 Full plume model run

A final run is performed which includes emissions of all species. The aerosol properties and photolysis rates (both defined in model input) are also updated to account for the influence of smoke. The altitude range of the plume is determined by the CO concentration from the previous run. Any model box with with [CO] greater than 300 ppb is considered to be within the plume.

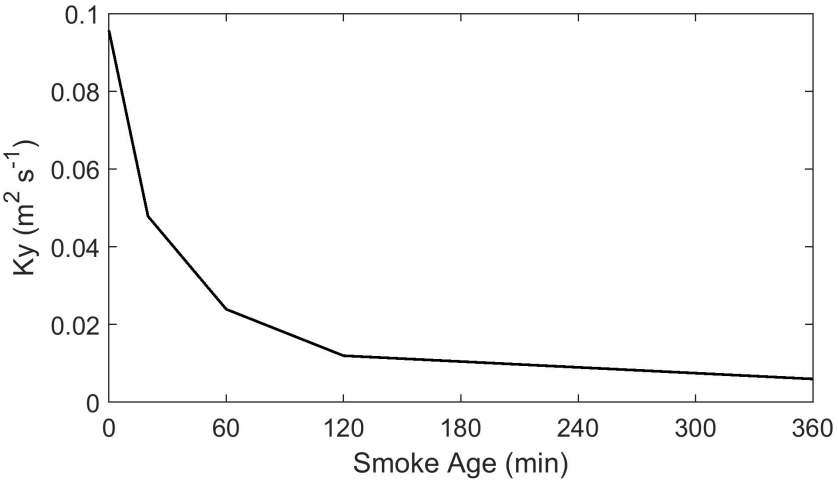

Figure 3.2: Horizontal turbulent diffusion coefficient (K_y) for the WFF model run. K_y describes the degree of mixing between the plume and the background air.

3.3.3.1 Trace gas emissions

As discussed in Section 1.3, trace gases are often quantified in smoke as normalized enhanced mixing ratios (NEMRs, Equation 1.17) and measurements close enough to the fire can be used as emission ratios (ERs). Measurements from the first transect downwind of the fire are therefore used to determine emissions in PACT-1D.

$$E_X = ER_X \times E_{CO} \tag{3.12}$$

HONO and NO_2 emission ratios were also reported from the mini-DOAS instrument. These are averaged with the in-situ ERs to calculate PACT-1D emission values. Table 3.1 lists the ERs used in PACT-1D for select trace gases that are most relevant for this work. For WFF, the NO and NO_2 ratios were increased by 20% compared to observed ERs in order to obtain better agreement between modeled and observed NO_x.

For species not measured on the DC-8, literature emission factors (EFs) from Andreae

Species	**Shady Fire ER (ppb X / ppb CO)**	**WFF ER (ppb X / ppb CO)**
HONO	0.0027	0.0020
NO_2	0.0049	0.0061
NO	0.0016	0.00094
HCHO	0.0234	0.0139
ACD	0.0141	0.0095

Table 3.1: Emission ratios for select trace gases used in PACT-1D model runs.

(2019) are used. These are reported for temperate forests as the amount of trace gas X (in g) emitted per kg of dry fuel burned.

$$E_X = EF_X \times E_C \times \frac{MW_C}{MW_X} \times \frac{1}{F_C} \tag{3.13}$$

Note that the total carbon emission (E_C) is used in this equation, not E_{CO}. F_C is set at 0.5 and the 1/1000 factor is to convert between kg and g. For particle nitrate (pNO_3), an EF of 0.547 is used, averaging three values from field and laboratory studies (May et al., 2014; Liu et al., 2017).

3.3.3.2 Aerosol properties

Aerosol concentrations, defined as input in PACT-1D, are much higher in smoke than in background air. Although there are in-situ measurements from NASA's LARGE instrument, these are only reported at a single altitude for each transect. A vertical profile of aerosol surface area (SA) is calculated based on the modeled plume in the PACT-1D CO plume run. The plume location is identified using [CO], and SA is calculated based on these concentrations. The relationship between [CO] and SA is determined from measurements

and a linear correlation between the two is used to define SA in PACT-1D. Although aerosol physics is extremely complex in biomass burning plumes, this gives a reasonable approximation of the total surface area that impacts heterogeneous reactions in the model. Figure 3.3 shows the surface area values used in the PACT-1D initialization for each fire, for smoke ages from 10-120 minutes. The initial plume rise and later smoke ages are not shown for scaling reasons. The circles show the transect observations, which agree fairly well with the model values. Since PACT-1D does not capture plume dynamics, the location of the measurements are approximated using a method that will be described in Chapter 5.

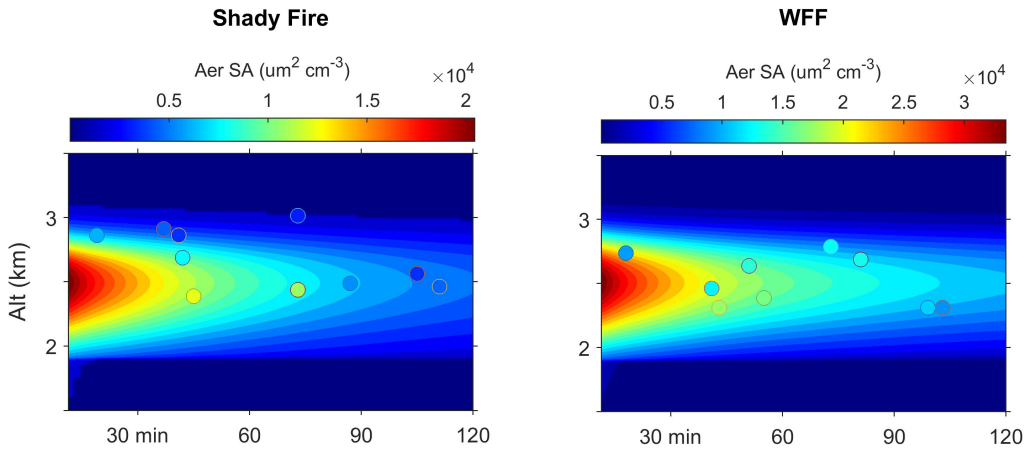

Figure 3.3: Initialized aerosol surface area for the first 2 hours of the Shady Fire (left) and WFF (right) model runs. The circles show measurement values from the LARGE instrument, with altitude approximated within the modeled plume.

3.3.3.3 Plume photolysis rate profiles

The large amount of aerosol present in biomass burning plumes have a significant impact on photolysis rates. To accurately represent the vertical profiles of these rates, results from the VLIDORT-QS RTM are used to parameterize the vertical variability. VLIDORT-QS and its role in interpreting FIREX-AQ measurements were briefly described in Section 2.3.2. The parameterization used in PACT-1D is based on a bidirectional sigmoid function that

accounts for both upwelling and downwelling radiation.

$$J(z) = J_{down}(z) + J_{up}(z) \tag{3.14}$$

$$J_{down}(z) = \frac{J_t - J_{min}}{1 + e^{(z' - z)/F}} + J_{min} \tag{3.15}$$

$$J_{up}(z) = \frac{J_b}{1 + e^{(z - z'')/F}} \tag{3.16}$$

$J(z)$ is the photolysis rate at altitude z, $J_{down}(z)$ and $J_{up}(z)$ are the downwelling and upwelling components, J_t and J_b are the J rates at the top and bottom of the plume, and J_{min} is the minimum J rate in the plume center. $z^{'}$ is the offset altitude where $J(z) = (J_t + J_{min})/2$ and $z^{''}$ is the offset altitude for the upwelling radiation. F controls the slope of the photolysis profile.

Measurements from the CAFS instrument are used to determine the J_t, J_b, and J_{min}. In addition to photolysis rates, CAFS data also includes the relative signal from downwelling and upwelling to the total actinic flux. From these measurements we determine that clear sky J values consisted of 80% downwelling radiation and 20% upwelling, therefore J_t is set to 80% of the upwind clean air J value and J_b is set to 20% of this value. As the plume ages and dilutes, J rates steadily increase. Within the model, the J rate profiles are kept constant for the first 90 minutes after emission and then J_t, J_b, and J_{min} steadily increase based on the rate seen in the CAFS measurements. The HONO photolysis rates used in the WFF model runs are shown in Figure 3.4.

3.3.3.4 HONO chemistry

The focus of this thesis is on chemistry in lofted biomass burning plumes. Because of this, the surface chemistry at the ground (Section 3.2.1) does not play a significant role in the HONO

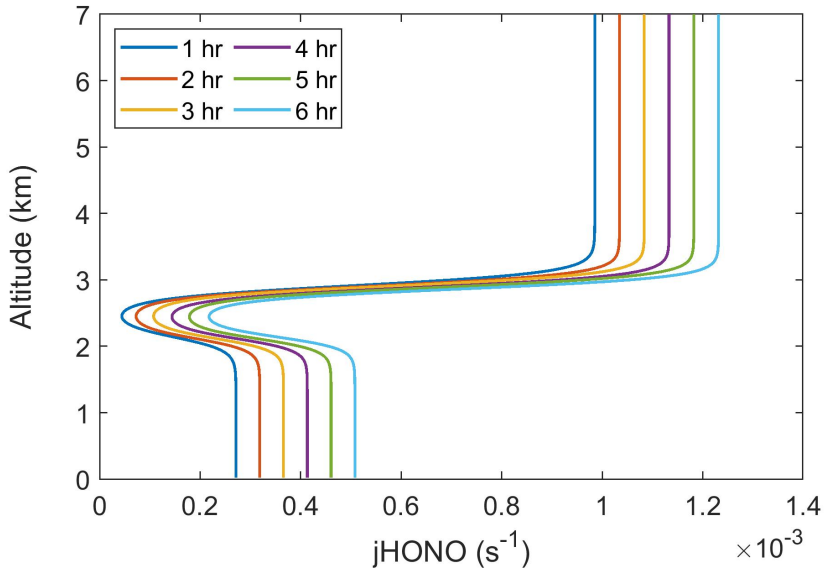

Figure 3.4: Vertical profile of the HONO photolysis rates used as PACT-1D input for the WFF model run. Highest values are seen above the plume (located between 2-3 km). Rates decrease quickly within the plume due to significant light extinction by aerosols. A minimum value is seen in the plume center and higher values are seen at the plume bottom due to some influence from upwelling radiation. Each line represents a different smoke age. As the plume dilutes with smoke age, photolysis rates increase.

budget. The large concentration of particles, however, indicate that heterogeneous HONO formation on aerosols may be important. In addition to the photolysis of particle nitrate that was included in the CalNex model setup, NO_2 hydrolysis and the photo-enhanced NO_2 conversion to HONO on aerosols are added to the mechanism.

The NO_2 reactive uptake coefficient is increased to $1x10^{-3}$ based on studies by Alvarado and Prinn (2009) and Wong et al. (2013). This value is on the high end of what is reported in literature so it should represent an upper limit of HONO formation. The hydrolysis reaction requires 2 molecules of NO_2 to produced HONO (Reaction 1.8) and the photo-enhanced mechanism is 1 to 1. Similar to the photo-enhanced implementation described in Section 3.2.1, the reactive uptake is parameterized based on the NO_2 phtotolysis rate, following

Wong et al. (2013).

$$\gamma_{NO_2,photo} = 1x10^{-3}\frac{J_{NO_2}}{J_{NO_2,noon}} \tag{3.17}$$

The pNO_3 photolysis rate is again set at 45 times the rate of gas-phase HNO_3. The partitioning between gas phase HNO_3 and pNO_3 is updated in the mechanism based on data from the aerosol group at CU Boulder. The pH of the aerosols within the sampled plumes was higher than in background air, shifting the HNO_3/pNO_3 partitioning strongly towards the particle phase, with $\epsilon(NO_3^-)$ (Equation 3.5) values close to 100%.

Results from the FIREX-AQ model runs will be presented and discussed in Chapter 5. Modeled values are compared to in-situ and mini-DOAS measurements and the HONO budget is investigated to determine how HONO chemistry evolves with smoke age.

CHAPTER 4

CalNex model results and discussion

PACT-1D was used to simulate HONO levels during the CalNex campaign and analyze the importance of heterogeneous ground sources in an urban setting. Five model runs were performed, including an initial run without HONO ground chemistry, a base run including these HONO sources, and four sensitivity tests to investigate the uncertainties in the heterogeneous mechanisms. An overview of each model run is provided in Table 4.1 and each is discussed below. PACT-1D results are compared to observations to validate model performance and the HONO vertical profile and budget are used to determine the strength of each ground source and how they impact OH formation.

4.1 Model run without HONO surface chemistry (NoSurf run)

A model run (NoSurf) was first performed to investigate HONO concentrations without ground surface chemistry. In this run, HONO was impacted by gas phase chemistry, direct emissions, deposition to the ground (with an uptake coefficient of 1x10 $^{-4}$), uptake on aerosol surfaces (with an uptake coefficient of 1x10 $^{-3}$), and formation from aerosol nitrate photolysis. HONO levels at 3 m were compared to the NI-PT-CIMS measurements (Figure 4.1, bottom right). Modeled HONO, shown in orange, remained around 0.1 ppb or lower during daytime periods, with May 28 and 29 showing a slight early morning peak between 0.15-0.3 ppb. Daytime and nighttime concentrations for all three days were significantly lower than observations. The modeled HONO vertical profiles are also severely underestimated (Figure 4.3), indicating that HONO chemistry in this model run (gas phase formation, direct emis-

Model Run	Description
NoSurf	HONO chemistry on the ground not included
Base	HONO chemistry on the ground included
Sens1	$\gamma_{NO_2,max}$ decreased by 50%, $J_{HNO_3,surf}$ increased by 25%
Sens2	$\gamma_{NO_2,max}$ increased by 2x, $J_{HNO_3,surf}$ decreased by 20%
Sens3	$\gamma_{NO_2,max}$ decreased by 90%, $J_{HNO_3,surf}$ increased by 60%
Sens4	$\gamma_{NO_2,max}$ increased by 5x, $J_{HNO_3,surf}$ decreased to gas phase J_{HNO_3}

Table 4.1: Overview of PACT-1D model runs

sions, and aerosol nitrate photolysis) cannot completely explain HONO levels and that an additional source is required.

4.2 Model results with interactive surface chemistry (Base run)

When the heterogeneous HONO formation sources described in Section 3.2.1 were implemented in PACT-1D (Base run), the model matched observations much better (Figure 4.1). The model captures the general trend and values of major species including NO_x, HO_x, and O_3. Due to lack of horizontal advection in PACT-1D, however, there are some discrepancies related to changes in air mass, for example near midnight on May 30. The model also misses some of the afternoon NO_x peaks, which are due to advection of polluted air from downtown Los Angeles. These dates correspond to the start of the Memorial Day holiday weekend as well, making traffic emissions more difficult to estimate.

The overprediction of OH and underprediction of HO_2 in PACT-1D is consistent with results from Griffith et al. (2016) and is likely due to missing radical processes in the RACM2 mechanism. Griffith et al. (2016) suggests that reactivity between OH and saturated hydrocarbons, and OH and aldehydes, is underpredicted in the mechanism, leading to an overprediction of OH and under prediction of HO_2. Similar results were reported by Wolfe

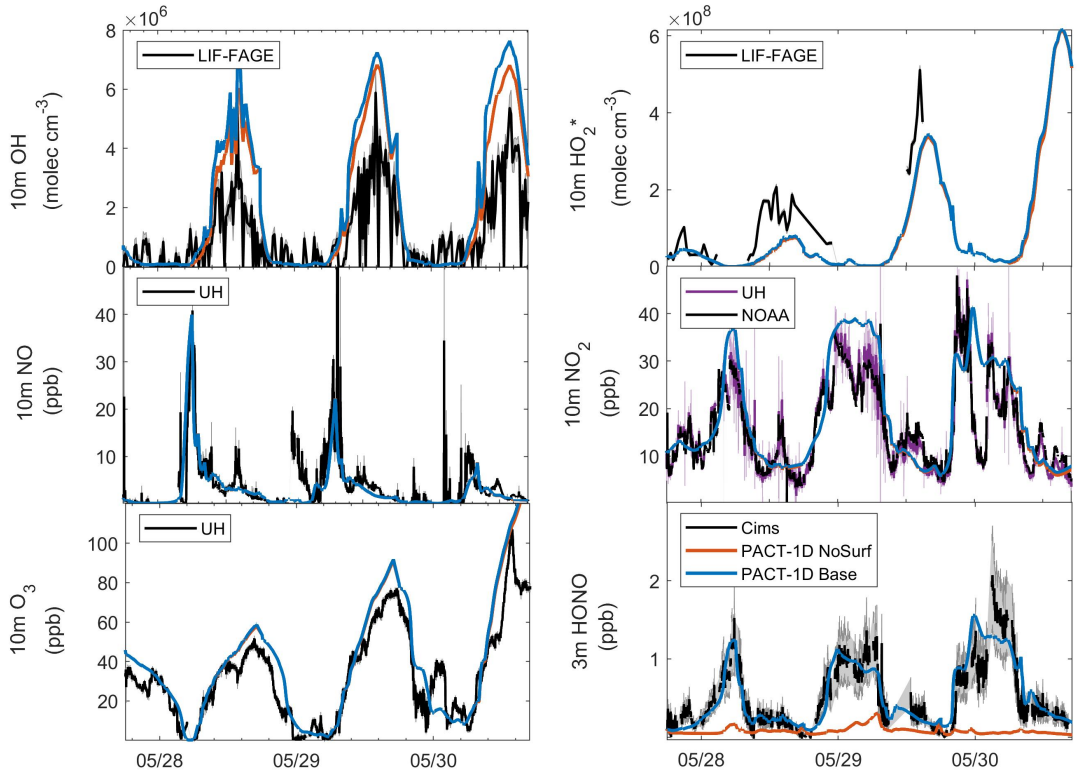

Figure 4.1: Overview plot showing NoSurf (orange) and Base (blue) model results compared to observations from May 27, 2010 18:00 through May 30, 2010 18:00. Measurement details are included in Table 2.1. HO_2* is HO_2 + 0.3RO_2, following Griffith et al. (2016).

et al. (2016), who found that production of HO_2 from reactions of OH with HCHO, CO and other hydrocarbons was too slow in the RACM2 mechanism to accurately capture OH and HO_2 observations.

The diurnal HONO trend is captured in the Base run, showing mixing ratios increasing over night, followed by a sharp decrease in the early morning. Concentrations are substantially higher compared to the NoSurf run, with daytime values ranging between 0.1-0.5 ppb and night time values increasing to 1.2-1.6 ppb. Modeled HONO does not capture the early morning peaks around 6:00-7:00 on May 29 and 30. This and the delayed decrease in HONO

during the morning of May 30 indicate that the morning mixing may not be completely accurate in the model. A delay in morning boundary layer growth can prevent HONO formed overnight from mixing away from the surface. The quick changes in observed O_3, NO_2, and NO also indicate that there are air mass changes that the model cannot capture. Overall, these results show very good agreement between model and observations and show that a heterogeneous HONO surface source is necessary to simulate realistic atmospheric HONO levels. The mechanisms implemented here appropriately describe this heterogeneous source during CalNex.

4.3 HONO vertical profiles

Since HONO photolyzes quickly during transport away from the ground where it is formed, vertical profiles must be considered to understand HONO's sources and its total impact to air quality in the boundary layer. Observed profiles were constructed by vertically interpolating between the NOAA NI-PT-CIMS measurements at 3 m and the LP-DOAS measurements at 55.5 m, 99.5 m, 188 m, and 405.5 m. The NI-PT-CIMS and LP-DOAS instruments showed excellent agreement in another field experiment (UBWOS 2012), and therefore can be combined to construct vertical concentration profiles of HONO confidently. Figure 4.2 shows the observed profile compared to PACT-1D for the entire 3 day period and Figure 4.3 shows select hours between May 27 18:00 and May 28 17:00.

In the observed profile, the highest HONO concentrations are typically at the surface, which is consistent with vertical profiles measured in other field campaigns (Kleffmann et al., 2003; Villena et al., 2011; Wong et al., 2011, 2012; Young et al., 2012; Vandenboer et al., 2013; Tsai et al., 2018). The quick decay in HONO with altitude in the lowest 100 m, especially during the day, emphasizes the importance of vertical profile measurements and modeling. HONO's role in boundary layer chemistry can easily be over or under estimated if measurements at a single altitude are used. In particular, this can have a significant impact

on OH production rates, which will be discussed in the following section. These profiles provide evidence for a ground source of HONO and the underestimation in the NoSurf run (Figure 4.3 right) shows that direct emissions cannot be the primary ground source. The implementation of heterogeneous sources are the cause for more accurate HONO levels, both near the surface and at higher altitudes.

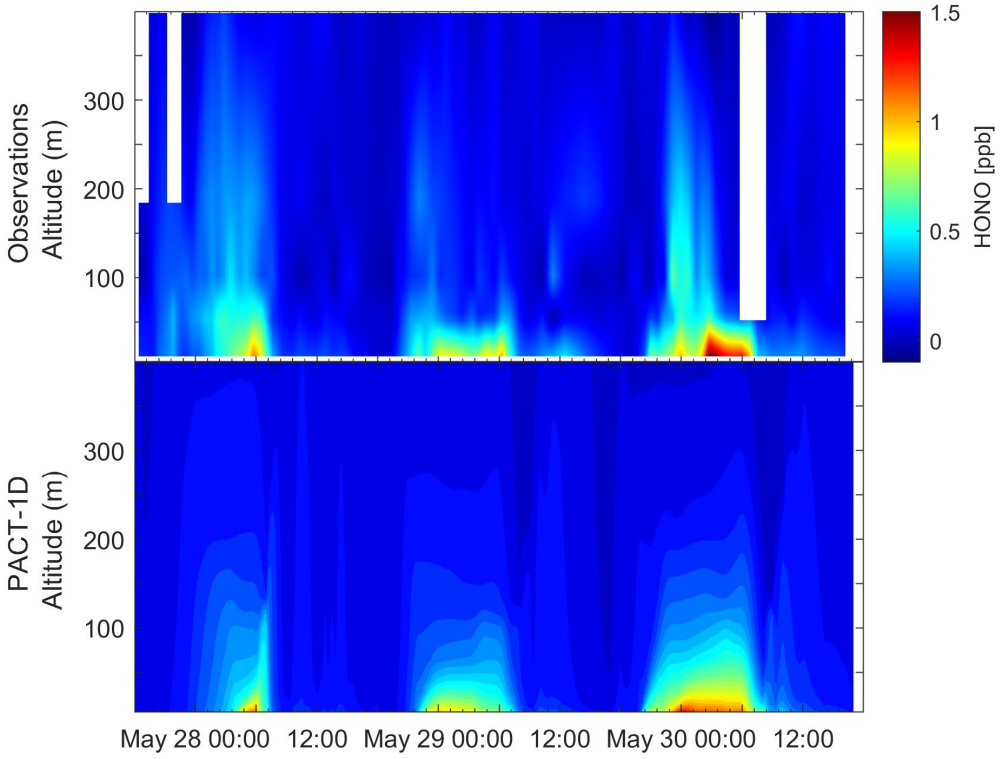

Figure 4.2: Comparison of HONO vertical concentration profiles between observations (top) and model (bottom), from May 27 18:00 to May 30 17:00. The observed profile is constructed from LP-DOAS and NI-PT-CIMS data.

The underestimation of HONO in the NoSurf run (Figure 4.3, right), which includes aerosol nitrate photolysis as the only heterogeneous HONO source, also shows that aerosols are less significant than ground sources. pNO_3 photolysis shows a diurnal trend, peaking in the early afternoon and decreasing to zero at night. In the Base run, the source peaks near

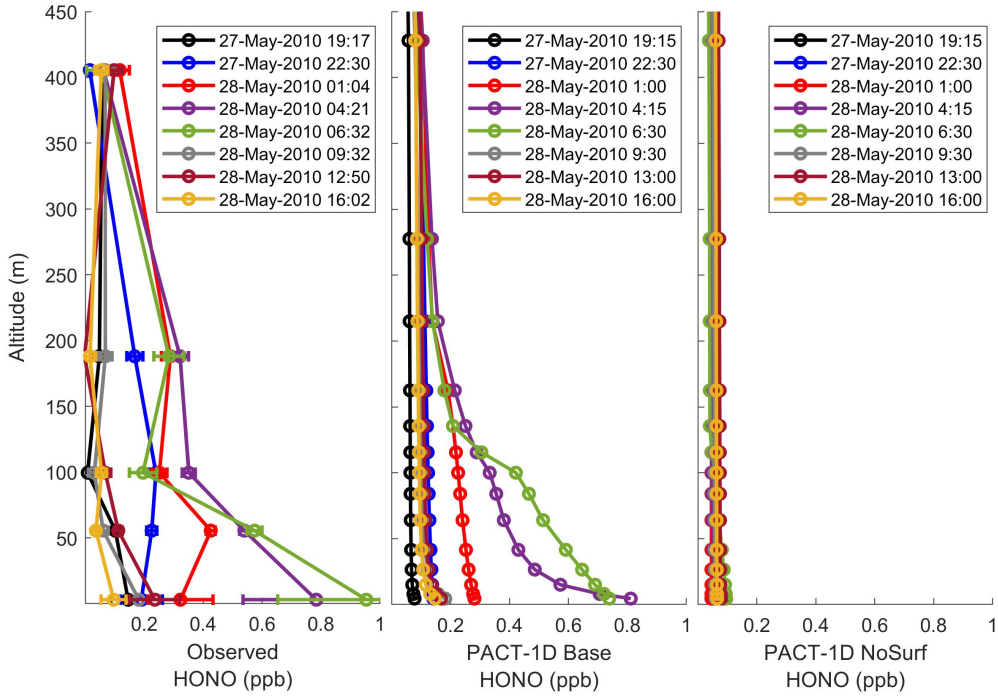

Figure 4.3: Comparison of HONO vertical concentration profiles between observations and model from May 27 to 28. The left panel is the observed profile, the middle is the PACT-1D Base run including surface chemistry, and the right panel is the PACT-1D NoSurf run excluding surface chemistry. The observed profile is constructed from LP-DOAS data (top four data points) and NOAA NI-PT-CIMS data (lowest data point).

7x10^{5} molec cm^{-3} s^{-1} on May 28, 9x10^{5} on May 29, and 8x10^{5} on May 30, within the LP-DOAS altitude range (50-400 m). Lower values on May 28 are due to smaller photolysis rates and lower aerosol number concentrations. pNO_3 concentrations are also under predicted on this day compared to observations so the values reported by PACT-1D are likely too low. On May 29, modeled pNO_3 levels are slightly higher than observed, indicating that the HONO aerosol source may be slightly over predicted on this day as well.

Overall, the values reported are generally consistent with other studies in urban areas, including Wong et al. (2013) who reports noontime values of 1.0-1.7x10^{6} molec cm^{-3} s^{-1} in

Houston, Texas. The CalNex values are lower than those in more polluted cities with larger available aerosol surface area. Liu et al. (2021), for example, found approximately 1 ppb hr^{-1} (6.9x10 ^{6} molec cm^{-3} s^{-1}) of HONO could be formed from aerosol sources at noon in Beijing in summer. The higher rates in Beijing are likely due to the higher aerosol loading in that study.

Net vertical transport of HONO from below can provide a source of HONO aloft. These rates are variable from day to day but, in general, are greater than or about equal to HONO production from aerosol nitrate. For most of the three day period, the primary source of HONO below 500 m is upward transport from the surface (Figure 4.4). The large difference in surface area between aerosols and the ground can explain the greater importance of ground versus sources and is in agreement with other studies (Kalberer et al., 1999; Kleffmann et al., 2003; Vogel et al., 2003; Stemmler et al., 2007). Compared to observations, daytime HONO levels between 50-400 m in the Base run tend to be slightly over predicted. This may indicate that the sources aloft (formation on aerosols and transport from below) are too high. There is uncertainty in the photolysis rate for the aerosol source in the model, and the vertical transport from the ground. Consequently, it is currently unclear which process is responsible for the disagreement.

4.4 Primary HO_x production

To determine the importance of HONO to the radical budget, primary HOx production (P_{HOx}) was calculated for the Base run and measurements. Three major primary HO_x production pathways are considered: HONO photolysis, HCHO photolysis, and O_3 photolysis followed by reaction of $O(^1D)$ with H_2O. Since HONO levels change quickly with altitude, as seen in the previous section, vertical profiles are used to calculate P_{HOx}. In addition to HONO measurements, the LP-DOAS observed vertical profiles of HCHO and O_3. These were combined with the 3 m NI-PT-CIMS measurements of HONO, and the University of

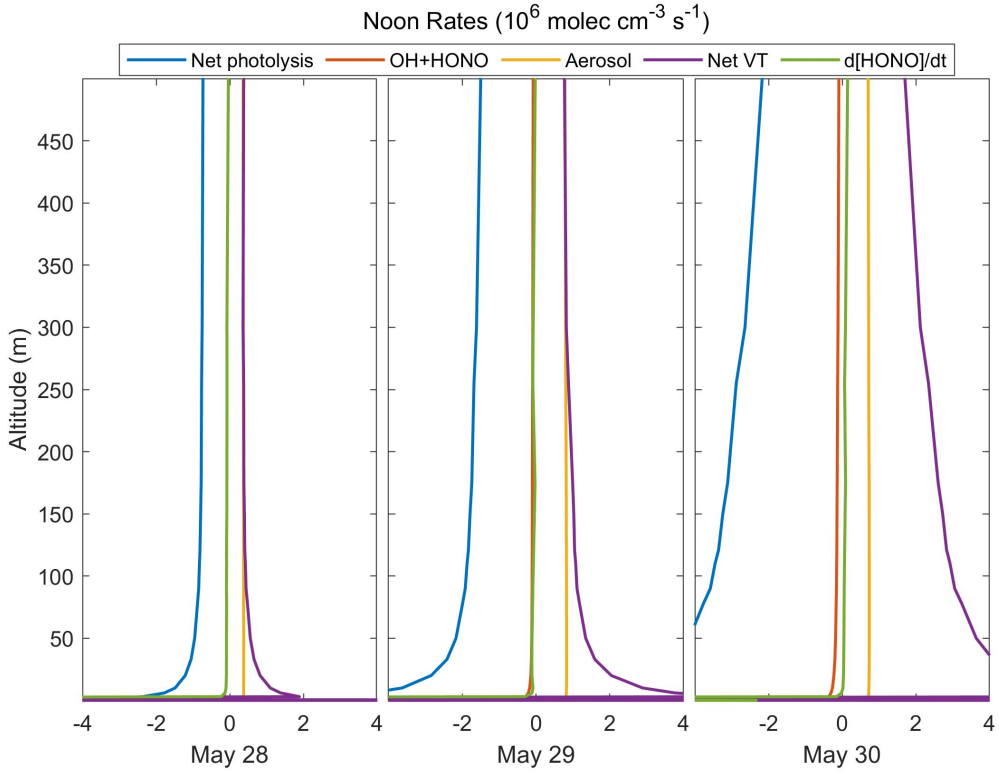

Figure 4.4: Noon time HONO budget for May 28 (left), 29 (middle), and 30 (right) from the Base run. Rates are reported in molec cm^{-3} s^{-1} and include net photolysis (HONO photolysis minus formation from the OH+NO reaction), loss via the HONO+OH reaction, formation from aerosol nitrate photolysis, net vertical transport, and the HONO concentration change with time.

Houston's (UH) 10 m O_3 measurements to construct concentration profiles. 10 m measurements of photolysis rates, temperature, and relative humidity (Table 2.1) were used to calculate P_{HOx}, assuming the values are constant over the altitude range considered here (0-450 m). Figure 4.5 shows vertical profiles of P_{HOx} from observations (solid lines) and PACT-1D (dashed lines). These values are averages from 10:00 am - 12:00 pm on May 28, 2010.

In both the model and observations, the contribution to P_{HOx} from HCHO and O_3 remains relatively constant with height, with higher values for O_3. PACT-1D underestimates P_{HOx}

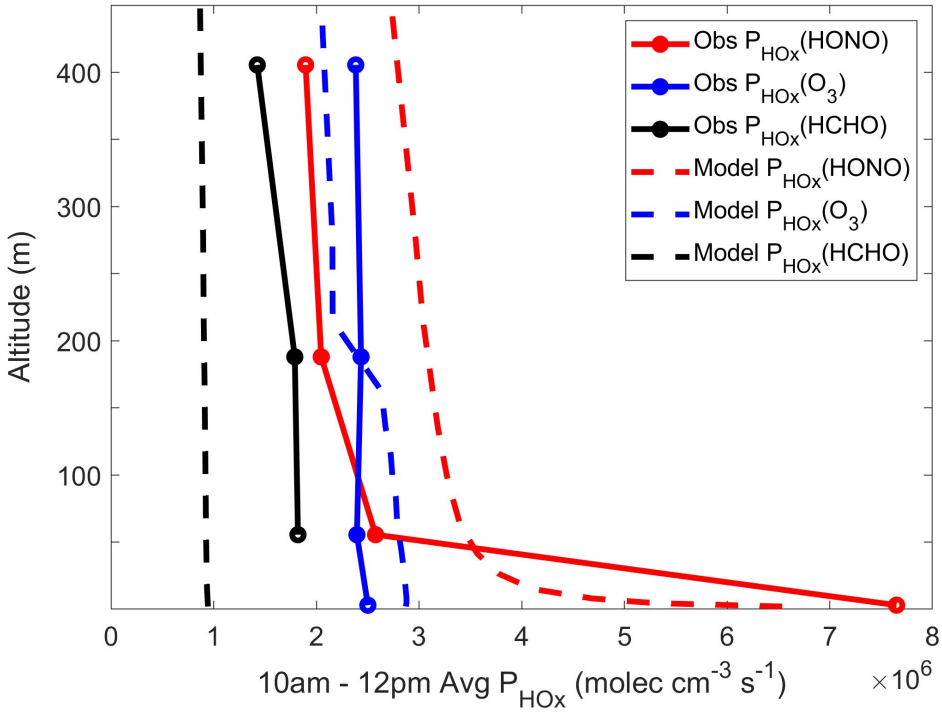

Figure 4.5: Primary HO_x production due to HONO (red), O_3 (blue), and HCHO (black). Observations are shown as dotted lines and model data from the Base run is shown as solid lines. Values are averaged between 10am-12pm on May 28, 2010.

from HCHO compared to the observations, but captures the O_3 contribution well. Comparing HCHO LP-DOAS measurements to the model shows that PACT-1D under predicts HCHO levels at these altitudes, which leads to the under prediction of P_{HOx}(HCHO).

Both observations and PACT-1D show that HONO photolysis is dominant near the surface, contributing 2-3 times more than O_3 below 10 m. P_{HOx}(HONO) decreases quickly moving away from the surface, following the trend seen in the HONO concentration profile. PACT-1D underestimates P_{HOx}(HONO) compared to the observations at the surface by about 15%, and over predicts at higher altitudes by 25-35%. The model also underestimates HONO concentrations at the surface and over predicts them aloft during this time period (Figure 4.3) which can explain this difference in P_{HOx}(HONO). The discrepancy between

model and observations, for both the concentration and P_{HOx}(HONO), is likely due to the high sensitivity of HONO to the vertical mixing or an over prediction of the HONO aerosol source, as discussed above. The influence of HONO on P_{HOx} leads to slightly higher daytime OH concentrations at lower altitudes (Figure 4.6). When HONO ground sources are excluded from the model (NoSurf run), OH concentrations are reduced, particularly at the surface, flattening the profile. An accurate representation of HONO levels and its heterogeneous sources can cause a 20-60% increase in OH below 10 m in the morning and a 10% increase in the afternoon.

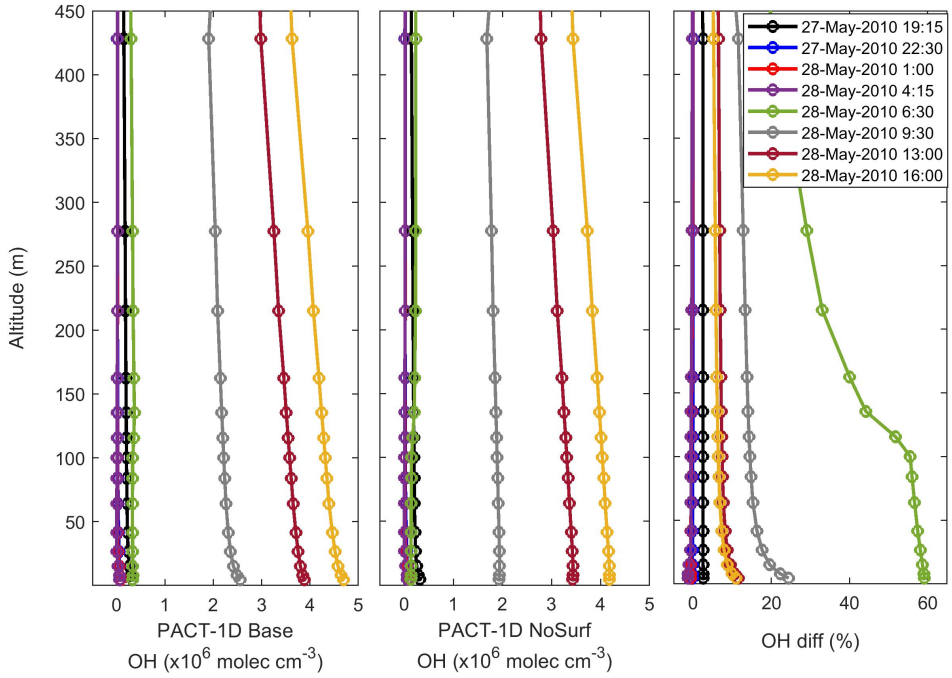

Figure 4.6: Comparison of OH vertical concentration profiles between the Base model run (left) and NoSurf run (center) from May 27 to 28. The right panel shows the percent difference between the two.

A study by Griffith et al. (2016) found that during the CalNex campaign, HONO photolysis contributed 26% to the total radical production rate on weekends and holidays and 29% on weekdays. Using these average values, their P_{HOx}(HONO) between 10:00 am and

12:00 pm ranged from about 5x10^{6} and 8x10^{6} molec cm^{-3} s^{-1}. They note that these values are most appropriate for 10 m altitude where measurements were recorded, and are consistent with the values reported here at low altitudes. HCHO photolysis contributed 9-10% to the total radical production, giving rates between 1.5x10^{6} and 3x10^{6} molec cm^{-3} s^{-1}. The observations reported here are in agreement with these values, but again PACT-1D under predicts P_{HOx}(HCHO) due to the HCHO concentration being too low. O_3 photolysis contributed 11-14%, with rates of 2x10^{6}-4.5x10^{6} molec cm^{-3} s^{-1}, matching the values in this study well.

4.5 HONO source mechanisms

The HONO surface formation mechanisms added to PACT-1D in the Base run provided an additional source of up to 2.5x10^{11} molecules cm^{-2} s^{-1} during the day and up to 5x10^{10} molecules cm^{-2} s^{-1} during the night. Figure 4.7 shows the source rate for the three day model period, including the contributions from individual mechanisms. Values remained relatively constant throughout each of the nights around 1x10^{10} to 5x10^{10} molecules cm^{-2} s^{-1} and then increased quickly in the early morning as photolytic formation mechanisms become effective.

The source rates reported here are higher than those from other field studies, which include a forest canopy (Zhang et al., 2009; Zheng et al., 2011), an agricultural site (Ren et al., 2011), and polluted rural site (Tsai et al., 2018). These studies have average noontime fluxes between 1x10^{10} to 3x10^{10} molecules cm^{-2} s^{-1}, measured at 10-20 m altitudes. The PACT-1D surface flux is provided directly at the ground which likely explains the higher values. Loss of HONO through photolysis and deposition back to the ground decreases the amount that is transported to higher altitudes. The flux of HONO across 10 m in the model was therefore calculated, giving noontime values of 5x10^{10} molecules cm^{-2} s^{-1} for May 28 and 29 and 1.1x10^{11} molecules cm^{-2} s^{-1} for May 30. These are in better agreement with previous studies. The CalNex urban site likely has a higher HONO source than the other

listed studies due to higher NO_2 concentrations and deposition, and higher surface HNO_3 concentrations.

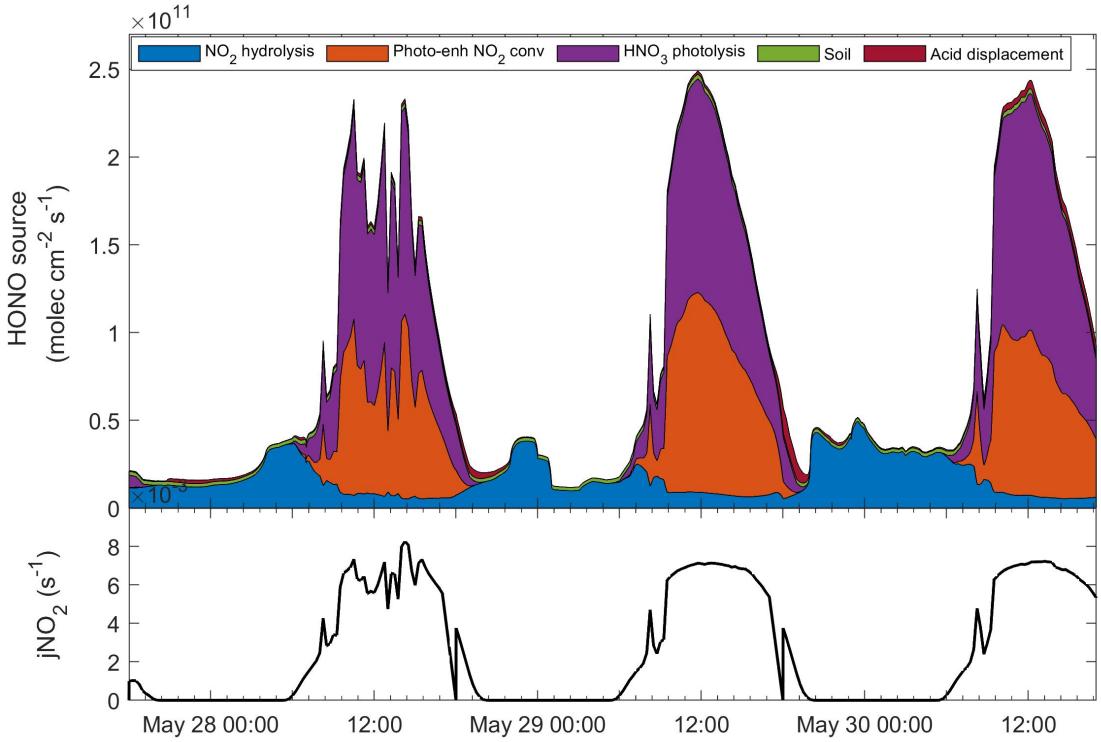

Figure 4.7: Contribution of individual mechanisms to the total HONO surface source in the Base run, from May 27, 2010 18:00 through May 30, 2010 17:00. The 10 m NO_2 photolysis rate for the 3 day period is shown in the lower panel as an indication of light availability.

The night time source was dominated by hydrolysis of NO_2, which is consistent with previous studies (Kleffmann et al., 2003; Wong et al., 2011; Vandenboer et al., 2013). Photolysis of surface HNO_3 dominated throughout the day, contributing 45-60% of the total source during mid-day. Photo-enhanced conversion of NO_2 was also significant, contributing 20-45% of the daytime source (Figure 4.7).

Previous studies have suggested that the photo-enhanced conversion of NO_2 is the dominant heterogeneous mechanism under high-NO_x urban conditions while the photolysis of

surface HNO_3 is more important under low-NO_x conditions (Zhou et al., 2003; Elshorbany et al., 2012). The opposite is seen during CalNex. Pusede et al. (2015) examined how HONO levels during the CalNex campaign changed compared to NO_x and found daytime HONO production did not vary with weekday/weekend changes in NO_2. They suggested therefore that NO_2 conversion is not the dominant HONO formation pathway. Although HNO_3 can also show a dependence on NO_x levels, its deposition and subsequent photolysis occur on a longer time scale which would not necessarily correlate with atmospheric NO_2 levels. Baergen and Donaldson (2016) suggests that HNO_3 photolysis on urban grime and its dependence on relative humidity would also cause a discrepancy between NO_2 and HONO production. The results here therefore support the findings by Pusede et al. (2015) that NO_2 conversion is not the primary source of HONO in Los Angeles.

It is currently unclear however, why these differ from the study performed by Wong et al. (2013) in Houston, Texas. They found that photo-enhanced NO_2 conversion was the dominant HONO source based on a clear correlation between HONO and NO_2 levels. It is possible that surface HNO_3/NO_3^- concentrations are higher in Los Angeles, giving more importance to its photolytic source. The scarcity of significant rain events in Southern California may cause a buildup of HNO_3 on surfaces, whereas the much more frequent precipitation in Houston can lead to surface adsorbed species being washed away. Guo et al. (2017) did find that particle nitrate and HNO_3 concentrations during CalNex were higher than measurements from summertime campaigns in the southeast United States. They suggest this is due to the higher NO_x versus SO_2 sources in southern California. This leads to a higher NO_3^- to SO_4^{-2} ratio in particles, which raises the pH. The higher pH then creates a positive feedback which forms more NO_3^-. Although Guo et al. (2017) focused on particles, it is possible that similar chemistry is occurring at the ground as well. The results from this study show that HNO_3 photolysis should be considered as an important HONO source in certain urban areas and may be especially important in regions with low precipitation and high NO_x emissions.

4.6 Source sensitivity to uptake coefficient and photolysis rate

Although there has been significant research into HONO heterogeneous formation in recent decades, many of the related chemical mechanisms and rates are not well constrained. Sensitivity tests were therefore performed to better understand how the daytime surface source is impacted by these uncertainties. The goal for these tests was to determine if the balance between the two major daytime mechanisms, the photo-enhanced conversion of NO_2 and the photolysis of surface HNO_3, could be adjusted and still provide a sufficient HONO source to match observations. Uncertainties in the maximum reactive uptake coefficient ($\gamma_{NO_2,max}$) and the photolysis rate enhancement of surface HNO_3 ($J_{HNO_3,surf}$) compared to the gas phase are addressed. Results from the sensitivity tests (Figure 4.8) are compared to the Base model run and a description of the changes made for each test are included in Table 4.1.

- Sens1 - To address the impact of uncertainties in $\gamma_{NO_2,max}$, its value was reduced by 50% in Sens1. A corresponding increase in $J_{HNO_3,surf}$ by 25% was then needed to maintain a surface source similar to the Base run. The noontime surface source increased from 1.6x10 ^{11} in the Base run to 1.9x10 ^{11} molecules $cm^{-2}\,s^{-1}$ in Sens1. The contribution of photo-enhanced NO_2 conversion at noon decreased from 32% of the total source in the Base run to 26%. The contribution from surface HNO_3 photolysis increased from 60% in the Base to 65%.

- Sens2 - Doubling $\gamma_{NO_2,max}$ required reducing $J_{HNO_3,surf}$ by 20% to maintain a surface source consistent with the Base run. This run again led to good agreement with the Base run, with the total source decreasing slightly to 1.5x10 ^{11} molecules $cm^{-2}\,s^{-1}$. The contribution of photo-enhanced NO_2 conversion at noon increased to 39% and the contribution from surface HNO_3 photolysis decreased slightly to 58%.

- Sens3 - Reducing $\gamma_{NO_2,max}$ by 90% and increasing $J_{HNO_3,surf}$ by 60% caused the 3 m HONO concentration and the total HONO source to become slightly larger. The

concentration though is still within the margin of error of the HONO NI-PT-CIMS measurements.

- Sens4 - To test if the photo-enhanced NO_2 conversion could contribute the majority of the ground HONO source, $\gamma_{NO_2,max}$ was increased by a factor of 5 and $J_{HNO_3,surf}$ was set equal to $J_{HNO_3,g}$. This test clearly failed to produce a strong enough source to describe HONO concentrations at 3 m. It is evident therefore that surface HNO_3 photolysis is an essential contributor to the HONO source and that it needs to proceed at a faster rate than gas phase HNO_3 photolysis. It is also interesting that the photo-enhanced NO_2 source is lower here than in Sens2 at most times throughout the day. Increasing $\gamma_{NO_2,max}$ between the Base run and Sens2 caused an increase in the source due to greater NO_2 uptake and conversion but this is obviously a nonlinear trend as $\gamma_{NO_2,max}$ continues to increase. The NO_2 concentration in the lowest model layer in Sens4 is less than half the concentration in Sens2, indicating that the mechanism becomes transport limited. Although NO_2 is converted at a greater rate, this is depleting NO_2 near the surface that cannot be replenished quickly enough from aloft, leading to an overall decrease in HONO production.

Since both photolytic mechanisms have similar dependencies, including irradiance and NO_x concentrations, it can be difficult to determine which is more important for HONO production. These sensitivity tests show that the contributions from each mechanism are uncertain due to poorly constrained $\gamma_{NO_2,max}$ and $J_{HNO_3,surf}$. While it is possible for surface HNO_3 photolysis to explain most of the HONO source, NO_2 conversion alone cannot produce enough HONO at the CalNex site. Without additional laboratory studies that demonstrate the specific importance of each of these two mechanisms, it is clear that both can be considered important HONO sources in urban regions.

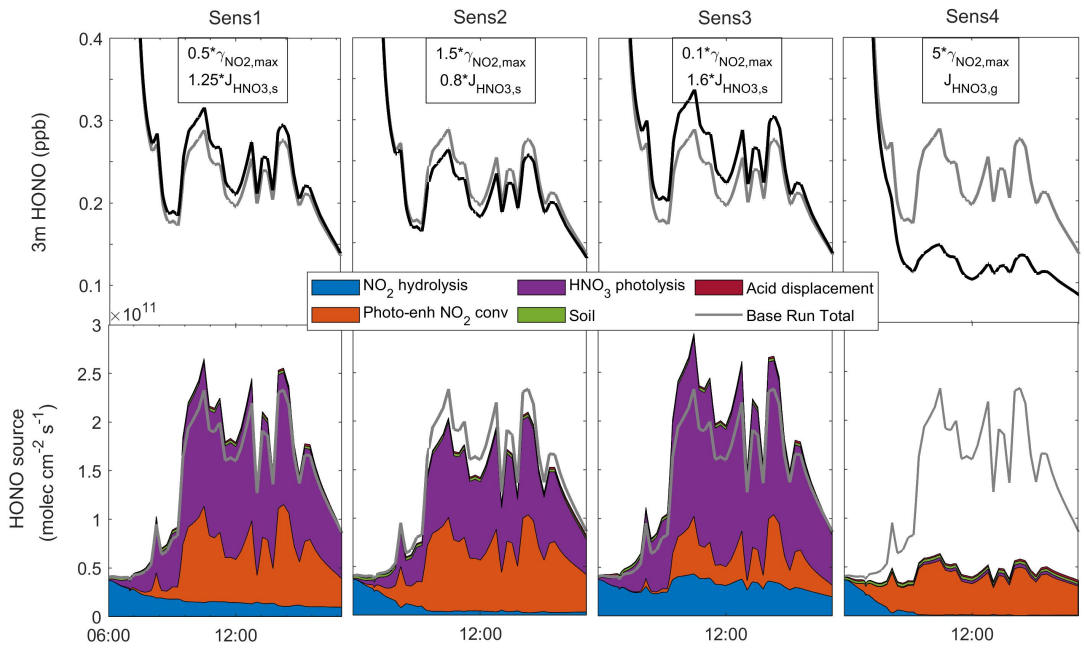

Figure 4.8: Results from sensitivity studies Sens1 - Sens4 for the afternoon of May 28. The top panel shows the 3 m HONO concentrations (black line) compared to the Base run (gray line). The bottom panel shows the contribution of the various formation mechanisms to the total HONO surface source. The total source from the Base run is indicated with by the gray line for comparison.

4.7 Conclusion

HONO's impact on secondary pollutant formation makes it an important species in urban environments. Since it's heterogeneous formation mechanisms are poorly understood, a new one-dimensional chemistry and transport model, PACT-1D, has been developed to perform mechanistic studies that can help constrain the HONO budget. In particular, PACT-1D has the ability to do molecular level surface chemistry and emissions. The model has been tested against observations from the CalNex field campaign, which was performed in the

urban region of Los Angeles. Multiple heterogeneous source mechanisms at the ground were added to the model which helped better simulate atmospheric HONO levels, both at the ground and throughout the boundary layer. The daytime HONO source was dominated by HNO_3/nitrate photolysis at the ground, followed by photo-enhanced conversion of NO_2. At night, the major HONO source was conversion of NO_2 on the ground. With these sources implemented the model shows that HONO photolysis is the dominant contributor to primary OH production near the surface. This contribution decreases quickly with altitude, showing a similar vertical profile to HONO concentration. These results emphasize the importance of atmospheric mixing when considering HONO's total impact to the boundary layer and help better understand the HONO sources in urban environments. Tests were also performed to determine the sensitivity of the two major daytime HONO sources to uncertainties in their mechanisms. While their relative contributions vary with the uncertainties, it is clear that both HNO_3/nitrate photolysis and photo-enhanced conversion of NO_2 should be considered to accurately simulate HONO in urban atmospheres.

CHAPTER 5

FIREX-AQ model results and discussion

Simulations of two fires sampled during the FIREX-AQ campaign were performed using PACT-1D. In this chapter, model results are compared to both in-situ and remote sensing observations to evaluate model performance. As discussed in Section 3.3, the model runs focus on chemistry in the horizontal middle of the plume, so only in-situ measurements from about 1500 m in the center of each transect are used for comparison. Vertical profiles and chemical budgets of HONO and HO_x are used to determine HONO's importance in biomass burning (BB) plumes. Because HONO is the dominant OH radical precursor in young smoke, this information is crucial to better constrain ozone and particle formation resulting from fire emissions. Sensitivity tests are also conducted to investigate how uncertainties in secondary production rates impact HONO concentrations, and how HONO emissions influence O_3 formation in smoke.

5.1 Evaluation of PACT-1D modifications for plume modeling

In order to more accurately simulate biomass burning plumes, PACT-1D was updated with a plume rise and dilution scheme. Since CO is a relatively non-reactive species that is emitted from fires in large quantities, its concentration is used to evaluate the plume location and the degree of dilution. Figure 5.1 shows the modeled CO plume compared to the 532 nm backscatter coefficient from the plume overpasses for each fire. The backscatter coefficient is from NASA's Differential Absorption Lidar/High-Spectral Resolution Lidar (DIAL/HSRL) instrument and provides useful information on the plume location, with higher values indi-

cating higher aerosol concentration. At some points along the plume overpass, the smoke was so thick that the laser was fully attenuated before penetrating the entire plume, which is shown as white areas in Figure 5.1.

Even with missing data, it is possible to see that both plumes were lofted 2-3 km above the ground, which matches the location in PACT-1D. The observations show considerable vertical variation with smoke age, however, that is not captured in the model. The injection altitude of smoke depends strongly on the temperature of the fire and the amount of heat released, with a hotter plume rising to a higher altitude. Temperature variations during burning will cause changes in the injection altitude, and this is clearly seen in the observed plumes in Figure 5.1. PACT-1D, on the other hand, follows a single air mass from the time of emission so is not impacted by variations in temperature or heat. There is also minimal vertical mixing in the free troposphere where the plume is lofted, indicated by low eddy diffusion coefficient (K_Z) values. This stabilizes the modeled plume at the same altitude as it ages.

Since PACT-1D does not include plume dynamics other than the initial rise, it is possible that the model underestimates the loss of species through vertical mixing at the top and bottom of the plume. Sensitivity tests were therefore performed, increasing K_Z in the free troposphere by a factor of 100. These results showed that loss through vertical mixing, even with much higher K_Z values, was minor compared to horizontal mixing. Additionally, the horizontal mixing parameter, K_y, is assigned using observations, so any dilution loss that is not captured in the vertical mixing scheme is likely compensated with horizontal mixing. The goal of the model runs is to better understand the chemistry within these plumes so the mixing parameterizations used in PACT-1D are sufficient for this purpose. More sophisticated methods would be necessary to study the plume dynamics and evaluate differences in vertical versus horizontal dilution.

Figure 5.2 shows the progression of CO concentrations in the model runs from 10-240 minutes. Due to the large concentration change over this time, the initial plume rise is not

shown and a new scale is assigned for each hour. The highest CO is found in young smoke, with plume center mixing ratios exceeding 10,000 ppb at a 10 minute smoke age. Values in WFF are higher since it was a larger and more intense fire, which emitted more carbon. This can be seen in the higher backscatter coefficient values in Figure 5.1 and the total carbon emissions in Figure 3.1. CO concentrations decrease with time due primarily to horizontal dilution, with 1000 ppb seen in the Shady Fire plume center at 240 minutes and 2000 ppb in WFF. In addition to a significant decrease with time, CO concentrations also vary with altitude, with the highest values in the plume center and a rapid decay moving to the top and bottom of the plume.

PACT-1D is compared to transect observations from NASA's Differential Absorption CO Measurement (DACOM) instrument, shown in the colored circles in Figure 5.2. Since the plume height varies between the model and observations (Figure 5.1), the CO measurements shown in Figure 5.2 are placed at approximate altitudes. The 532 nm backscatter coefficient data from each transect was used to define the top and bottom of the observed plume, using a value greater than 0.1 km^{-1} sr^{-1} to identify smoke. Both the Shady Fire and WFF plumes were approximately 1000 m high during early transects and decreased to 500-700 m over the course of sampling. The modeled plume height was determined using the same method described in Section 3.3, where model boxes with CO concentrations greater than 300 ppb are considered to be within the plume. The observed plume was then scaled to the modeled plume height, also scaling the measurement altitude to the approximate location in PACT-1D. Although there are inherent errors translating the plume height between the observations and model, this method provides a reasonable way to determine if PACT-1D is capturing the general concentration trends seen in the campaign. The placement of the measurements should be not be seen as completely accurate and there are many examples in Figure 5.2 where a shift up or down by 100 m shows much better agreement.

Another factor complicating the comparison between the model and observations is that sampling during the campaign was not performed in a strictly Lagrangian manner. Although

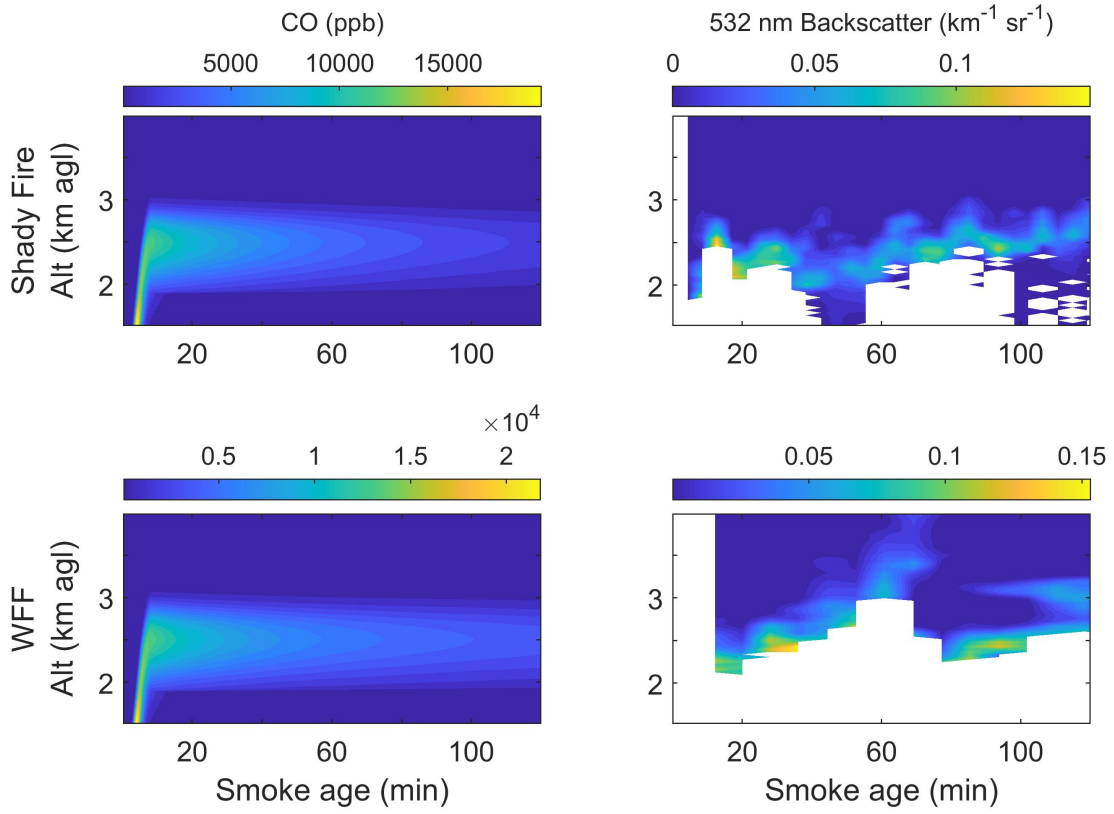

Figure 5.1: Modeled CO (left) is compared to the measured 532 nm backscatter coefficient (right) to evaluate PACT-1D's plume rise feature. The backscatter data is from the DIAL/HSRL instrument during the plume overpasses for both fires. White sections indicate when the instrument signal was saturated and the laser could not penetrate the entire depth of the plume. The modeled CO plume for both the Shady Fire (top) and WFF (bottom) is lofted to 2-3 km agl, approximately matching the altitude range of the observed plumes.

the DC-8 performed consecutive transects through the smoke as the plume traveled downwind, the same air mass was not followed during this process and each measurement therefore has a different emission time. As mentioned above, PACT-1D models a single air mass with one emission time. The varying emissions during sampling are somewhat accounted for in the model by averaging over a time range (described in Section 3.3), but large concentration changes due to emission variations cannot be captured in PACT-1D. Even within a 1 hour

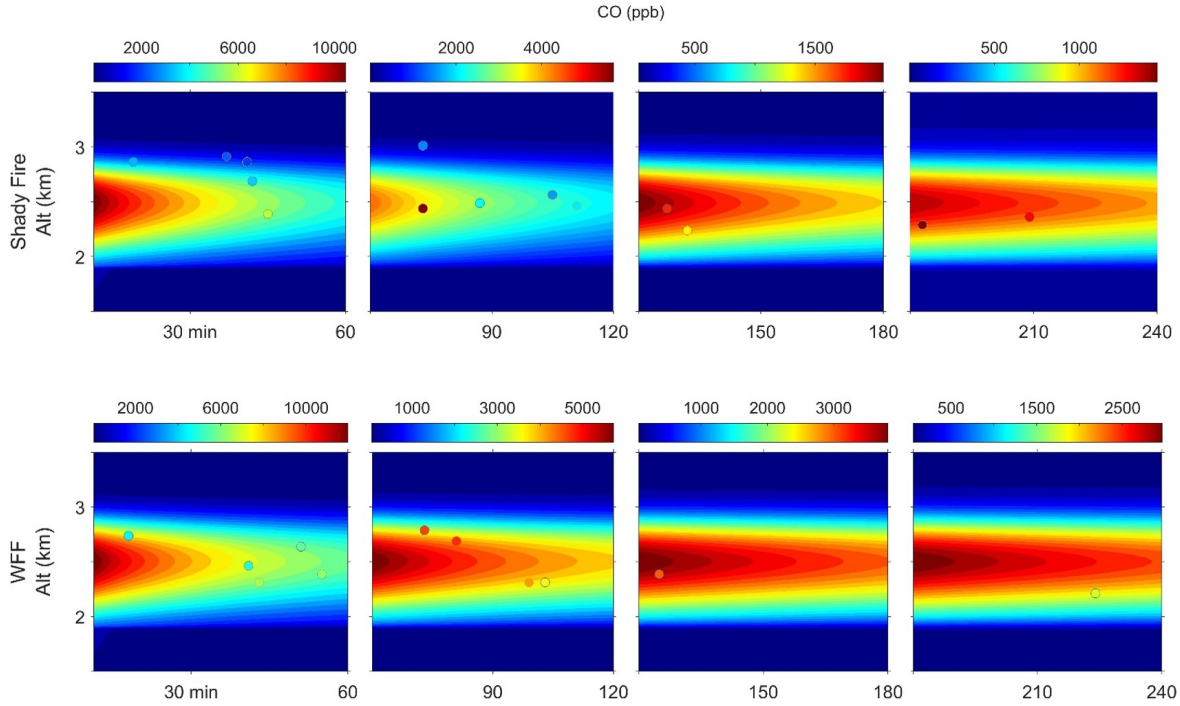

Figure 5.2: Modeled CO for smoke ages from 10 min through 4 hours. The Shady Fire is shown in the top panels and WFF is shown in the bottom panels. The circles show a comparison to transect observations from the DACOM instrument. A different scale is used for each hour due to the large change in concentrations as the plume travels downwind.

time period, emissions can change by nearly a factor of 2 (Figure 3.1). A clear example can be seen in the Shady Fire data at 75 and 90 minutes (Figure 5.2, top panel). The observed CO decreases 3000 ppb within 15 minutes, which is too large to be explained by dilution and instead indicates a change in emissions between the two air masses.

The goal of the PACT-1D runs is not to perfectly describe the measurements, but rather to capture the general trends and broad chemical characteristics of the plumes and focus on the mechanistic details related to HONO chemistry. Considering the fine vertical scale and the uncertainties in the measurement altitude and emissions, PACT-1D, overall, does a good job simulating the CO concentrations for both the Shady Fire and WFF plumes. This

provides confidence in the model's ability to reasonably describe plume rise, dilution, and carbon emissions.

5.2 Comparison of model results to in-situ measurements

Similar to the comparison with CO observations, results from the full plume model runs, with all fire emissions included, were compared to transect measurements (Figure 5.3 and Figure 5.4). HONO measurements are from NOAA's Time of Flight (ToF) Chemical Ionization Mass Spectrometer (CIMS) instrument, NO_2 and O_3 are from NOAA's chemiluminescence instrument, pNO_3 is from University of Colorado's ToF High Resolution Aerosol Mass Spectrometer (AMS) instrument, and HCHO is from University of Colorado's Compact Atmospheric Multi-species Spectrometer (CAMS) instrument. References for each instrument are listed in Table 2.2.

Modeled HONO, NO_2, pNO_3, and HCHO all show similar trends with time and altitude that generally follow CO. These species are emitted from the fire so have highest concentrations in young smoke in the plume center. Similar to CO, each shows a rapid decay moving towards the top and bottom of the plume. Dilution and mixing play a large role in the decrease with smoke age and altitude but chemistry also has a noticeable impact for these reactive species, as further discussed below. In both model runs, HONO concentrations are near 20 ppb at a 10 minute smoke age and decrease to 0.05 ppb in the Shady Fire and 1.5 ppb in WFF at 240 minutes. NO_2 decreases from 50 ppb to 0.5 ppb in the Shady Fire and from 70 ppb to 5 ppb in WFF. The higher values in WFF are due again to its thickness. The larger concentration of aerosols in the smoke leads to lower photolysis rates compared to the Shady Fire so less HONO and NO_2 are lost through photolysis in the older smoke. HCHO and pNO_3 show similar trends but are less impacted by photolytic loss. Additionally, HCHO is produced more efficiently in older smoke than HONO or NO_2. Because of this, both HCHO and pNO_3 show a wider vertical distribution than HONO and NO_2 and their

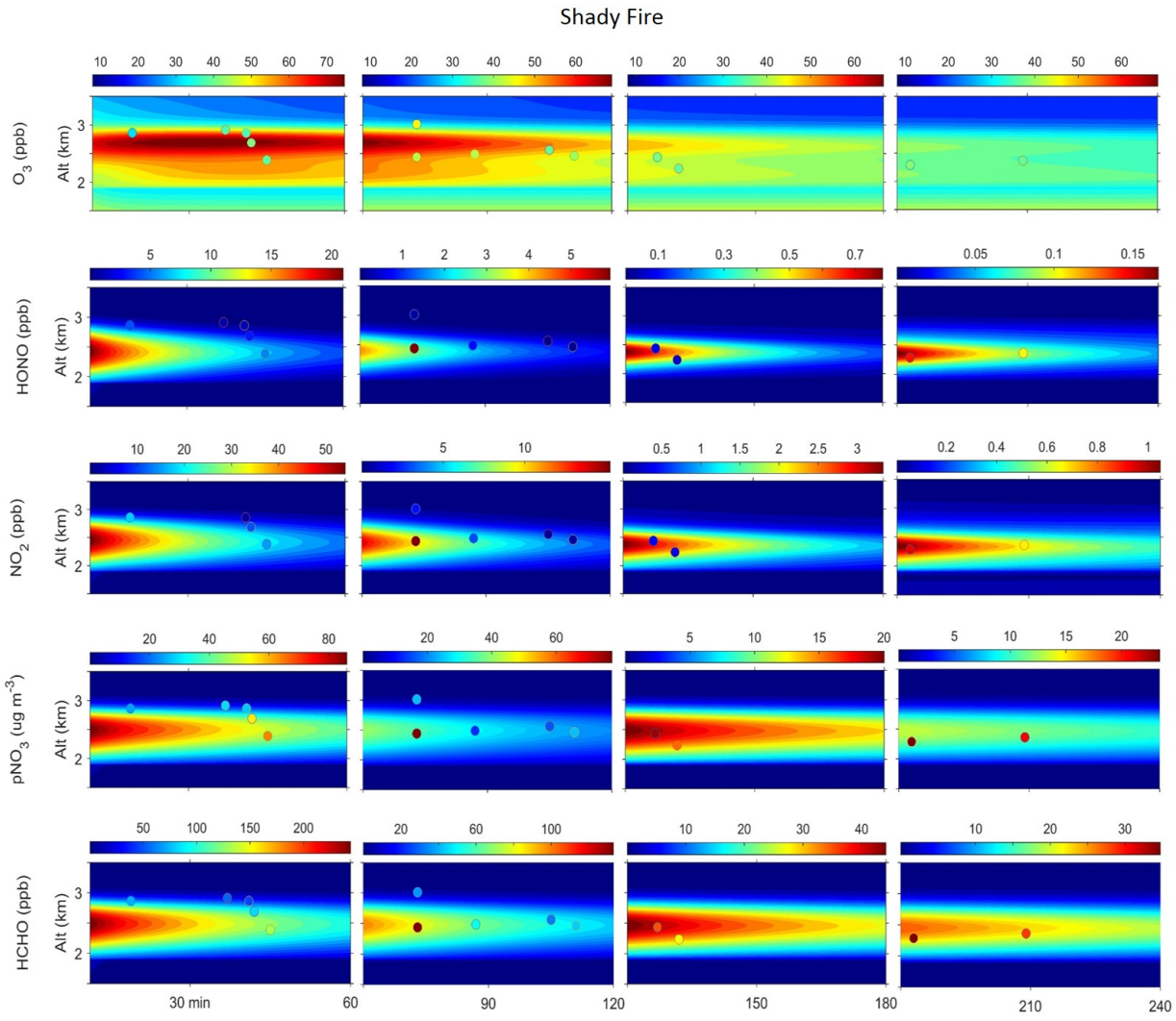

Figure 5.3: Modeled O_3, HONO, NO_2, pNO_3, and HCHO for the Shady Fire, showing smoke ages from 10 min through 4 hours. The circles show a comparison to transect observations (instruments listed in Table 2.2). A different scale is used for each hour due to the large change in concentrations as the plume travels downwind.

concentrations do not decay as quickly with age.

O_3 profiles show a different trend than the other species. O_3 is not emitted from fires and instead is a secondary pollutant that can form in smoke from the high levels of emitted NO_x and VOCs. In both plumes, PACT-1D shows elevated levels at the plume top, indicating

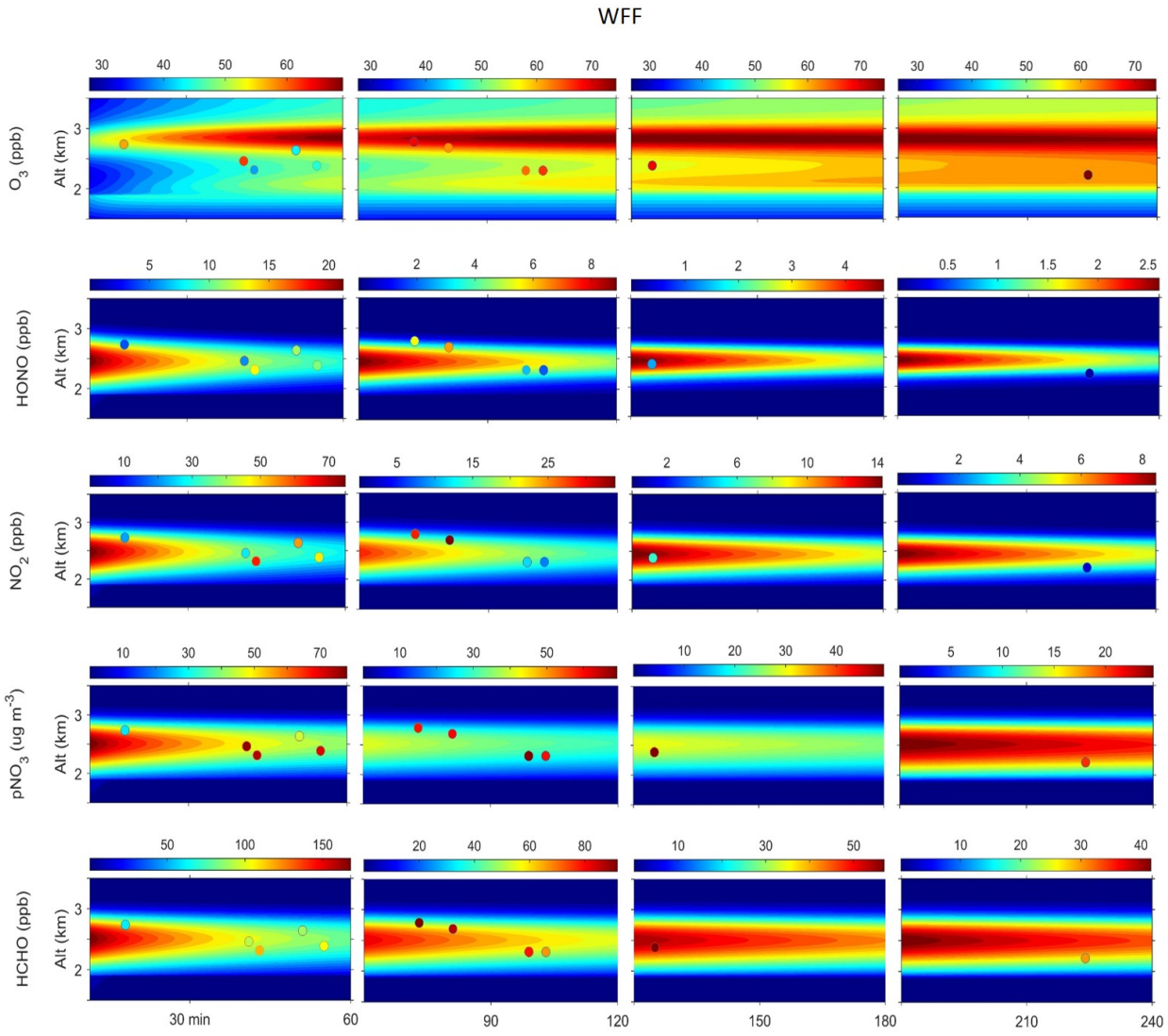

Figure 5.4: Same as Figure 5.3, but for the WFF model run.

O_3 formation from the increased photolysis rates and photochemistry. Concentrations in the Shady Fire reach 72 ppb within the first hour. The band of elevated O_3 extends through 150 minutes but decreases to 45 ppb and the altitude gradient within the plume gets less steep with age. By 240 minutes there are slightly higher values towards the plume bottom. This shift in the O_3 profile is attributed to the vertical profiles of photolysis rates and NO_x and VOC concentrations that change via dilution and chemistry. WFF also shows elevated

O_3 levels at the plume top, but the formation occurs more slowly. A peak of 72 ppb is not reached until 90 minutes downwind and is then maintained through 240 minutes. At lower altitudes in the WFF plume, O_3 levels are smaller than in the Shady Fire, with a minimum of 30 ppb at 10 minutes. These concentrations steadily increase with smoke age, indicating O_3 formation, and reach 60 ppb by 240 minutes. Overall, the O_3 production in WFF is slower than in the Shady Fire and these high levels are maintained for a longer period.

The measurement comparisons here have the same limitations discussed in the previous section, including difficulty in mapping observations to the correct model altitude and addressing varying emissions. There are again many examples in Figures 5.3 and 5.4 where a 100 m shift in altitude would show better agreement. For the Shady Fire, PACT-1D concentrations, with the exception of O_3, match the observations well in the first hour. As with the CO data, the measurements at 75 and 90 minutes again show a large concentration decrease that is due to changing emissions and therefore not captured in the model. PACT-1D overestimates HONO and NO_2 around 130-140 minutes but matches the observations well after 180 minutes. There's good agreement for pNO_3 and HCHO concentrations, with a slight overestimation in the model after 180 minutes.

Within the first hour, O_3 concentrations are nearly 30 ppb higher than observations. Although some of the measurements collected higher in the plume may be influenced by inaccurate altitude placement, the model clearly overestimates O_3 in the plume center. NO concentrations in young smoke are underestimated by about 50%, so the strong titration of O_3 by emitted NO is not accurately captured. Low NO values are likely due to model emissions, which are based on field observations from the first transect. For the Shady Fire, this was 20 minutes downwind of the fire and considerable NO may have been lost by this point due to the fast chemistry with background O_3. Total NO_x emissions are somewhat compensated by including NO_2, but the small photolysis rates in the smoke prevent NO_2 from photolyzing to NO, so the O_3 titration is still underestimated. The influence of the initially emitted NO fades as the smoke ages and PACT-1D does a better job matching the

O_3 observations in the later portion of the model run.

PACT-1D has a more difficult time capturing the observed concentrations for WFF. The thicker and denser plume is more difficult to model considering the parameterizations used in PACT-1D for aerosol surface area and photolysis rates. HONO concentrations are captured fairly well, but the model is significantly higher than the observations at 40 and 130 minutes. The large concentration change between the two points near 40 minutes again indicate an emission change that cannot be simulated with PACT-1D. NO_2 is underestimated from 45-80 minutes and overestimated at 130 minutes. Based on the time series of carbon emissions shown in Figure 3.1, it seems the overestimation after 130 minutes is likely due to emission changes. The measurements at 130 and 220 minutes correspond to emission times of 23:45 and 22:15 UTC. The total C emissions are lower at these times than the average used in PACT-1D, so this impacts the model comparison. For most of the model run, pNO_3 is underestimated but there is good agreement between the modeled and observed HCHO concentrations, with a slight underestimation in the model from 70-100 minutes. Model O_3 tends to be underestimated in the plume center, particularly after 90 minutes. NO follows a similar trend as NO_2, with values underestimated in the early plume which will again impact O_3 titration. The high NO_x after 120 minutes appears to be destroying too much O_3, giving modeled values that are 10-20 ppb higher than measurements.

Normalized enhanced mixing ratios (NEMR, Equation 1.17) of HONO, NO_2, and O_3 are shown in Figures 5.5 and 5.6. NEMRs describe the concentration change of a species between the plume and background air normalized to CO ($\Delta X/\Delta CO$). This removes the influence of dilution so any NEMR changes with time can be attributed to chemistry. Increasing values with time indicate that overall formation is greater than loss and decreasing values mean the opposite. Negative values show that the plume concentrations are lower than background. The average concentration measured during the upwind transect is used as the background here.

In general, the HONO and NO_2 NEMRs for both plumes decrease with smoke age and

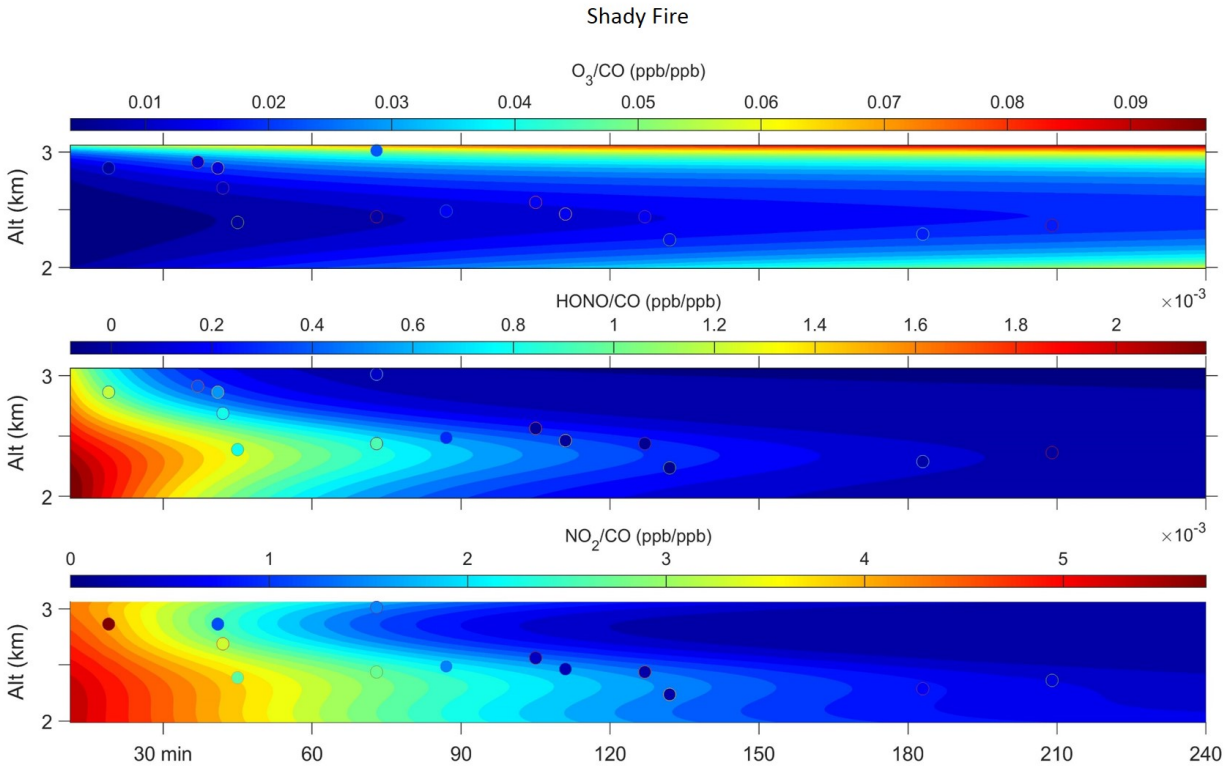

Figure 5.5: O_3, HONO, and NO_2 NEMRs for smoke ages 10-240 minutes for the Shady Fire. The circles show a comparison to transect observations. Background concentrations used in the NEMR calculation are from the upwind transect.

at higher altitudes, indicating that both are chemically lost in the upper portion of the plume as smoke travels downwind. The decrease with time seems to occur more quickly in the observations which may suggest the photolysis rates in PACT-1D do not increase fast enough. O_3 NEMRs are highest at the plume top and increase with time due to increased formation. The observed values for WFF decrease slightly between 30-60 minutes showing that O_3 is lost at this point, which is not captured in the model. The comparisons here again suffer from observation placement but as a whole, PACT-1D reasonably captures the general chemical trends.

Overall, PACT-1D does a good job simulating the change in concentrations of key chem-

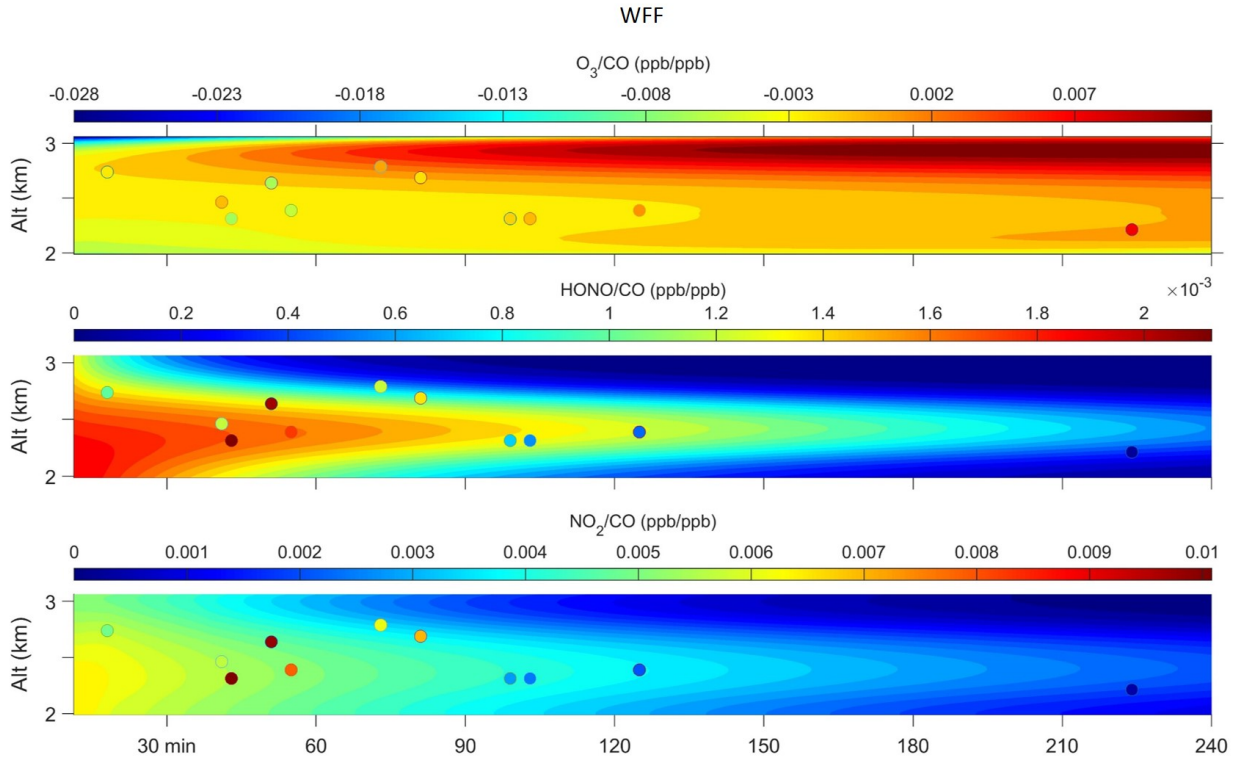

Figure 5.6: Same as Figure 5.5, but for the WFF model run.

ical species within smoke and an analysis of results can provide useful information about the HONO chemical budget.

5.3 Comparison of model results to mini-DOAS measurements

To remove the uncertainty related to the measurement altitude in the above section, model results were also compared to mini-DOAS data (Figure 5.7). Absorption spectra measured by the mini-DOAS instrument during the plume overpass segments of FIREX-AQ were analyzed with the radiative transfer model, VLIDORT-QS (Brockway, 2021). This analysis provided vertical column densities (VCDs) for HONO and NO_2, with a reported error of 16.5%. PACT-1D total column concentrations within the plume were calculated by summing the concentrations for each model box that was within the plume altitude range.

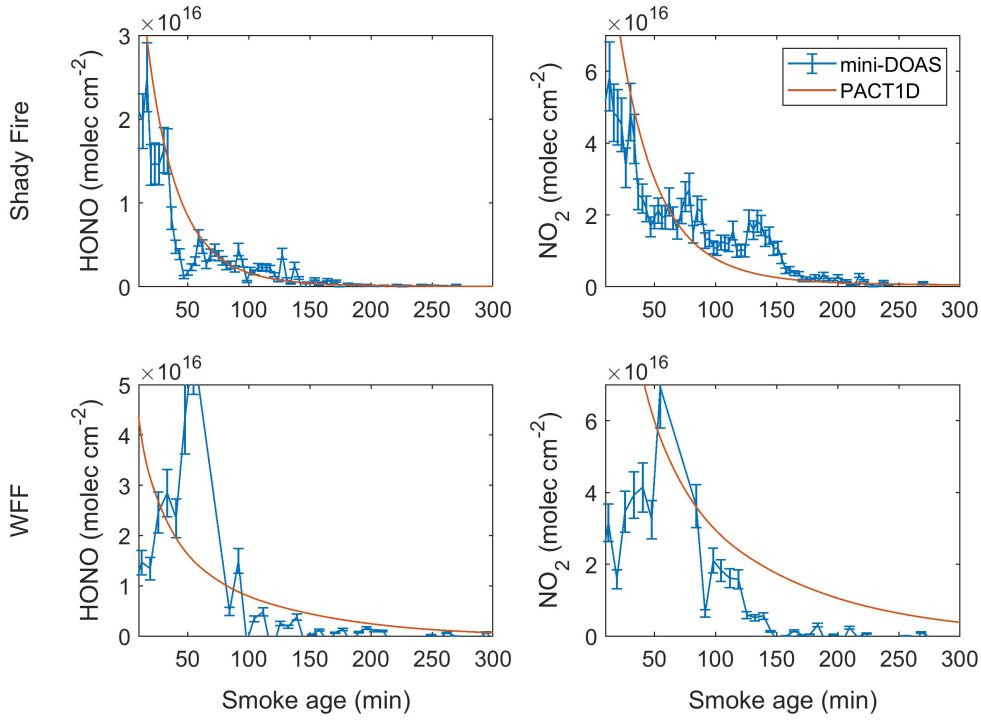

Figure 5.7: Comparison of column values of HONO (left) and NO_2 (right) between PACT-1D (orange) and the mini-DOAS (blue). The Shady Fire is shown in the top panel and WFF is shown on the bottom. PACT-1D values are the summed concentration within the modeled plume. mini-DOAS vertical column densities (VCDs) were determined through analysis of observations with a radiative transfer model and have an error of 16.5%.

PACT-1D does a particularly good job capturing the observations for the Shady Fire (Figure 5.7, top panel), showing a rapid decay in both HONO and NO_2. The decrease in HONO occurs more quickly due to its faster photolysis which is also simulated well. This provides further confidence in the model's ability to simulate these plumes. The VCDs for WFF show a greater variability with smoke age, with a large peak in both species around 60 minutes. Similar to the in-situ observations, the mini-DOAS measurements are not following a single air mass as it ages and is again subject to changing fire activity and emissions. Sensitivity tests were performed, increasing and decreasing the fire emissions for the WFF run by 30% to determine if the large shifts in VCD values could be attributed to emission

variations.

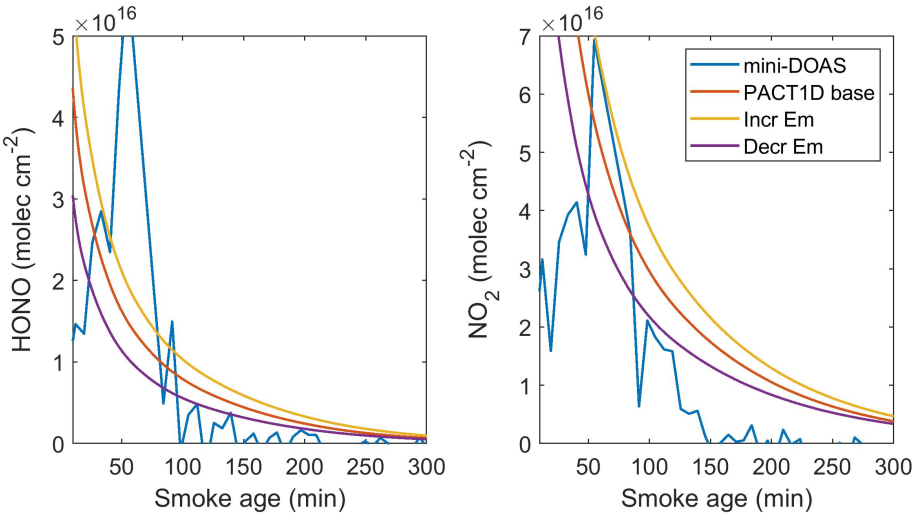

Figure 5.8: Comparison of column values of HONO (left) and NO_2 (right) between PACT-1D and the mini-DOAS (blue) for WFF. mini-DOAS VCDs have an error of 16.5% (error bars removed for clarity, see Figure 5.8) The PACT-1D base run is shown in orange. The yellow line shows a model run with fire emissions increased by 30% and the purple line shows a run with emissions decreased by 30%.

The impact of emissions can be seen clearly in the NO_2 data (Figure 5.8, right panel), with the increased emission run clearly matching the high VCD values from 60-90 minutes, and the decreased emission run following values at 50 and 100-120 minutes. The increased emissions also show better agreement with some of the higher HONO data around 50 and 90 minutes but does not capture the very large peak at 60 minutes. All of the model runs overestimate NO_2 after 120 minutes. PACT-1D values are higher than both HONO and NO_2 in-situ values in this time frame as well. As discussed above, the measurements after 130 minutes are associated with lower emissions and the sensitivity tests here show emissions would need to be decreased by more than 30%. This is possible considering the large changes in carbon emissions seen in Figure 3.1. The overestimation of HONO and NO_2 NEMRS at this time however also indicates that either the formation is too great or the destruction is

too small. It is very likely that photolysis rates do not increase fast enough in PACT-1D, underestimating the photolytic loss.

Dilution may be another cause for the disagreement. Although the WFF CO observations are captured well after 120 minutes, there are only two data points in this time frame, which decreases confidence in the comparison. Underestimated dilution rates would lead to overestimated NO_2. Similarly, the increase in photolysis rates over time is determined from observations. The lack of measurements in older smoke may also lead to an underestimation of these rates, which would have a significant impact on HONO and NO_2 due to their fast photolysis. While an analysis of WFF results will be presented in later sections, this uncertainty should be kept in mind. Greater emphasis is placed on the Shady Fire model run since it seems to more accurately simulate the observed plume.

5.4 HONO vertical profiles

The vertical profile information provided by PACT-1D can help interpret field observations which are collected at a single altitude or as column densities. This is particularly useful for fast-reacting species like HONO. The fact that photolysis rates can change an order of magnitude within a plume (Figure 3.4) makes it especially important to understand how HONO levels, and its production of OH, change vertically within smoke. Other studies have focused on horizontal HONO variations within a plume (Peng et al., 2020; Wang et al., 2021), but vertical variability has received much less attention.

Similar to other emitted species, HONO values are greatest in young smoke and decrease with smoke age due to both chemistry and dilution (Figure 5.9, top panel). The largest concentrations are also seen near the plume center where photolysis rates are low and there is less dilution with background air. There is a very steep decline moving away from the maximum towards the plume top and bottom. This provides another visualization of the measurement location sensitivity that was discussed above. For example, at 30 minutes in

the Shady Fire, the HONO concentration decreases from 5.2 ppb to 2.5 ppb, when moving from 2.7 to 2.8 km. The fact that HONO is nearly cut in half within just 100 m clearly emphasizes the vulnerability in the comparisons presented in Section 5.2. Again, comparison with column values from the mini-DOAS removes some of this uncertainty and shows a much clearer agreement.

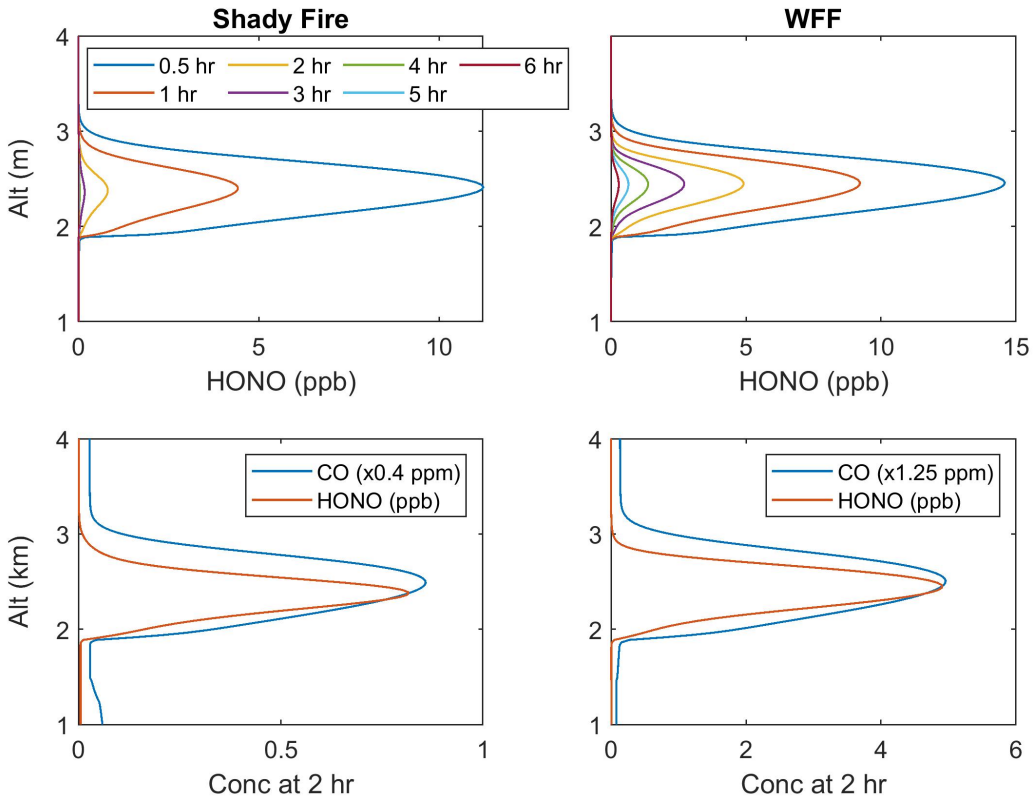

Figure 5.9: Vertical profiles of HONO within the Shady Fire (left) and WFF (right) plumes. The profiles at various smoke ages from 30 min to 6 hours are shown in the top panel, with HONO decreasing over time. The bottom panels compare HONO and CO at a 2 hour smoke age. CO concentrations have been scaled to show how the vertical profile between the two species differ.

Although the HONO vertical profile shows a Gaussian shape, it does not match the profile of less reactive species. This can be seen clearly when compared to CO (Figure

5.9, bottom panel), which shows a wider profile. HONO decays more quickly at the plume top and bottom where photolysis rates are greater. In field campaigns, aerosol information from LIDAR instruments are typically used to determine plume shape and height, giving a Gaussian profile similar to CO. When attempting to quantify total HONO concentrations within a plume from single-altitude observations, however, a more narrow profile needs to be used or total HONO levels will be considerably overestimated.

5.5 Primary HO_x production

The large emissions of HONO from burning fuel, and its efficient photolysis in low light conditions, make it one of the dominant sources of HO_x in biomass burning plumes, especially in young smoke (Peng et al., 2020; Theys et al., 2020; Robinson et al., 2021; Wang et al., 2021). A primary HO_x production (P_{HOx}) budget is constructed for both the Shady Fire and WFF model runs to evaluate the importance of HONO in these two plumes. Four P_{HOx} pathways are compared here (Figure 5.10): HONO photolysis, HCHO photolysis, O_3 photolysis followed by reaction of O^1D and H_2O, and acetaldehyde (CH_3CHO) photolysis. The entire vertical extent of the plume is considered in this analysis, summing P_{HOx} for all model levels within the plume to give a column P_{HOx}.

HONO photolysis dominates P_{HOx} in the early plume stages, contributing close to 80% of the the total immediately after emission. This steadily declines and HCHO becomes increasingly important. The rate of this decline varies between the two plumes with a much quicker decay in the Shady Fire and a slower, almost linear decay in WFF. The slower decline in WFF is likely because it is a thicker plume with higher aerosol concentrations. This decreases photolysis rates in the plume, allowing HONO to be transported farther from the burning location and providing a downwind source of HO_x. Additionally, HCHO is formed in plumes through photochemistry so the smaller photolysis rates slows this process and decreases its impact on P_{HOx} as well. HONO levels in PACT-1D are overestimated after

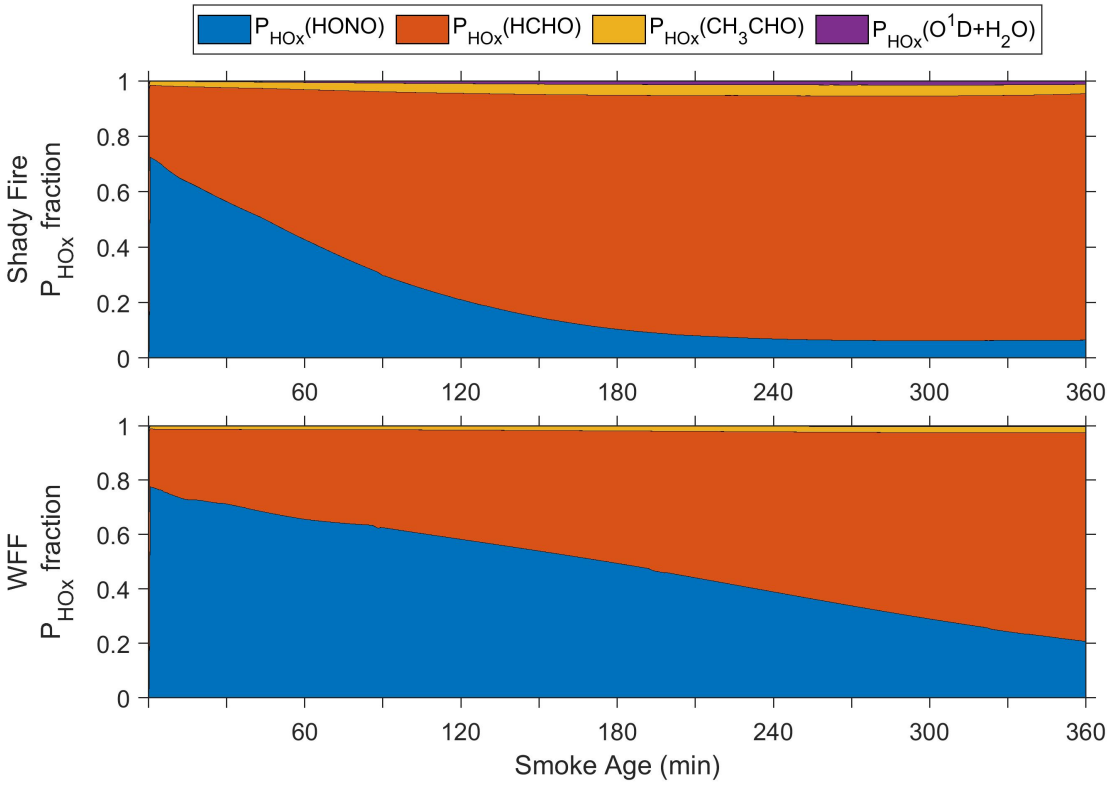

Figure 5.10: Comparison of primary HO_x production in the Shady Fire (top) and WFF (bottom) model runs, showing the contribution of four sources to total column P_{HOx}. HONO photolysis (blue) dominates P_{HOx} in the youngest smoke and HCHO photolysis (orange) becomes increasingly important as the plume ages. Together, acetaldehyde (yellow) and ozone (purple) never contribute more than 5%.

120 minutes in WFF, however, so its P_{HOx} contribution after this time is likely too high. In both plumes, HCHO is the dominant source of HO_x at the end of the 6 hour model runs, making up over 90% of the total for the Shady Fire and about 80% in WFF. HO_x from O_3 and CH_3CHO is considerably lower than HONO and HCHO, and together never contribution more than 5% to the total.

The HONO contribution to P_{HOx} in the early plumes compares well with values reported by Theys et al. (2020), who studied global HONO emissions from biomass burning using a

year's worth of satellite data. They found that HONO photolysis accounted for 80-90% of local OH production. These values are slightly lower than an analysis from the WE-CAN campaign, however. WE-CAN was conducted during the summer of 2018 in a similar manner to FIREX-AQ, where wildfire smoke plumes in the Western United States were sampled via aircraft. Peng et al. (2020) compared the same four HO_x sources and found that, as a campaign average, HONO made up over 90% of the P_{HOx} in the first hour of smoke age, slightly higher than this analysis. The contribution decreases to about 50% from 2-3 hours and then to 25% at smoke ages greater than 3 hours. These values at later smoke ages agree with WFF but not the Shady Fire. 2019 was a relatively mild fire season compared to 2018 (https://www.nifc.gov/fire-information/statistics) so the fires sampled during WE-CAN were likely larger with thicker smoke plumes than those from FIREX-AQ. WFF was one of the densest plumes sampled during FIREX-AQ so this may explain why there is better agreement with the values reported by Peng et al. (2020).

Vertical profiles of P_{HOx} were also analyzed and may explain some of the difference in this analysis versus WE-CAN. In most field studies, P_{HOx} is calculated from observations collected at a single altitude. As discussed in the previous section, HONO vertical profiles vary significantly within a plume and do not follow the same shape as aerosols or less reactive species. The profiles of P_{HOx} from HONO and HCHO show very different trends, and examples from 30 and 120 minute smoke ages are shown for the Shady Fire in Figure 5.11. At 30 minutes, the contribution of P_{HOx} from HONO is relatively constant through the core of the plume. HCHO on the other hand produces much more HO_x at the top than the bottom. The location of the measurement therefore plays a major role in balance of HO_x sources. An observation at the top of the plume would indicate a fairly even contribution of HONO and HCHO whereas at the bottom, HONO's influence would be overestimated in total plume-wide P_{HOx}. These profiles continue to change as the smoke ages. At 120 minutes, HCHO continues to be most important at the plume top, whereas HONO now has a peak in the plume center. These figures show how important it is to consider vertical variability

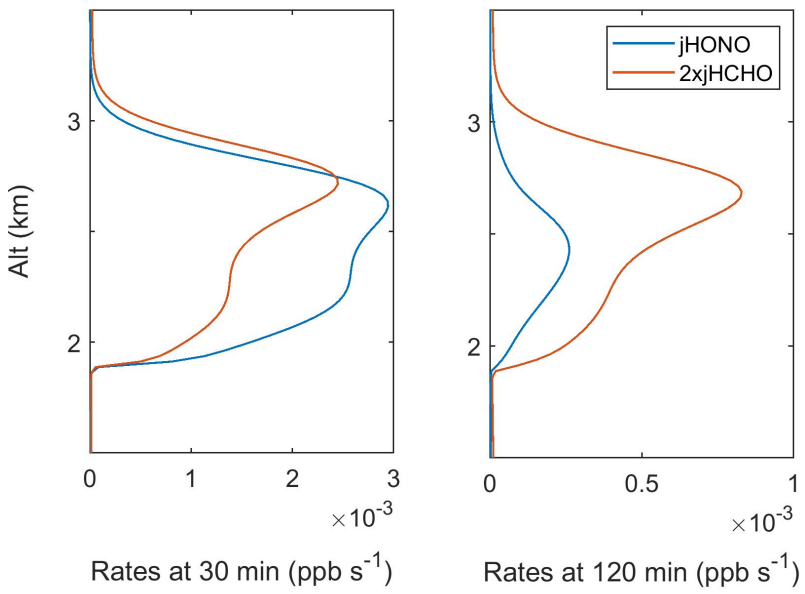

Figure 5.11: Vertical profiles of HO_x production from HONO (blue) and HCHO (orange) for the Shady Fire. Rates at a 30 min smoke age are on the left and 120 min on the right. Location within the plume plays a significant role in which of the two dominates P_{HOx}.

when determining the overall impact of various species on P_{HOx}.

5.6 HONO budget

One of the main goals of this thesis is to better understand the relative importance of HONO emissions versus secondary production within smoke plumes. A HONO budget was therefore constructed for both the Shady Fire (Figure 5.12) and WFF (Figure 5.13), considering gas phase reactions, uptake of HONO onto aerosol surfaces, heterogeneous aerosol formation (pNO_3 photolysis and NO_2 hydrolysis and photolytic conversion), vertical transport (VT), and lateral transport (LT). Negative rates in the figures indicate that HONO is being lost and positive means HONO is formed. A different scale is used for each smoke age. In both plumes, the main loss processes are photolysis and dilution through lateral mixing. HONO

formation is minor until later smoke ages when pNO_3 photolysis becomes important.

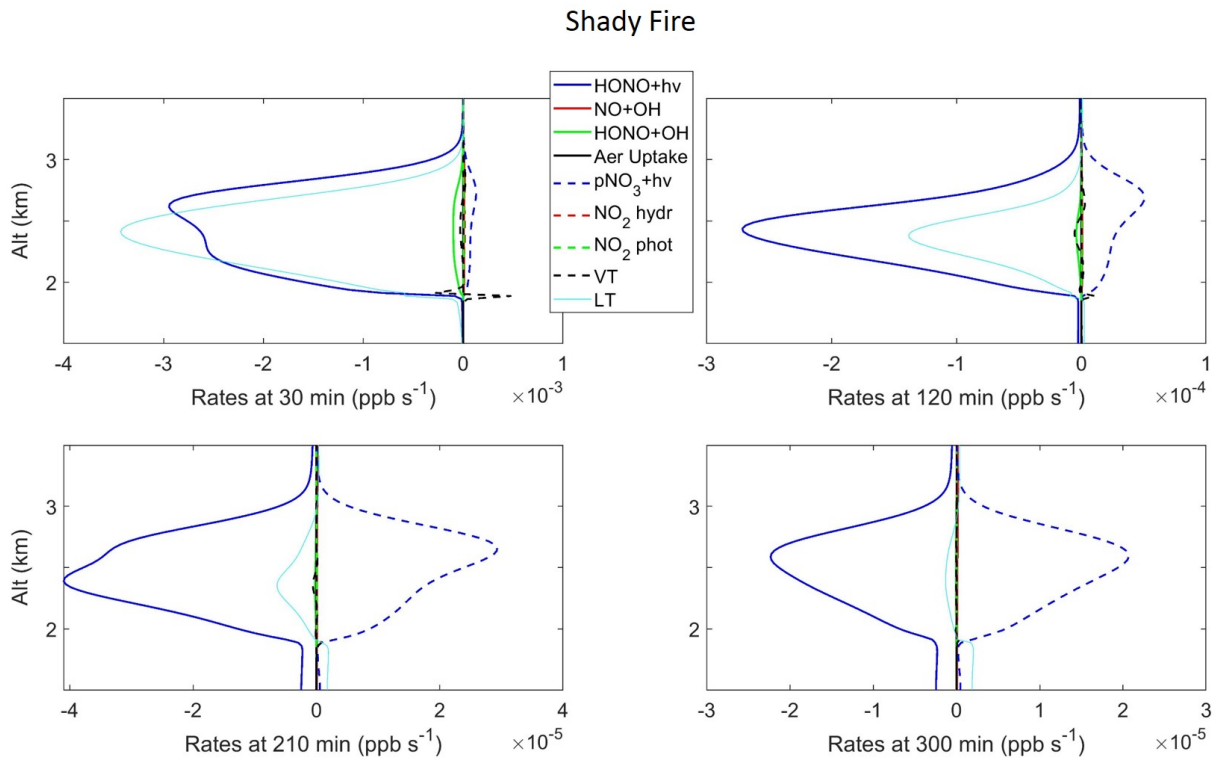

Figure 5.12: HONO budget plots for the Shady Fire at different smoke ages. Each line represents a different HONO source (positive values) or sink (negative), including gas phase reactions, uptake on aerosols, heterogeneous aerosol formation, and vertical and lateral transport. Each subplot has a different scale, with rates decreasing with smoke age.

At a 30 minute smoke age, lateral dilution with background air is the dominant HONO loss. The lateral transport (LT) rate is directly proportional to the HONO concentration in the plume, the background concentration, and the horizontal turbulent diffusion coefficient (K_y). The background concentration and K_y are constant with height at these altitudes, so the LT loss vertical profile follows the HONO concentration shape (Figure 5.9), peaking in the center of the plume around 2.5 km and decreasing at the top and bottom. As the plume ages, both the plume concentration and K_y decrease so the LT loss consequently gets smaller as well.

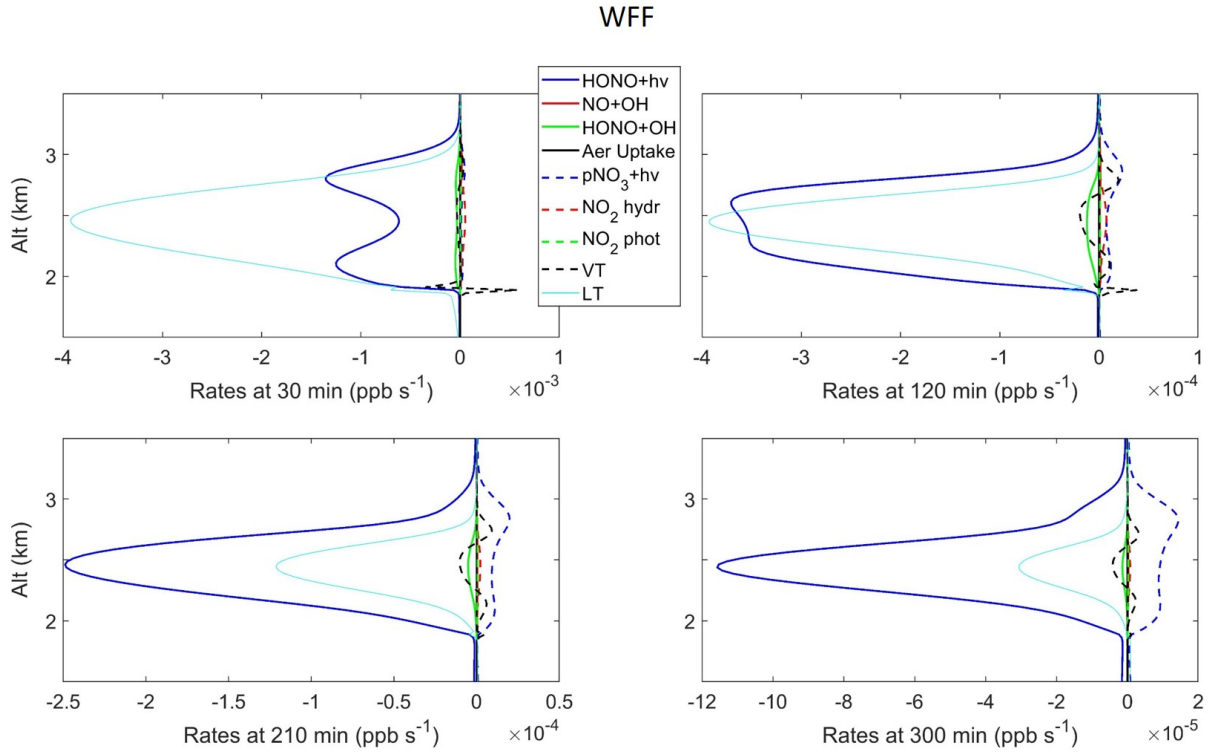

Figure 5.13: Same as Figure 5.12, but for the WFF model run.

Photolysis is the major chemical loss of HONO in both plumes and becomes more important than dilution as the plume ages. This loss depends on both the HONO concentration and the photolysis rate so the profile is more varied than the LT profile. Although HONO concentrations are greatest in the plume center, this is also where photolysis rates are lowest. The result of these opposing trends is seen most clearly in the 30 minute plot for WFF, where the more efficient photolysis at the plume top and bottom create a bimodal profile. This strong shape is not present in the Shady Fire since it was a thinner plume with higher photolysis rates. Greater photolytic loss was therefore seen throughout the plume at 30 minutes. By 120 minutes, the photolysis rates have increased, causing the WFF photolytic loss to lose the strong bimodal shape. As discussed in the previous section, the vertical profile of photolytic loss significantly impacts HO_x production.

In both plumes, the overall loss of HONO is greater than its formation. For WFF, this is

seen at all smoke ages and for the Shady Fire, this is true until about 300 minutes (5 hours). This imbalance in the budget indicates that most of the HONO lost is being transported from upwind (i.e., the previous model time step). The initial HONO emissions from the fire are providing this downwind HONO source. Even though the typical HONO lifetime is only 15-20 minutes under clear sky conditions, the extremely low photolysis rates within the smoke increase this significantly. At 30 minutes downind, the lifetime in the plume center (2.5 km) is 66 minutes for the Shady Fire and 389 minutes for WFF. Even at a 300 minute smoke age, the lifetime in WFF is still much higher than in background air, at 92 minutes. This allows the large amount of HONO emitted from the fire to be transported a great distance, providing a continual source of OH along the way.

The influence of the emissions on the HONO budget is seen until at least 210 minutes for both plumes. In the thick WFF plume, this extends for the entire 6 hour model run, due to a mix of the higher HONO emissions and lower photolysis rates compared to the Shady Fire. For the Shady Fire, the loss and formation of HONO is essentially equal by 300 minutes, meaning all of the initially emitted HONO has been lost and there is a near steady state between secondary HONO formation and photolytic loss. Comparing the two plumes, it is evident that the amount of HONO emitted, thickness of the smoke, and the plume center photolysis rates, all play an important role in how far downwind HONO emissions are transported. This has significant implications for the HO_x budget and ability of secondary pollutants to be formed at far distances from the original fire.

Secondary formation of HONO from pNO_3 photolysis becomes increasingly important in both plumes at later smoke ages. Starting at 120 minutes, this HONO source starts to play a role in the very top of the plume where it nearly balances the photolytic loss. This suggests that the HONO emissions are primarily transported in the center and lower portion of the plume and that HONO at the plume top is in a steady state. The small vertical transport rates in the plume also stabilize these emissions in the plume center. Continuing downwind, pNO_3 photolysis contributes more to the total budget, and for the Shady Fire, a balance is

eventually reached at 300 minutes.

Recent studies from the FIREX-AQ campaign suggest that secondary HONO formation plays a larger role than seen here. Wang et al. (2021), for example found that including heterogeneous conversion of NO_2 to HONO when modeling the WFF plume was necessary to accurately represent observed HONO concentrations. They report, however, that the HONO photolysis rates in their model are 20% higher than observations, causing a much larger photolytic loss than in this study. It seems that the overestimated loss of HONO by photolysis leads to the increased need for secondary production. PACT-1D more accurately represents the photolysis rates, allowing the initially emitted HONO to be transported farther downwind, eliminating the need for a strong heterogeneous source early in the plume.

Chai et al. (2021) and Kaspari et al. (2021) also suggest that heterogeneous NO_2 conversion is an important source of HONO in plumes sampled during FIREX-AQ. These studies use ground-based measurements collected from a mobile laboratory (MACH-2), however, and therefore analyze plume chemistry in smoke that penetrates the boundary layer and has contact with the ground. The PACT-1D model runs here focus on lofted plumes that are not influenced by heterogeneous chemistry at the ground. It's very likely that the large NO_2 concentrations and the greater available surface area of the ground (versus aerosol only) would make this an important secondary source of HONO. As seen in the CalNex study in Chapter 4, heterogeneous sources at the ground played a dominant role in the HONO budget and with even higher NO_x concentrations present in smoke plumes, these ground sources are expected to be even larger. Additional PACT-1D studies would be required to evaluate this possibility.

5.7 HONO source sensitivity studies

Similar to uncertainties in the HONO ground sources discussed in Section 4.6, the aerosol sources of HONO are also not well constrained. Sensitivity studies were again performed to

evaluate the impact of these unknown rates on the conclusions presented above. Four tests were performed, using the Shady Fire as the base run. To investigate the uncertainty in NO_2 conversion, the uptake coefficient (γ_{NO2}) for both the hydrolysis and photo-enhanced mechanisms were increased and decreased by 50% (Figure 5.14). Two more runs were performed, increasing and decreasing the pNO_3 photolysis rate by 50%, to address uncertainties in this parameter (Figure 5.15).

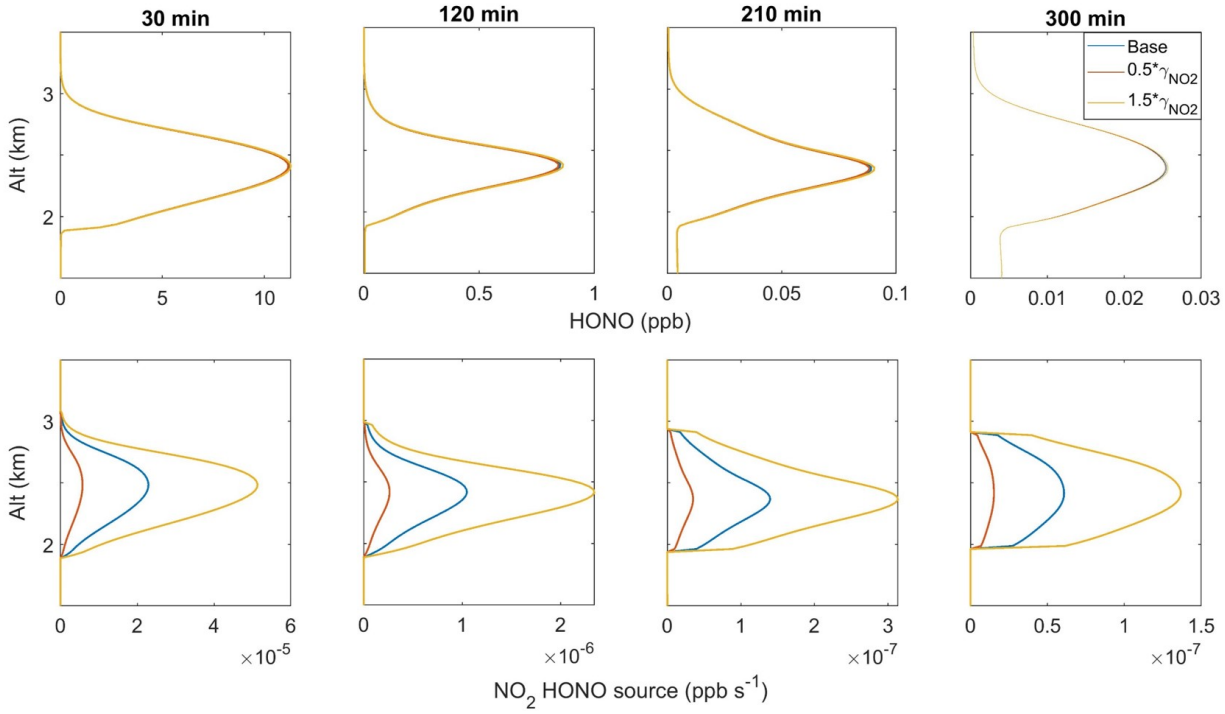

Figure 5.14: Comparison of Shady Fire HONO concentrations (top panels) from the base run (blue) and the sensitivity tests that decreased (red) and increased (yellow) the NO_2 uptake coefficient (γ_{NO2}) by 50%. The combined rate of HONO formation from NO_2 hydrolysis and the photo-enhanced conversion mechanism is shown in the bottom panels.

Changing γ_{NO2} had essentially no impact on HONO concentrations within the Shady Fire plume. Although the combined NO_2 hydrolysis and photo-enhanced conversion rates change by a factor of 2-4, they are still orders of magnitude smaller than the other HONO sources and sinks so the change is negligible. The γ_{NO2} value of 1x10 $^{-3}$ used in the base run

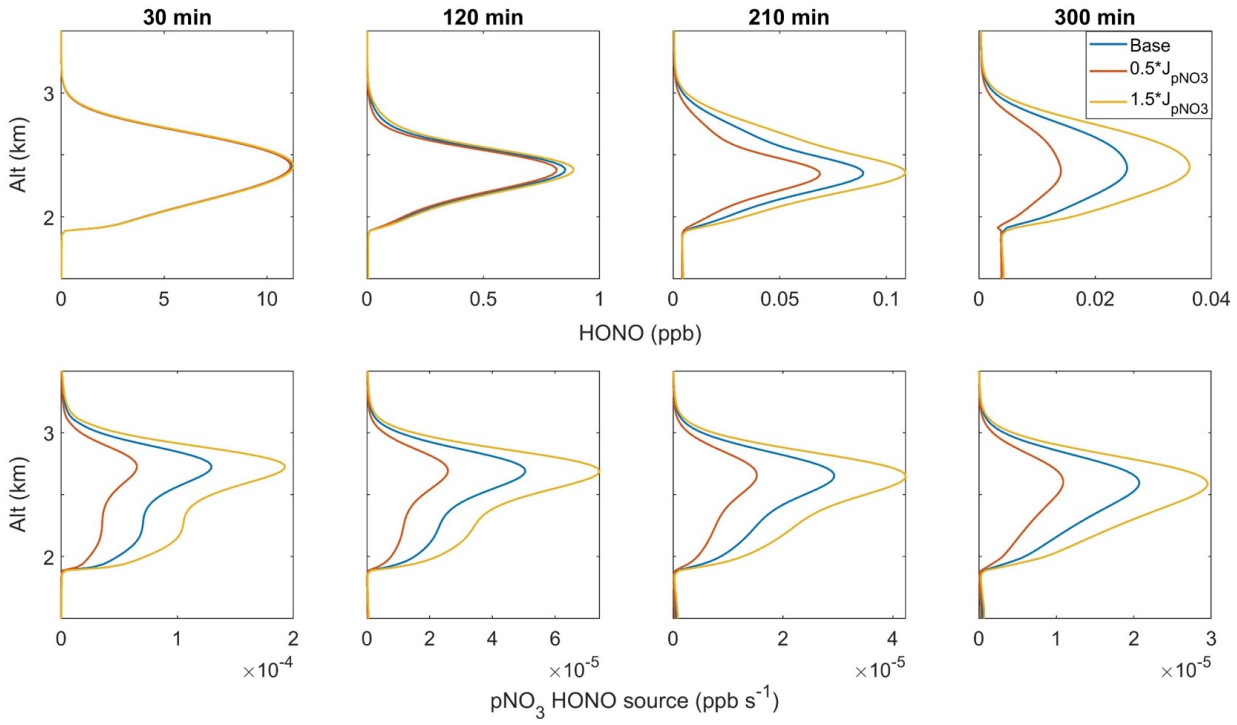

Figure 5.15: Comparison of Shady Fire HONO concentrations (top panels) from the base run (blue) and the sensitivity tests that decreased (red) and increased (yellow) the pNO_3 photolysis rate by 50%. The rate of HONO formation from pNO_3 photolysis is shown in the bottom panels.

is already on the high end of those reported in literature and even this upper limit estimate provides a minor source of HONO within lofted plumes. Significantly higher NO_2 or aerosol concentrations would be needed for this source to be relevant in the HONO budget. As discussed above though, NO_2 conversion likely does play a role in plumes that reach the ground.

Increasing and decreasing the pNO_3 photolysis rate by 50% causes a similar magnitude change in the HONO source from this mechanism. This has a negligible impact on HONO concentrations in young smoke due to the large influence of emissions close to the fire. As the plume ages, though, there is a larger increase or decrease in HONO concentrations, with a change of 25% at 210 minutes and 44% at 300 minutes. There has been little research on

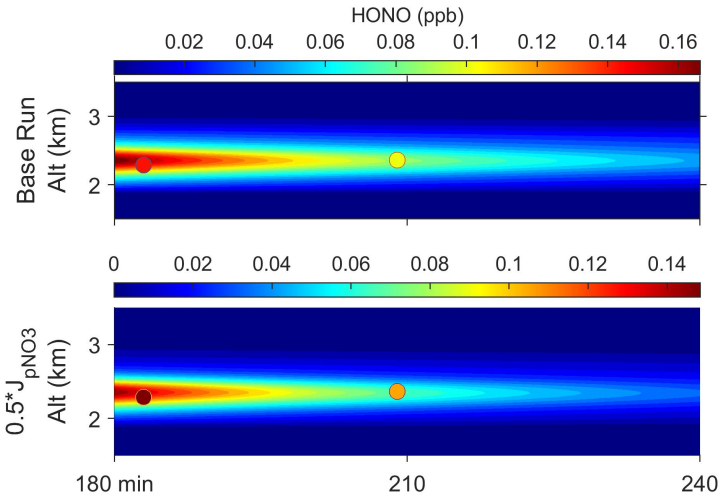

Figure 5.16: Shady Fire HONO concentrations from 180-240 minutes. The top panel shows the base run and the bottom shows the sensitivity test where the pNO_3 photolysis rate was halved. The base run shows better agreement with observations (circles), indicating HONO secondary formation is important in older smoke.

the photolysis rate of pNO_3 so it is unclear if the enhancement factor of 45 (Zhou et al., 2003; Karamchandani et al., 2014), determined from studies that focused on other surface types, is correct for biomass burning aerosols. It seems reasonable that similar chemistry would occur on aerosol surfaces, working to enhance the photolysis rate relative to gas-phase HNO_3. The complex aging associated with aerosols, especially in smoke plumes, makes this unclear however. In the Shady Fire example shown here, the addition of this HONO source leads to better predictions of HONO observations at later smoke ages (Figure 5.16). More studies focusing on HONO chemistry in plumes, especially in older smoke, are needed to determine if this heterogeneous source is relevant in all smoke plumes or strictly under certain conditions.

From the HONO budget discussed in Section 5.6, it was determined that fire emissions provide the major source of HONO in smoke plumes. Many global models exclude HONO fire emissions (Theys et al., 2020; Elshorbany et al., 2014) however, which impacts the OH

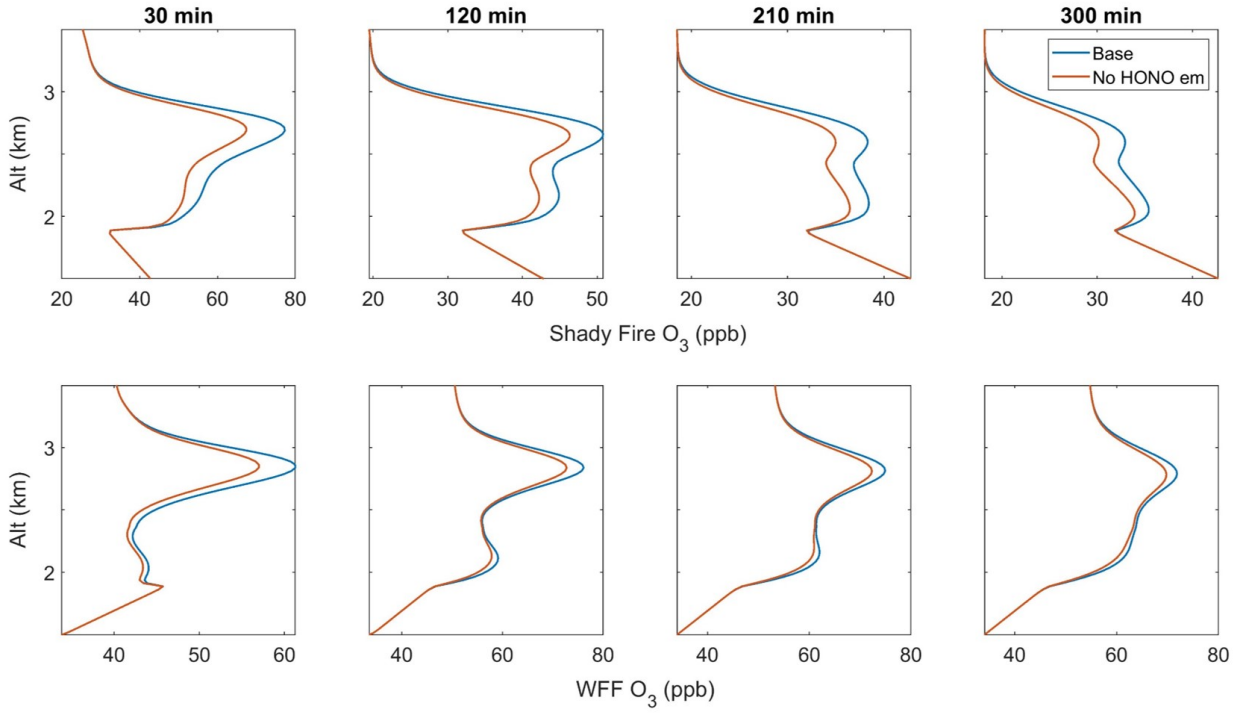

Figure 5.17: Comparison of O_3 concentrations from the base run (blue) and the sensitivity tests where HONO fire emissions are excluded from model (red). The Shady Fire is shown in the top panels and WFF is shown in the bottom panels.

budget and potential for secondary pollutants to form. To evaluate the impact HONO emissions have on O_3 levels for the Shady Fire and WFF, the model was re-run removing all HONO emissions (Figure 5.17). The greatest impact on O_3 levels occurs in young smoke where HONO emissions have the biggest influence on primary HO_x production. At 30 minutes, O_3 is decreased by up to 10 ppb in the Shady Fire and 5 ppb in WFF. The smaller changes in WFF are likely due to the lower photolysis rates throughout the model period, but O_3 was overpredicted at the start of the Shady Fire so the decrease seen there may be an overestimation. By the end of the model runs, the decrease in O_3 compared to the base run is 2 ppb. The values seen here are consistent with Theys et al. (2020), who reports that global model simulations of O_3 increase by up to 10% when HONO fire emissions are included.

5.8 Impact of vertical profiles on remote sensing

As discussed in Section 5.4, understanding the HONO vertical profile can help interpret in-situ measurements. The profile shape can also have significant impacts on remote sensing (RS) observations of smoke plumes. Over the past few years, there has been increased observation of plumes by satellite and airborne RS techniques (Theys et al., 2020; Griffin et al., 2020, 2021; Jin et al., 2021), including the mini-DOAS during FIREX-AQ. The conversion of DSCDs, which are the typical trace gas measurement value from RS, into VCDs requires knowledge of the trace gas profile. This can be difficult to estimate for fast reacting species like HONO and NO_x, especially from satellite data. Other studies have attempted to approximate the NO_x profile with cloud fractions (Jin et al., 2021) or aerosol corrections (Griffin et al., 2021). These approximations, however, do not accurately account for varying chemistry and photolysis rates, which increases the retrieval error.

Brockway (2021) compared the impact of using the HONO vertical profiles from PACT-1D (shown in Figure 5.9) versus the DIAL/HSRL aerosol profile for the FIREX-AQ mini-DOAS analysis. Using the PACT-1D profiles increased the retrieved HONO VCD by 15% and the retrieved maximum mixing ratio by nearly 60% over the first 2 hours after emission. This is attributed to the higher concentration of HONO lower in the plume where the mini-DOAS has less sensitivity. This decreased sensitivity at lower altitudes within a plume impacts all RS techniques due to light attenuation from smoke aerosols. These results clearly show the benefit of using chemical vertical profile modeling to aid in accurate RS HONO retrievals.

To avoid the impact of unknown vertical profiles, Theys et al. (2020) reported ratios of HONO to NO_2, which were both retrieved within the same wavelength range. Their study used a year of global satellite observations from TROPOMI. This approach, however, assumes similar HONO and NO_2 vertical profiles throughout the life of the plume. PACT-1D results indicate this may not be an accurate assumption for all fires. Figure 5.18 shows the vertical profiles of both species at different smoke ages for the Shady Fire and Figure 5.19

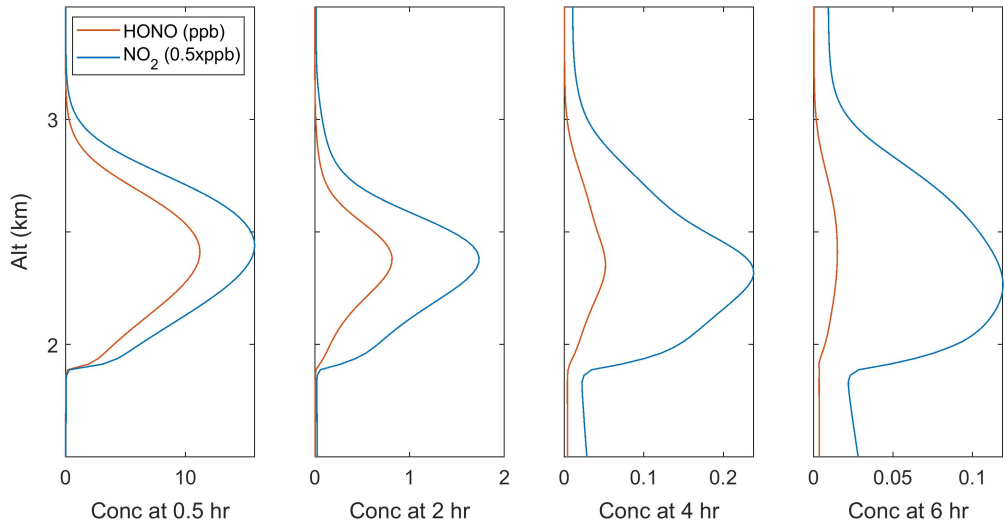

Figure 5.18: Vertical profiles of HONO (orange) and NO_2 within the Shady Fire plume at 0.5, 2, 4, and 6 hour smoke ages. NO_2 concentrations are halved for better comparison of the profiles. The profiles are similar in young smoke but vary as smoke ages.

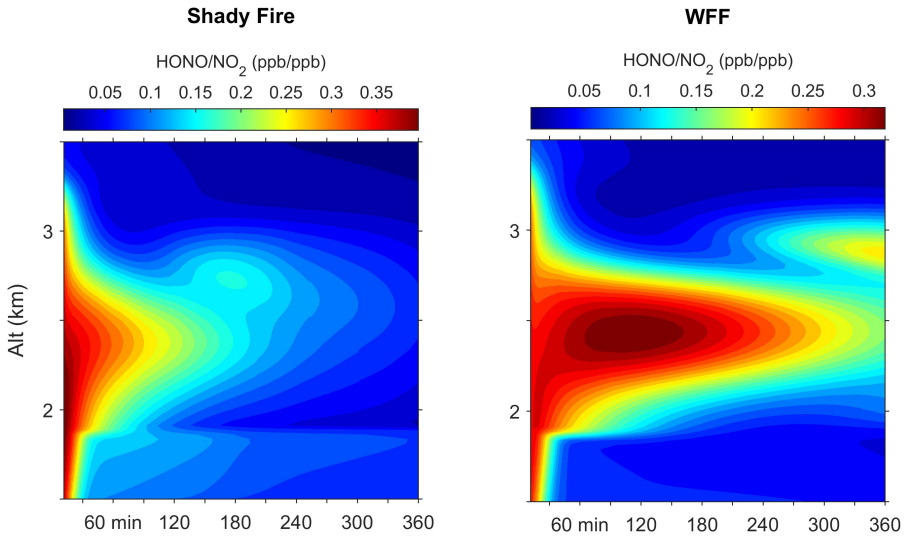

Figure 5.19: Ratio of HONO to NO_2 for the Shady Fire (left) and WFF (right). Within the plumes, the ratio generally decreases with smoke age.

shows the HONO/NO_2 ratios for both fires. There is a general decrease in the HONO/NO_2 ratio with smoke age, with the exception of a slight increase in the center of the WFF plume in the first hour. The values in young smoke agree well with the satellite and aircraft values reported by Theys et al. (2020) (0.29-0.54), and with the modeled values reported by Wang et al. (2021) for the WFF plume center (0.2-0.3). These values do not match for older smoke, however, especially for the thinner Shady Fire plume.

The vertical profiles of both species are similar in young smoke but change in older smoke. Upwelling radiation from below appears to photolyze HONO more efficiently than NO_2 at the plume bottom. This creates higher concentrations of NO_2 in the lower half of the plume relative to HONO. Again, this emphasizes the importance of understanding vertical profiles of reactive species when performing RS retrievals. While assuming a constant HONO/NO_2 ratio within the first 2 hours after emission may be reasonable, it likely leads to errors when analyzing observations of older smoke. PACT-1D is a useful tool for this purpose and can provide greater constraints on RS results.

5.9 Conclusions

HONO is emitted in large quantities from fires and photolyzes efficiently in smoke, providing a source of OH that can impact secondary pollutant formation in biomass burning plumes. Using PACT-1D, two wildfire smoke plumes from the FIREX-AQ campaign were successfully modeled. The implementation of an updraft speed and lateral mixing scheme allowed plume rise and dilution to be accurately simulated and results show good agreement with observations, capturing the general trends and magnitudes of key trace gas species. The chemical mechanism was also updated to include heterogeneous aerosol formation of HONO and a full chemical budget was analyzed to determine the major sources and sinks within these plumes. Figure 5.20 shows a sketch of the main processes that impact the budget.

HONO emissions from the fire provide the dominant source and are sustained in the

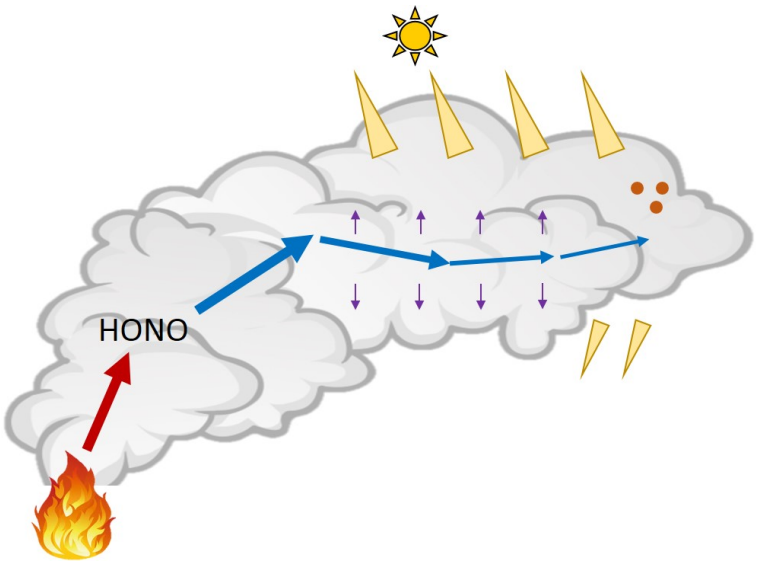

Figure 5.20: Cartoon of major processes impacting the HONO budget in biomass burning plumes. Emissions (red arrow) provide the main HONO source, which are transported (blue) downwind in the lower half of the plume. Efficient photolysis at the plume top and eventually at the bottom give HONO a unique vertical profile that varies with smoke age. Secondary sources only become important in older smoke after most of the initially emitted HONO is lost.

plume center due to low photolysis rates and minimal vertical mixing. The transport of these emissions allows HONO to contribute significantly to HO_x production, even hours downwind. pNO_3 photolysis becomes an important HONO source as the plumes age and the relative contribution of HONO emissions and secondary formation in older smoke depends strongly on the plume photolysis rates. HONO provides 80% of primary HO_x in young smoke, but this decreases with smoke age and HCHO becomes dominant within 1-4 hours after emission. The two sources show significantly different vertical profiles that should be considered when analyzing field observations. The large impact of HONO emissions on the HO_x budget enhances O_3 concentrations by up to 10 ppb in young smoke, emphasizing HONO's importance in predicting pollutant formation in biomass burning plumes.

CHAPTER 6

Conclusions and Outlook

6.1 Conclusion

Despite its important role as a radical precursor, HONO chemistry and sources are often excluded from or simplified in air quality models. This is largely due to uncertainties in HONO emissions and heterogeneous sources and leads to an underestimation of HONO concentrations, and consequently OH formation. The goal of this thesis was to advance the scientific knowledge of HONO chemistry in polluted environments and encourage the incorporation of HONO sources in air quality models. Accurately predicting the HO_x budget and formation of secondary pollutants like secondary organic aerosol and O_3 relies on a better understanding of HONO.

HONO measurements from two field campaigns conducted in polluted environments were presented and discussed in this work. CalNex 2010 was performed in urban Los Angeles and aimed to better understand atmospheric chemistry that leads to O_3 formation in southern California. During FIREX-AQ 2019, wildfire smoke plumes throughout the western United States were sampled via aircraft to study biomass burning emissions and downwind plume chemistry. Previous studies have shown that HONO plays a significant role in OH formation in both urban regions and biomass burning plumes, but the exact mechanisms behind HONO chemistry are still under debate. The large collection of trace gas, aerosol, and meteorological data during both experiments, including in-situ and remote sensing HONO measurements, provided ideal opportunities to better constrain HONO sources.

The new vertical column chemistry and transport model, PACT-1D, was developed as part of this thesis to interpret observations and study HONO chemistry that has generally been omitted from or simplified in air quality models. Combining observations with fine vertical-grid modeling can help identify HONO sources in different environments and determine how these sources impact the OH budget and secondary pollutant formation. The ability to include detailed heterogeneous chemistry on a molecular level, perform mechanistic studies, and analyze trace gas vertical profiles make PACT-1D an ideal tool to investigate fast reacting species formed on surfaces. In addition to HONO, it has been used recently to study chlorine and bromine chemistry on snow surfaces (Ahmed et al., 2021), and an ocean source of iodine. In this thesis, modeling studies were performed for a 3 day period during CalNex and for two different fires sampled during FIREX-AQ.

The observations from the CalNex campaign were well simulated using PACT-1D. Five heterogeneous sources of HONO at the ground were added to the model, which allowed an accurate description of the HONO concentrations and its diurnal profile. Without these sources, surface HONO was underestimated by up to 0.4 ppb during the day and 2 ppb at night. Vertical profiles of HONO, up to 400 m, were similarly underestimated without the ground sources, with the greatest impact seen at lower altitudes. This is evidence that heterogeneous chemistry provides a major source of HONO in urban areas and is necessary to accurately model HONO concentrations.

The shape of the vertical profiles, showing highest values near the ground and a quick decay with altitude, agree with previous studies (Kleffmann et al., 2003; Villena et al., 2011; Wong et al., 2011; Young et al., 2012; Vandenboer et al., 2013; Tsai et al., 2018) and supports the idea that HONO is formed primarily at the surface. The HONO budget shows that the main source aloft is vertical mixing from below, with some influence from particle nitrate (pNO_3) photolysis. The concentration profile emphasizes the need for measurements at multiple altitudes when studying boundary layer chemistry. For species like HONO, that are formed or emitted near the ground and are quickly lost before mixing vertically, the location

of a measurement can lead to a severe over or underestimation of total boundary layer concentrations. In the case of HONO, this has significant consequences on HO_x production estimates.

Primary HO_x production (P_{HOx}) from HONO photolysis was compared against HCHO and O_3, showing HONO is 2-3 times more important than the other sources below 10 m in the late morning (10:00-12:00). Similar to the HONO concentration profile, its impact on P_{HOx} decreases quickly with altitude and the three sources become comparable above 50 m. Both HCHO and O_3 show fairly constant contribution to P_{HOx} with height. Without an accurate description of HONO ground sources, OH concentrations below 10 m are reduced by 10-60% throughout the early morning and afternoon. Griffith et al. (2016) performed a more comprehensive HO_x budget analysis for CalNex, considering additional sources and sinks, and found similar production rates to the ones reported here at 10 m and below. Their study was based only on in-situ measurements near the the surface however, so the influence of altitude on P_{HOx}(HONO) is not discussed. This again stresses the need to consider vertical profiles.

After determining the importance of heterogeneous sources in the HONO budget, the contribution from each individual mechanism was analyzed. At night, the total ground source provided an additional $1x10^{10}$ to $5x10^{10}$ molecules cm^{-2} s^{-1} of HONO and was dominated by the NO_2 hydrolysis mechanism. The total source increased rapidly in the early morning, reaching up to $2.5x10^{11}$ molecules cm^{-2} s^{-1} during the day. Photolysis of surface HNO_3 was the main daytime source, making up 45-60% of the total, followed by photo-enhanced conversion of NO_2, which contributed 20-45%. Sensitivity studies were also performed to address uncertainties in the various heterogeneous mechanisms. Although the relative contribution of the two major daytime sources varied with each of these tests, they showed overall that both are important in Los Angeles and need to be included in the model to accurately simulate HONO concentrations.

Most previous studies agree that NO_2 hydrolysis provides the dominant nighttime HONO

source (Kleffmann et al., 2003; Wong et al., 2011; Vandenboer et al., 2013), and the PACT-1D results here support that conclusion. It has been suggested, however, that in polluted environments, photolysis of surface HNO_3/nitrate is much less important during the day than photo-enhanced NO_2 conversion (Zhou et al., 2003; Elshorbany et al., 2012). This work disputes that assumption, showing that HNO_3/nitrate photolysis is necessary to realistically model HONO. Pusede et al. (2015) examined the diurnal and weekday/weekend trends of HONO and NO_x during CalNex, and also concluded that NO_2 conversion cannot be the dominant formation mechanism. These results suggest that HNO_3/nitrate photolysis can indeed be significant in certain urban regions and should continue to be considered when updating air quality models.

In addition to an urban setting, PACT-1D was also used to simulate two biomass burning plumes sampled during the FIREX-AQ campaign, the Shady Fire and Williams Flats Fire (WFF). The model was updated with a smoke rise and dilution scheme and comparison of model results to observed CO concentrations and aerosol backscatter data shows PACT-1D successfully captures these key plume features. The dynamic nature of smoke, including variations in plume height, plume width, and emissions, complicate a direct comparison between model results and in-situ observations. Using data from the mini-DOAS instrument, which provides column average values of HONO and NO_2, provides an easier way to assess model performance since it removes the impact of measurement vertical variability. Overall, PACT-1D reasonably captures the general trend, magnitude, and chemistry of key trace gas species, and an analysis of the results provides important insight into the behavior of HONO in smoke plumes.

HONO concentrations in both plumes showed strong gradients with smoke age and altitude. In the youngest smoke, HONO levels are extremely high and exceed 20 ppb. A combination of dilution and chemistry causes a decrease with time, and concentrations drop to 0.05 ppb in the Shady Fire an 1.5 ppb in WFF by 240 minutes. At all smoke ages, the highest values are near the plume center and there is a sharp decay towards the plume top

and bottom. This vertical profile is more narrow than less-reactive species (CO, aerosols) that are typically used to determine plume height and width so needs to be considered when calculating the total concentration of HONO within smoke.

An analysis of primary HO_x production within the two modeled plumes shows that HONO provides nearly 80% of the total column HO_x in young smoke. This contribution decays with time and HCHO becomes dominant after a few hours. The transition from HONO to HCHO largely depends on the initial emissions and the thickness of the smoke, which controls in-plume photolysis rates. In this study, the Shady Fire was less intense and produced a thinner plume than WFF, so the contribution of HONO to P_{HOx} decreased much more quickly. In contrast, WFF is more representative of thick smoke plumes and showed a slower and steadier decline in P_{HOx}(HONO). Considering the large variations between fires and burning conditions, the overall values and trends in P_{HOx} seen here agree with other studies (Theys et al., 2020; Peng et al., 2020; Robinson et al., 2021; Wang et al., 2021).

Vertical profiles again provide important information that can be useful when determining the HO_x budget from observations. HCHO photolysis tends to produce more HO_x at the plume top, whereas, the peak production from HONO is lower in the plume and shows greater variation with smoke age. Because of this, observations collected in the upper portion of the plume may underestimate HONO's influence on the HO_x budget and the opposite is true for measurements towards the bottom of the plume. Vertical column models like PACT-1D are a useful tool to more accurately interpret observations and assess the full impact of chemistry throughout the entire plume height.

The HONO budget shows that emissions provide the major source within smoke plumes. Low photolysis rates in the plume center and minimal vertical mixing allow the emissions to be transported hours downwind, continuing to provide a source of OH at far distances from the fire. The amount of HONO emitted and the thickness of the smoke determine how far downwind the emissions play a significant role in the HONO and HO_x budgets. For WFF, they continued to be important throughout the entire 6 hour model run, whereas for the

Shady Fire, the influence was gone by 5 hours. Sensitivity tests removing HONO emissions were performed to determine how they impact O_3 formation. The largest differences were seen in young smoke, and at a 30 minute smoke age, O_3 was decreased by up to 10 ppb in the Shady Fire and 5 ppb in WFF. Comparing these two examples provides insight on how fire and plume conditions control the influence of HONO emissions. Larger fires with denser plumes can transport HONO farther downwind, having a significant impact on P_{HOx} far downwind, whereas in thinner plumes with higher photolysis rates, HONO emissions have a greater impact on O_3 formation close to the fire.

pNO_3 photolysis is the dominant secondary production mechanism, but does not play a significant role in the HONO budget until a few hours downwind, after most of the emissions have been lost through dilution or photolysis. The timing again depends on the initial emissions and thickness of the smoke. In the Shady Fire, for example, a near steady state is reached between the pNO_3 source and photolytic loss at 5 hours. Emissions are no longer important at this time, but HONO still contributes about 5% to primary HO_x production. Although this is much smaller than the impact from HCHO, HONO secondary sources still need to be considered to calculate an accurate HO_x budget as plumes age. At 5 hours in the thicker WFF plume, on the other hand, the emissions source is still considerably larger than secondary production. Heterogeneous conversion of NO_2 to form HONO was minor in the lofted plumes studied here but likely play a much larger role in plumes that reach the ground, as was seen in Chai et al. (2021) and Kaspari et al. (2021).

Other modeling work suggests that heterogeneous sources of HONO are needed at earlier plume ages to explain observations. These studies, however, suffer from either a lack of HONO measurements to validate model results (Alvarado and Prinn, 2009), or report over-estimated plume photolysis rates (i.e., overestimated HONO loss that is compensated by secondary production) (Wang et al., 2021). The more mechanistic and detailed description of HONO chemistry in PACT-1D likely does better job describing the HONO budget. There are large variations between fires and plume conditions though which impact the chemistry.

More detailed studies like this are therefore needed to better understand which factors are most influential in predicting secondary production of HONO in smoke.

6.2 Outlook

The measurements and model results presented in this thesis provide evidence that HONO is an important species to study in polluted environments. Its impact on OH formation needs to be considered to accurately construct a HO_x budget and predict secondary pollutant formation. Without primary HONO emissions and secondary sources, concentrations of HONO, OH and O_3 will be underestimated. The secondary source parameterizations described here should be incorporated into more widely used air quality models. In particular, the conversion of NO_2 to HONO on the ground (via both hydrolysis and the photo-enhanced mechanism) and photolysis of ground adsorbed HNO_3 and pNO_3 were essential in this work. Biomass burning HONO emissions can easily be included using either emission factor inventories (e.g, Andreae (2019) and Akagi et al. (2011)) or measured emission ratios. HONO observations should also ideally be included in all major field campaigns in polluted regions, and where possible, vertical profile measurements should be conducted.

The LP-DOAS was invaluable for understanding the rapid change of HONO with altitude in the CalNex study and allowed us to better understand the HO_x budget vertical profile in urban boundary layers. Additional measurements of HONO and its precursors at even lower altitudes would be helpful to constrain the impact of inefficient mixing in the lowest part of the atmosphere. PACT-1D simulated the transport of species to and from the ground using a logarithmic vertical grid below 1 m but there were no measurements from the campaign that could confirm the atmospheric mixing parameterizations in the model. Flux or turbulence measurements at ground level would provide confidence in the surface deposition and emissions that PACT-1D simulates. These parameters are essential to heterogeneous chemistry so reducing their uncertainty would allow us to focus solely on the chemistry. Field

measurements of surface HNO_3/nitrate concentrations and additional laboratory studies to constrain its photolysis rate and the NO_2 uptake coefficient are also major variables that would aid in constraining the HONO budget.

The lack of vertical profile measurements during FIREX-AQ was a challenge in this work and future aircraft campaigns should place more emphasis on observing the entire plume height by repeating transects at multiple altitudes. This will allow us to better understand how reactive species and chemistry vary vertically in smoke. In addition to helping interpret in-situ measurements and validate models, this information is also important for satellite retrievals. The use of satellites to observe smoke plumes and their air quality impacts has increased in recent years and provide a promising way to assess global changes in biomass burning due to climate change. An accurate analysis of remotely sensed NO_x and HONO, however, requires vertical profile information. Field experiments therefore need to prioritize vertical measurements before the scientific community can confidently use these satellite observations

The fact that photolysis rates change by orders of magnitude within a plume was also difficult to initialize in PACT-1D and additional measurements would allow us to more confidently parameterize the vertical profile shape of these rates. Another option to better constrain photolysis is to use more advanced radiative transfer models (RTMs). VLIDORT-QS, the RTM used in this work, is currently being updated to output vertical profiles of actinic fluxes and photolysis rates. These are not standard output parameters but are essential to accurately model chemistry within smoke plumes. The HONO and HO_x budgets are both highly dependent on photolysis rates and a more accurate representation will lead to better predictions of secondary pollutant formation.

A focus on sampling older smoke would also help to constrain the impact of HONO secondary sources in biomass burning plumes. In both of the plumes studied here, there were no observations in smoke older than 240 minutes. One of the major air quality concerns for biomass burning is the impact of smoke mixing with urban pollution as its transported

to population centers, which typically occurs much farther downwind from the burning site. On one of the sampling days during FIREX-AQ (August 7, 2019), the DC-8 aircraft did sample aged smoke for about an hour as it flew between two different fires. The trajectory analysis estimated that the smoke age varied between 7 and 90 hours, however, there are large uncertainties due to difficulty identifying the fire location and the possibility of mixed smoke from multiple fires. The in-situ HONO measurements during this time period were near background levels so it is uncertain if secondary sources are contributing to the HONO budget in this aged smoke. More measurements and modeling studies are required to predict if HONO levels are sustained in older smoke through secondary formation and how this chemistry changes when mixing with urban pollution plumes. The results from the CalNex study showed how important ground sources of HONO are in urban boundary layers and its reasonable to expect these sources will increase with a large influx of NO_x from wildfire smoke. This thesis focused on HONO chemistry in these two separate environments but the growing threat of wildfires in the western United States make it inevitable that urban centers will experience increased wildfire smoke pollution. More work is therefore needed to understand how HONO sources and the production of OH change in this unique combined environment that connects biomass burning and urban air quality.

Bibliography

K. Acker, A. Febo, S. Trick, C. Perrino, P. Bruno, P. Wiesen, D. Möller, W. Wieprecht, R. Auel, M. Giusto, A. Geyer, U. Platt, and I. Allegrini. Nitrous acid in the urban area of Rome. *Atmospheric Environment*, 40(17):3123–3133, 2006. ISSN 13522310. doi: 10.1016/j.atmosenv.2006.01.028.

Shaddy Ahmed, Jennie L Thomas, Katie Tuite, Jochen Stutz, John J Orlando, Rebecca S Hornbrook, Eric C Apel, K Louisa, Detlev Helmig, Patrick Boylan, L Gregory Huey, R Samuel, Kirk Ullmann, Christopher A Cantrell, and Alan Fried. The role of snow in controlling halogen chemistry and boundary layer oxidation during Arctic spring : A 1D modelling case study. pages 1–41, 2021. doi: 10.1029/2021JD036140.

S. K. Akagi, R. J. Yokelson, C. Wiedinmyer, M. J. Alvarado, J. S. Reid, T. Karl, J. D. Crounse, and P. O. Wennberg. Emission factors for open and domestic biomass burning for use in atmospheric models. *Atmospheric Chemistry and Physics*, 11(9):4039–4072, 2011. ISSN 16807316. doi: 10.5194/acp-11-4039-2011.

S. K. Akagi, J. S. Craven, J. W. Taylor, G. R. McMeeking, R. J. Yokelson, I. R. Burling, S. P. Urbanski, C. E. Wold, J. H. Seinfeld, H. Coe, M. J. Alvarado, and D. R. Weise. Evolution of trace gases and particles emitted by a chaparral fire in California. *Atmospheric Chemistry and Physics*, 12(3):1397–1421, 2012. ISSN 16807316. doi: 10.5194/acp-12-1397-2012.

B. Alicke, U. Platt, and J. Stutz. Impact of nitrous acid photolysis on the total hydroxyl radical budget during the Limitation of Oxidant Productioh/Pianura Padana Produzione di Ozono study in Milan. *Journal of Geophysical Research Atmospheres*, 107(22), 2002. ISSN 01480227. doi: 10.1029/2000JD000075.

B. Alicke, A. Geyer, A. Hofzumahaus, F. Holland, S. Konrad, H. W. Pätz, J. Schäfer, J. Stutz, A. Volz-Thomas, and U. Platt. OH formation by HONO photolysis during the

BERLIOZ experiment. *Journal of Geophysical Research D: Atmospheres*, 108(4):3–1, 2003. ISSN 01480227. doi: 10.1029/2001jd000579.

M. J. Alvarado and R. G. Prinn. Formation of ozone and growth of aerosols in young smoke plumes from biomass burning: 1. Lagrangian parcel studies. *Journal of Geophysical Research Atmospheres*, 114(9):1–19, 2009. ISSN 01480227. doi: 10.1029/2008JD011144.

M. J. Alvarado, C. Wang, and R. G. Prinn. Formation of ozone and growth of aerosols in young smoke plumes from biomass burning: 2. Three-dimensional Eulerian studies. *Journal of Geophysical Research Atmospheres*, 114(9):1–27, 2009. ISSN 01480227. doi: 10.1029/2008JD011186.

M. Ammann, M. Kalberer, D. T. Jost, L. Tobler, E. Rössler, D. Piguet, H. W. Gäggeler, and U. Baltensperger. Heterogeneous production of nitrous acid on soot in polluted air masses. *Nature*, 395(6698):157–160, 1998. ISSN 00280836. doi: 10.1038/25965.

M. Andreae. Emission of trace gases and aerosols from biomass burning - an updated assessment. *Atomospheric Chemistry and Physics*, 15 (4)(April):955–966, 2019.

D. G. Aubin and J. P. D. Abbatt. Interaction of NO2 with hydrocarbon soot: Focus on HONO yield, surface modification, and mechanism. *Journal of Physical Chemistry A*, 111 (28):6263–6273, 2007. ISSN 10895639. doi: 10.1021/jp068884h.

A. M. Baergen and D. J. Donaldson. Photochemical Renoxi fi cation of Nitric Acid on Real Urban Grime. *Environmental Science & Technology*, 47:815–820, 2013. doi: 10.1021/es3037862.

A. M. Baergen and D. J. Donaldson. Formation of reactive nitrogen oxides from urban grime photochemistry. *Atmospheric Chemistry and Physics*, 16:6355–6363, 2016. doi: 10.5194/acp-16-6355-2016.

T. Bartels-Rausch, M. Brigante, Y. F. Elshorbany, M. Ammann, B. D'Anna, C. George, K. Stemmler, M. Ndour, and J. Kleffmann. Humic acid in ice: Photo-enhanced conversion of nitrogen dioxide into nitrous acid. *Atmospheric Environment*, 44(40):5443–5450, 2010. ISSN 13522310. doi: 10.1016/j.atmosenv.2009.12.025.

R. Beelen, G. Hoek, O. Raaschou-Nielsen, M. Stafoggia, Z. J. Andersen, G. Weinmayr, B. Hoffmann, K. Wolf, E. Samoli, P. H. Fischer, M. J. Nieuwenhuijsen, W. W. Xun, K. Katsouyanni, K. Dimakopoulou, A. Marcon, E. Vartiainen, T. Lanki, T. Yli-Tuomi, B. Oftedal, P. E. Schwarze, P. Nafstad, U. de Faire, N. L. Pedersen, C. G. Östenson, L. Fratiglioni, J. Penell, M. Korek, G. Pershagen, K. T. Eriksen, K. Overvad, M. Sørensen, M. Eeftens, P. H. Peeters, K. Meliefste, M. Wang, H. Bas Bueno-De-Mesquita, D. Sugiri, U. Krämer, J. Heinrich, K. De Hoogh, T. Key, A. Peters, R. Hampel, H. Concin, G. Nagel, A. Jaensch, A. Ineichen, M. Y. Tsai, E. Schaffner, N. M. Probst-Hensch, C. Schindler, M. S. Ragettli, A. Vilier, F. Clavel-Chapelon, C. Declercq, F. Ricceri, C. Sacerdote, C. Galassi, E. Migliore, A. Ranzi, G. Cesaroni, C. Badaloni, F. Forastiere, M. Katsoulis, A. Trichopoulou, M. Keuken, A. Jedynska, I. M. Kooter, J. Kukkonen, R. S. Sokhi, P. Vineis, and B. Brunekreef. Natural-cause mortality and long-term exposure to particle components: An Analysis of 19 European cohorts within the multi-center ESCAPE project. *Environmental Health Perspectives*, 123(6):525–533, 2015. ISSN 15529924. doi: 10.1289/ehp.1408095.

A. J. Beyersdorf, L. D. Ziemba, G. Chen, C. A. Corr, J. H. Crawford, G. S. Diskin, R. H. Moore, K. L. Thornhill, E. L. Winstead, and B. E. Anderson. The impacts of aerosol loading, composition, and water uptake on aerosol extinction variability in the Baltimore-Washington, D.C. region. *Atmospheric Chemistry and Physics*, 16(2):1003–1015, 2016. ISSN 16807324. doi: 10.5194/acp-16-1003-2016.

A. Borbon, J. B. Gilman, W. C. Kuster, N. Grand, S. Chevaillier, A. Colomb, C. Dolgorouky, V. Gros, M. Lopez, R. Sarda-Esteve, J. Holloway, J. Stutz, H. Petetin, S. McKeen,

M. Beekmann, C. Warneke, D. D. Parrish, and J. A. De Gouw. Emission ratios of anthropogenic volatile organic compounds in northern mid-latitude megacities: Observations versus emission inventories in Los Angeles and Paris. *Journal of Geophysical Research Atmospheres*, 118(4):2041–2057, 2013. ISSN 21698996. doi: 10.1002/jgrd.50059.

M. Boy, A. Sogachev, J. Lauros, L. Zhou, A. Guenther, and S. Smolander. SOSA - A new model to simulate the concentrations of organic vapours and sulphuric acid inside the ABL - Part 1: Model description and initial evaluation. *Atmospheric Chemistry and Physics*, 11(1):43–51, 2011. ISSN 16807316. doi: 10.5194/acp-11-43-2011.

G. P. Brasseur and D. J. Jacob. *Modeling of Atmospheric Chemistry*. Cambridge University Press, 2017. doi: 10.1017/9781316544754.

M. Brigante, D. Cazoir, B. D'Anna, C. George, and D. J. Donaldson. Photoenhanced uptake of NO2 by pyrene solid films. *Journal of Physical Chemistry A*, 112(39):9503–9508, 2008. ISSN 10895639. doi: 10.1021/jp802324g.

N. Brockway. *Airborne Remote Sensing of Radical Precursors in Biomass Burning Smoke Plumes: Emissions, Chemistry, and Radiative Transfer*. PhD thesis, University of California Los Angeles, 2021.

R. D. Brook, S. Rajagopalan, C. A. Pope, J. R. Brook, A. Bhatnagar, A. V. Diez-Roux, F. Holguin, Y. Hong, R. V. Luepker, M. A. Mittleman, A. Peters, D. Siscovick, S. C. Smith, L. Whitsel, and J. D. Kaufman. Particulate matter air pollution and cardiovascular disease: An update to the scientific statement from the american heart association. *Circulation*, 121(21):2331–2378, 2010. ISSN 00097322. doi: 10.1161/CIR.0b013e3181dbece1.

R. R. Buchholz, L.K. Emmons, S. Tilmes, and The CESM2 Development Team. CESM2.1/CAM-chem Instantaneous Output for Boundary Conditions. UCAR/NCAR - Atmospheric Chemistry Observations and Modeling Laboratory. 2019. doi: https://doi.org/10.5065/NMP7-EP60.

I. R. Burling, R. J. Yokelson, D. W.T. Griffith, T. J. Johnson, P. Veres, J. M. Roberts, C. Warneke, S. P. Urbanski, J. Reardon, D. R. Weise, W. M. Hao, and J. De Gouw. Laboratory measurements of trace gas emissions from biomass burning of fuel types from the southeastern and southwestern United States. *Atmospheric Chemistry and Physics*, 10(22):11115–11130, 2010. ISSN 16807316. doi: 10.5194/acp-10-11115-2010.

L. Cao, H. Sihler, U. Platt, and E. Gutheil. Numerical analysis of the chemical kinetic mechanisms of ozone depletion and halogen release in the polar troposphere. *Atmospheric Chemistry and Physics*, 14(7):3771–3787, 2014. ISSN 16807324. doi: 10.5194/acp-14-3771-2014.

L. Cao, U. Platt, and E. Gutheil. Role of the Boundary Layer in the Occurrence and Termination of the Tropospheric Ozone Depletion Events in Polar Spring. *Atmospheric Environment*, 132:98–110, 2016. ISSN 1352-2310. doi: 10.1016/j.atmosenv.2016.02.034.

M. Cazorla, G. M. Wolfe, S. A. Bailey, A. K. Swanson, H. L. Arkinson, and T. F. Hanisco. A new airborne laser-induced fluorescence instrument for in situ detection of formaldehyde throughout the troposphere and lower stratosphere. *Atmospheric Measurement Techniques*, 8(2):541–552, 2015. ISSN 18678548. doi: 10.5194/amt-8-541-2015.

J. Chai, J. E. Dibb, B. E. Anderson, C. Bekker, Blumm D. E., E. Heim, C. Jordan, E. E. Joyce, J. Kaspari, H. Munro, W. Walters, and M. Hastings. Isotopic evidence for dominant secondary production of HONO in near-ground wildfire plumes. *Atmospheric Chemistry and Physics*, 21(22):13077–13098, 2021. ISSN 16807324. doi: 10.5194/acp-21-13077-2021.

K. R. Chan, J. Dean-Day, S. W. Bowen, and T. P. Bui. Turbulence measurements by the DC-8 meteorological measurement system. 25(9):1355–1358, 1998.

B. H. Czader, B. Rappenglück, P. Percell, D. W. Byun, F. Ngan, and S. Kim. Modeling nitrous acid and its impact on ozone and hydroxyl radical during the Texas Air Quality

Study 2006. *Atmospheric Chemistry and Physics*, 12(15):6939–6951, 2012. ISSN 16807316. doi: 10.5194/acp-12-6939-2012.

L. M. David, A. R. Ravishankara, S. J. Brey, E. V. Fischer, J. Volckens, and S. Kreidenweis. Could the exception become the rule? 'Uncontrollable' air pollution events in the US due to wildland fires. *Environmental Research Letters*, 16(3), 2021. ISSN 17489326. doi: 10.1088/1748-9326/abe1f3.

P. F. Decarlo, J. R. Kimmel, A. Trimborn, M. J. Northway, J. T. Jayne, A. C. Aiken, M. Gonin, K. Fuhrer, T. Horvath, K. S. Docherty, D. R. Worsnop, and J. L. Jimenez. Field-Deployable, High-Resolution, Time-of-Flight Aerosol Mass Spectrometer. *Analytical Chemistry*, 78(24):8281–8289, 2006. ISSN 0003-2700. doi: 8410.1029/2001JD001213.Analytical.

S. Dusanter, D. Vimal, P. S. Stevens, R. Volkamer, and L. T. Molina. Measurements of OH and HO2 concentrations during the MCMA-2006 field campaign - Part 1: deployment of the indiana university laser-induced fluorescence instrument. *Atmospheric Chemistry and Physics*, 9(5):1665–1685, 2009. ISSN 16807324. doi: 10.5194/acp-9-1665-2009.

Y F Elshorbany, R Kurtenbach, P Wiesen, E Lissi, M Rubio, G Villena, E Gramsch, A R Rickard, MJ Pilling, and J Kleffmann. Oxidation capacity of the city air of Santiago, Chile. *Atmospheric Chemistry and Physics*, 9(3):2257–2273, 2009. doi: 10.5194/acp-9-2257-2009.

Y. F. Elshorbany, B. Steil, C. Brühl, and J. Lelieveld. Impact of HONO on global atmospheric chemistry calculated with an empirical parameterization in the EMAC model. *Atmospheric Chemistry and Physics Discussions*, 12(5):12885–12934, 2012. ISSN 1680-7375. doi: 10.5194/acpd-12-12885-2012.

Y. F. Elshorbany, P. J. Crutzen, B. Steil, A. Pozzer, H. Tost, and J. Lelieveld. Global and regional impacts of HONO on the chemical composition of clouds and aerosols. *Atmospheric*

Chemistry and Physics, 14(3):1167–1184, 2014. ISSN 16807316. doi: 10.5194/acp-14-1167-2014.

L. K. Emmons, R. H. Schwantes, J. J. Orlando, G. Tyndall, D. Kinnison, J. F. Lamarque, D. Marsh, M. J. Mills, S. Tilmes, C. Bardeen, R. R. Buchholz, A. Conley, A. Gettelman, R. Garcia, I. Simpson, D. R. Blake, S. Meinardi, and G. Pétron. The Chemistry Mechanism in the Community Earth System Model Version 2 (CESM2). *Journal of Advances in Modeling Earth Systems*, 12(4):1–21, 2020. ISSN 19422466. doi: 10.1029/2019MS001882.

Z. L. Fleming, R. M. Doherty, E. Von Schneidemesser, C. S. Malley, O. R. Cooper, J. P. Pinto, A. Colette, X. Xu, D. Simpson, M. G. Schultz, A. S. Lefohn, S. Hamad, R. Moolla, S. Solberg, and Z. Feng. Tropospheric Ozone Assessment Report: Present-day ozone distribution and trends relevant to human health. *Elementa*, 6, 2018. ISSN 23251026. doi: 10.1525/elementa.273.

X. Fu, T. Wang, L. Zhang, Q. Li, Z. Wang, M. Xia, H. Yun, W. Wang, C. Yu, D. Yue, Y. Zhou, J. Zheng, and R. Han. The significant contribution of HONO to secondary pollutants during a severe winter pollution event in southern China. *Atmospheric Chemistry and Physics*, 19(1):1–14, 2019. ISSN 16807324. doi: 10.5194/acp-19-1-2019.

N. A. Fuchs and A. G. Sutugin. High-dispersed aerosols. In *Topics in current aerosol research*. Elsevier, 1971.

C. George, R. S. Strekowski, J. Kleffmann, K. Stemmler, and M. Ammann. Photoenhanced uptake of gaseous NO2 on solid organic compounds: A photochemical source of HONO? *Faraday Discussions*, 130(2):195–210, 2005. ISSN 13596640. doi: 10.1039/b417888m.

A. Geyer and J. Stutz. The vertical structure of OH-HO2 -RO2 chemistry in the nocturnal boundary layer: A one-dimensional model study. *Journal of Geophysical Research*, 109 (D16):1–17, 2004a. ISSN 0148-0227. doi: 10.1029/2003JD004425.

A. Geyer and J. Stutz. Vertical profiles of NO3, N2O5, O3, and NOx in the nocturnal boundary layer: 2. Model studies on the altitude dependence of composition and chemistry. *Journal of Geophysical Research*, 109(D12):1–18, 2004b. ISSN 0148-0227. doi: 10.1029/2003JD004211.

J. B. Gilman, J. F. Burkhart, B. M. Lerner, E. J. Williams, W. C. Kuster, P. D. Goldan, P. C. Murphy, C. Warneke, C. Fowler, S. A. Montzka, B. R. Miller, L. Miller, S. J. Oltmans, T. B. Ryerson, O. R. Cooper, A. Stohl, and J. A. De Gouw. Ozone variability and halogen oxidation within the Arctic and sub-Arctic springtime boundary layer. *Atmospheric Chemistry and Physics*, 10(21):10223–10236, 2010. ISSN 16807316. doi: 10.5194/acp-10-10223-2010.

P. Glarborg, J. A. Miller, B. Ruscic, and S. J. Klippenstein. Modeling nitrogen chemistry in combustion. *Progress in Energy and Combustion Science*, 67:31–68, 2018. ISSN 03601285. doi: 10.1016/j.pecs.2018.01.002.

W. S. Goliff, W. R. Stockwell, and C. V. Lawson. The regional atmospheric chemistry mechanism, version 2. *Atmospheric Environment*, 68(x):174–185, 2013. ISSN 13522310. doi: 10.1016/j.atmosenv.2012.11.038.

C. Granier, S. Darras, H. Denier Van Der Gon, D. Jana, N. Elguindi, G. Bo, G. Michael, G. Marc, J. P. Jalkanen, and J. Kuenen. The Copernicus Atmosphere Monitoring Service global and regional emissions (April 2019 version). Data from ECCAD. (April), 2019. URL `https://hal.archives-ouvertes.fr/hal-02322431`.

D. Griffin, C. Sioris, J. Chen, N. Dickson, A. Kovachik, M. De Graaf, S. Nanda, P. Veefkind, E. Dammers, C. A. McLinden, P. Makar, and A. Akingunola. The 2018 fire season in North America as seen by TROPOMI: Aerosol layer height intercomparisons and evaluation of model-derived plume heights. *Atmospheric Measurement Techniques*, 13(3):1427–1445, 2020. ISSN 18678548. doi: 10.5194/amt-13-1427-2020.

D. Griffin, C. A. McLinden, E. Dammers, C. Adams, C. E. Stockwell, C. Warneke, I. Bourgeois, J. Peischl, T. B. Ryerson, K. J. Zarzana, J. P. Rowe, R. Volkamer, C. Knote, N. Kille, T. K. Koenig, C. F. Lee, D. Rollins, P. S. Rickly, J. Chen, L. Fehr, A. Bourassa, D. Degenstein, K. Hayden, C. Mihele, S. N. Wren, J. Liggio, A. Akingunola, and P. Makar. Biomass burning nitrogen dioxide emissions derived from space with TROPOMI: Methodology and validation. *Atmospheric Measurement Techniques*, 14(12):7929–7957, 2021. ISSN 18678548. doi: 10.5194/amt-14-7929-2021.

S. M. Griffith, R. F. Hansen, S. Dusanter, V. Michoud, J. B. Gilman, W.C. Kuster, P.R. Veres, M. Graus, J. A. de Gouw, J. Roberts, C. Young, R. Washenfelder, S.S. Brown, R. Thalman, E. Waxman, R. Volkamer, C. Tsai, J. Stutz, J. H. Flynn, N. B Grossberg, and P. S. Stevens. Measurements of hydroxyl and hydroperoxy radicals during CalNex-LA: Model comparisons and radical budgets. *Journal of Geophysical Research : Atmospheres*, pages 4211–4232, 2016. doi: 10.1002/2015JD024358.Received.

H. Guo, J. Liu, K. D. Froyd, J. M. Roberts, P. R. Veres, P. L. Hayes, J. L. Jimenez, A. Nenes, and R. J. Weber. Fine particle pH and gas-particle phase partitioning of inorganic species in Pasadena, California, during the 2010 CalNex campaign. *Atmospheric Chemistry and Physics*, 17(9):5703–5719, 2017. ISSN 16807324. doi: 10.5194/acp-17-5703-2017.

L. Gutzwiller, F. Arens, U. Baltensperger, H. W. Gäggeler, and M. Ammann. Significance of semivolatile diesel exhaust organics for secondary HONO formation. *Environmental Science and Technology*, 36(4):677–682, 2002. ISSN 0013936X. doi: 10.1021/es015673b.

J. W. Hair, C. A. Hostetler, A. L. Cook, D. B. Harper, R. A. Ferrare, T. L. Mack, W. Welch, Luis R. Izquierdo, and F. E. Hovis. Airborne High Spectral Resolution Lidar for profiling Aerosol optical properties. *Applied Optics*, 47(36):6734–6753, 2008. ISSN 15394522. doi: 10.1364/AO.47.006734.

P. L. Hayes, A. M. Ortega, M. J. Cubison, K. D. Froyd, Y. Zhao, S. S. Cliff, W. W. Hu, D. W. Toohey, J. H. Flynn, B. L. Lefer, N. Grossberg, S. Alvarez, B. Rappenglück, J. W.

Taylor, J. D. Allan, J. S. Holloway, J. B. Gilman, W. C. Kuster, J. A. De Gouw, P. Massoli, X. Zhang, J. Liu, R. J. Weber, A. L. Corrigan, L. M. Russell, G. Isaacman, D. R. Worton, N. M. Kreisberg, A. H. Goldstein, R. Thalman, E. M. Waxman, R. Volkamer, Y. H. Lin, J. D. Surratt, T. E. Kleindienst, J. H. Offenberg, S. Dusanter, S. Griffith, P. S. Stevens, J. Brioude, W. M. Angevine, and J. L. Jimenez. Organic aerosol composition and sources in Pasadena, California, during the 2010 CalNex campaign. *Journal of Geophysical Research Atmospheres*, 118(16):9233–9257, 2013. ISSN 21698996. doi: 10.1002/jgrd.50530.

D. A. Jaffe and N. L. Wigder. Ozone production from wildfires: A critical review. *Atmospheric Environment*, 51:1–10, 2012. ISSN 13522310. doi: 10.1016/j.atmosenv.2011.11.063.

D. A. Jaffe, N. Wigder, N. Downey, G. Pfister, A. Boynard, and S. B. Reid. Impact of wildfires on ozone exceptional events in the western U.S. *Environmental Science and Technology*, 47(19):11065–11072, 2013. ISSN 0013936X. doi: 10.1021/es402164f.

M. E. Jenkin, R. A. Cox, and D. J. Williams. Laboratory studies of the kinetics of formation of nitrous acid from the thermal reaction of nitrogen dioxide and water vapour. *Atmospheric Environment*, 22(3):487–498, 1988. doi: 10.1016/0004-6981(88)90194-1.

X. Jin, Q. Zhu, and R. C. Cohen. Direct estimates of biomass burning NOx emissions and lifetimes using daily observations from TROPOMI. *Atmospheric Chemistry and Physics*, 21(20):15569–15587, 2021. ISSN 16807324. doi: 10.5194/acp-21-15569-2021.

M. Kalberer, M. Ammann, F. Arens, H. W. Gaggeler, and U Baltensperger. Heterogeneous formation of nitrous acid (HONO) on soot aerosol particles. 104:13825–13832, 1999.

P. Karamchandani, C. Emery, G. Yarwood, B. Lefer, J. Stutz, E. Couzo, and W. Vizuete. Implementation and refinement of a surface model for heterogeneous HONO formation in a 3-D chemical transport model. *Atmospheric Environment*, 112:356–368, 2014. ISSN 18732844. doi: 10.1016/j.atmosenv.2015.01.046.

A. Karanasiou, A. Alastuey, Fu. Amato, M. Renzi, M. Stafoggia, A. Tobias, C. Reche, F. Forastiere, S. Gumy, P. Mudu, and X. Querol. Short-term health effects from outdoor exposure to biomass burning emissions: A review. *Science of the Total Environment*, 781: 146739, 2021. ISSN 18791026. doi: 10.1016/j.scitotenv.2021.146739.

J. H. Kaspari, J. Chai, B. E. Anderson, C. E. Jordan, E. Scheuer, M. G. Hastings, and J. E. Dibb. Influence of Solar Irradiation on Nitrous Acid Production in Western U.S. Wildfire Smoke. *Journal of Geophysical Research : Atmospheres*, 2021.

W. C. Keene, J. M. Lobert, P. J. Crutzen, J. R. Maben, D. H. Scharffe, T. Landmann, C. Hély, and C. Brain. Emissions of major gaseous and particulate species during experimental burns of southern African biomass. *Journal of Geophysical Research Atmospheres*, 111(4), 2006. ISSN 01480227. doi: 10.1029/2005JD006319.

A. F. Khalizov, M. Cruz-Quinones, and R. Zhang. Heterogeneous reaction of NO2 on fresh and coated soot surfaces. *Journal of Physical Chemistry A*, 114(28):7516–7524, 2010. ISSN 10895639. doi: 10.1021/jp1021938.

S. Kim, B. C. Mcdonald, S. Baidar, S. S. Brown, B. Dube, R. A. Ferrare, G. J. Frost, R. A. Harley, J. S. Holloway, H. Lee, S. A. Mckeen, J. A. Neuman, J. B. Nowak, H. Oetjen, I. Ortega, I. B. Pollack, J. M. Roberts, T. B. Ryerson, A. J. Scarino, C. J. Senff, R. Thalman, M. Trainer, R. Volkamer, N. Wagner, R. A. Washenfelder, E. Waxman, and C. J. Young. Modeling the weekly cycle of NOx and CO emissions and their impacts on O3 in the Los Angeles-South Coast Air Basin during the CalNex 2010 field campaign. *Journal of Geophysical Research : Atmospheres*, pages 1340–1360, 2016. doi: 10.1002/2015JD024292.Received.

T. W. Kirchstetter, R. A. Harley, and D. Littlejohn. Measurement of nitrous acid in motor vehicle exhaust. *Environmental Science and Technology*, 30:2843–2849, 1996. doi: 10.1021/es960135y.

J. Kleffmann. Daytime sources of nitrous acid (HONO) in the atmospheric boundary layer. *ChemPhysChem*, 8(8):1137–1144, 2007. ISSN 1439-4235. doi: 10.1002/cphc.200700016.

J. Kleffmann, R. Kurtenbach, J. Lörzer, P. Wiesen, N. Kalthoff, B. Vogel, and H. Vogel. Measured and simulated vertical profiles of nitrous acid - Part I: Field measurements. *Atmospheric Environment*, 37(21):2949–2955, 2003. ISSN 13522310. doi: 10.1016/S1352-2310(03)00242-5.

J. Kleffmann, T. Gavriloaiei, A. Hofzumahaus, F. Holland, R. Koppmann, L. Rupp, E. Schlosser, M. Siese, and A. Wahner. Daytime formation of nitrous acid: A major source of OH radicals in a forest. *Geophysical Research Letters*, 32(5):1–4, 2005. ISSN 00948276. doi: 10.1029/2005GL022524.

J. Kleffmann, J. C. Lörzer, P. Wiesen, C. Kern, S. Trick, R. Volkamer, M. Rodenas, and K. Wirtz. Intercomparison of the DOAS and LOPAP techniques for the detection of nitrous acid (HONO). *Atmospheric Environment*, 40(20):3640–3652, 2006. ISSN 13522310. doi: 10.1016/j.atmosenv.2006.03.027.

L. Kramer, L. Crilley, T. Adams, S. Ball, F.s Pope, and W. Bloss. Nitrous acid (HONO) emissions under real-world driving conditions from vehicles in a UK road tunnel. *Atmospheric Chemistry and Physics*, (2):1–31, 2019. ISSN 1680-7316. doi: 10.5194/acp-2019-1070.

R. Kurtenbach, K.H. Becker, J.A.G. Gomes, J. Kleffmann, J.C. Lorzer, M. Spittler, P. Wiesen, R. Ackermann, A. Geyer, and U. Platt. Investigations of emissions and heterogeneous formation of HONO in a road traffic tunnel. *Atmospheric Environment*, 35: 3385–3394, 2001. doi: 10.1016/S1352-2310(01)00138-8.

G. Lammel and J.N. Cape. Nitrous acid and nitrite in the atmosphere. *Chem. Soc. Rev.*, 25:361–369, 1996. doi: 10.1039/CS9962500361.

P. J. Landrigan, R. Fuller, N. J. R. Acosta, O. Adeyi, R. Arnold, N. N. Basu, A. B. Baldé, R. Bertollini, V. Fuster, M. Greenstone, A. Haines, D. Hanrahan, D. Hunter, M. Khare,

A. Krupnick, B. Lanphear, B. Lohani, K. Martin, K. V. Mathiasen, M. A. Mcteer, C. J. L. Murray, J. D. Ndahimananjara, F. Perera, J. Potočnik, A. S. Preker, J. Ramesh, J. Rockström, C. Salinas, L. D. Samson, K. Sandilya, P. D. Sly, K. R. Smith, and A. Steiner. The Lancet Commissions The Lancet Commission on pollution and health. *The Lancet*, 391, 2018. doi: 10.1016/S0140-6736(17)32345-0.

S. Laufs, M. Cazaunau, P. Stella, R. Kurtenbach, P. Cellier, A. Mellouki, B. Loubet, and J. Kleffmann. Diurnal fluxes of HONO above a crop rotation. *Atmospheric Chemistry and Physics*, 17(11):6907–6923, 2017. ISSN 16807324. doi: 10.5194/acp-17-6907-2017.

Y. Li, J. An, M. Min, W. Zhang, F. Wang, and P. Xie. Impacts of HONO sources on the air quality in Beijing, Tianjin and Hebei Province of China. *Atmospheric Environment*, 45(27):4735–4744, 2011. ISSN 13522310. doi: 10.1016/j.atmosenv.2011.04.086.

M. Lippmann. Health effects of tropospheric ozone. *Environmental Science & Technology*, 25(12), 1991.

J. Liu, Z. Liu, Z. Ma, S. Yang, D. Yao, S. Zhao, B. Hu, G. Tang, J. Sun, M. Cheng, Z. Xu, and Y. Wang. Detailed budget analysis of HONO in Beijing, China: Implication on atmosphere oxidation capacity in polluted megacity. *Atmospheric Environment*, 244 (April 2020), 2021. ISSN 18732844. doi: 10.1016/j.atmosenv.2020.117957.

X. Liu, L. G. Huey, R. J. Yokelson, V. Selimovic, I. J. Simpson, M. Müller, J. L. Jimenez, P. Campuzano-Jost, A. J. Beyersdorf, D. R. Blake, Z. Butterfield, Y. Choi, J. D. Crounse, D. A. Day, G. S. Diskin, M. K. Dubey, E. Fortner, T. F. Hanisco, W. Hu, L. E. King, L. Kleinman, S. Meinardi, T. Mikoviny, T. B. Onasch, B. B. Palm, J. Peischl, I. B. Pollack, T. B. Ryerson, G. W. Sachse, A. J. Sedlacek, J. E. Shilling, S. Springston, J. M. St. Clair, D. J. Tanner, A. P. Teng, P. O. Wennberg, A. Wisthaler, and G. M. Wolfe. Airborne measurements of western U.S. wildfire emissions: Comparison with prescribed burning and air quality implications. *Journal of Geophysical Research*, 122(11):6108–6129, 2017. ISSN 21562202. doi: 10.1002/2016JD026315.

J. M. Lobert and J. Warnatz. Emissions from the combustion process in vegetation, 1993.

M. Maljanen, P. Yli-Pirilä, J. Hytönen, J. Joutsensaari, and P. J. Martikainen. Acidic northern soils as sources of atmospheric nitrous acid (HONO). *Soil Biology and Biochemistry*, 67(2):94–97, 2013. ISSN 00380717. doi: 10.1016/j.soilbio.2013.08.013.

J. Mao, X. Ren, S. Chen, W. H. Brune, Z. Chen, M. Martinez, H. Harder, B. Lefer, B. Rappenglück, J. Flynn, and M. Leuchner. Atmospheric oxidation capacity in the summer of Houston 2006: Comparison with summer measurements in other metropolitan studies. *Atmospheric Environment*, 44(33):4107–4115, 2010. ISSN 13522310. doi: 10.1016/j.atmosenv.2009.01.013.

J. R. Marlon, P. J. Bartlein, D. G. Gavin, C. J. Long, R. S. Anderson, C. E. Briles, K. J. Brown, D. Colombaroli, D. J. Hallett, M. J. Power, E. A. Scharf, and M. K. Walsh. Long-term perspective on wildfires in the western USA. *Proceedings of the National Academy of Sciences of the United States of America*, 109(9):535–543, 2012. ISSN 00278424. doi: 10.1073/pnas.1112839109.

A. A. May, G. R. McMeeking, T Lee, J. W. Taylor, J. S. Craven, I. R. Burling, Amy P. Sullivan, S. K. Akagi, Jeffrey L. Collett, M. Flynn, H. Coe, S. P. Urbanski, J. H. Seinfeld, R. J. Yokelson, and Sonia M. Kreidenweis. Aerosol emissions from prescribed fires in the United States: A synthesis of laboratory and aircraft measurements. *Journal of Geophysical Research*, 119, 2014. ISSN 2169897X. doi: 10.1002/2014JD021848.

J. L. McCarty, S. Korontzi, C. O. Justice, and T. Loboda. The spatial and temporal distribution of crop residue burning in the contiguous United States. *Science of the Total Environment*, 407(21):5701–5712, 2009. ISSN 00489697. doi: 10.1016/j.scitotenv.2009.07.009.

C. D. McClure and D. A. Jaffe. US particulate matter air quality improves except in wildfire-prone areas. *Proceedings of the National Academy of Sciences of the United States of America*, 115(31):7901–7906, 2018. ISSN 10916490. doi: 10.1073/pnas.1804353115.

H. Meusel, A. Tamm, U. Kuhn, D. Wu, A. Lena Leifke, S. Fiedler, N. Ruckteschler, P. Yordanova, N. Lang-Yona, M. Pöhlker, J. Lelieveld, T. Hoffmann, U. Pöschl, H. Su, B. Weber, and Y. Cheng. Emission of nitrous acid from soil and biological soil crusts represents an important source of HONO in the remote atmosphere in Cyprus. *Atmospheric Chemistry and Physics*, 18(2):799–813, 2018. ISSN 16807324. doi: 10.5194/acp-18-799-2018.

K. E. Min, R. A. Washenfelder, W. P. Dubé, A. O. Langford, P. M. Edwards, K. J. Zarzana, J. Stutz, K. Lu, F. Rohrer, Y. Zhang, and S. S. Brown. A broadband cavity enhanced absorption spectrometer for aircraft measurements of glyoxal, methylglyoxal, nitrous acid, nitrogen dioxide, and water vapor. *Atmospheric Measurement Techniques*, 9(2):423–440, 2016. ISSN 18678548. doi: 10.5194/amt-9-423-2016.

M. E. Monge, B. D'Anna, and C. George. Nitrogen dioxide removal and nitrous acid formation on titanium oxide surfaces-an air quality remediation process? *Physical Chemistry Chemical Physics*, 12(31):8991–8998, 2010. ISSN 14639076. doi: 10.1039/b925785c.

J. A. Neuman, T. B. Ryerson, L. G. Huey, R. Jakoubek, J. B. Nowak, C. Simons, and F. C. Fehsenfeld. Calibration and evaluation of nitric acid and ammonia permeation tubes by UV optical absorption. *Environmental Science and Technology*, 37(13):2975–2981, 2003. ISSN 0013936X. doi: 10.1021/es026422l.

J. A. Neuman, M. Trainer, S. S. Brown, K. E. Min, J. B. Nowak, D. D. Parrish, J. Peischl, I. B. Pollack, J. M. Roberts, T. B. Ryerson, and P. R. Veres. HONO emission and production determined from airborne measurements over the Southeast U.S. *Journal of Geophysical Research*, 121(15):9237–9250, 2016. ISSN 21562202. doi: 10.1002/2016JD025197.

R. Oswald, T. Behrendt, M. Ermel, D. Wu, H. Su, Y. Cheng, C. Breuninger, A. Moravek, E. Mougin, C. Delon, B. Loubet, A. Pommerening-Röser, M. Sörgel, U. Pöschl, T. Hoffmann, M. O. Andreae, F. X. Meixner, and I. Trebs. HONO emissions from soil bacteria as a major source of atmospheric reactive nitrogen. *Science*, 341(6151):1233–1235, sep 2013. ISSN 1095-9203. doi: 10.1126/science.1242266.

R. D. Ottmar, D. V. Sandberg, C. L. Riccardi, and S. J. Prichard. An overview of the Fuel Characteristic Classification System - Quantifying, classifying, and creating fuelbeds for resource planning. *Canadian Journal of Forest Research*, 37(12):2383–2393, 2007. ISSN 00455067. doi: 10.1139/X07-077.

S. A. Parks, C. Miller, M. A. Parisien, L. M. Holsinger, S. Z. Dobrowski, and J. Abatzoglou. Wildland fire deficit and surplus in the western United States, 1984-2012. *Ecosphere*, 6 (12):1–13, 2015. ISSN 21508925. doi: 10.1890/ES15-00294.1.

Q. Peng, B. B. Palm, K. E. Melander, B. H. Lee, S. R. Hall, K. Ullmann, T. Campos, A. J. Weinheimer, E. C. Apel, R. S. Hornbrook, A. J. Hills, D. D. Montzka, F. Flocke, L. Hu, W. Permar, C. Wielgasz, J. Lindaas, I. B. Pollack, E. V. Fischer, T. H. Bertram, and J. A. Thornton. HONO Emissions from Western U.S. Wildfires Provide Dominant Radical Source in Fresh Wildfire Smoke. *Environmental Science and Technology*, 54(10): 5954–5963, 2020. ISSN 15205851. doi: 10.1021/acs.est.0c00126.

J. N. Pitts, E. Sanhueza, R. Atkinson, W. P. L. Carter, A. M. Winer, G. W. Harris, and C. N. Plum. An investigation of the dark formation of nitrous acid in environmental chambers. *International Journal of Chemical Kinetics*, 16:919–939, 1984. doi: 10.1002/kin.550160712.

U. Platt and D. Perner. Simultaneous Measurement of Atmospheric CH_2O, O_3, and NO_2 by Differential Optical Absorption. *Journal of Geophyscal Research*, 84:6329–6335, 1979.

U. Platt and J. Stutz. *Differential Optical Absorption Spectroscopy*. Physics of Earth and Space Environments. Springer Berlin Heidelberg, Berlin, Heidelberg, 2008. ISBN 978-3-540-21193-8. doi: 10.1007/978-3-540-75776-4.

I. B. Pollack, B. M. Lerner, and T. B. Ryerson. Evaluation of ultraviolet light-emitting diodes for detection of atmospheric NO2 by photolysis - Chemiluminescence. *Journal of*

Atmospheric Chemistry, 65(2-3):111–125, 2010. ISSN 01677764. doi: 10.1007/s10874-011-9184-3.

G. Pouliot, V. Rao, J. L. McCarty, and A. Soja. Development of the crop residue and rangeland burning in the 2014 National Emissions Inventory using information from multiple sources. *Journal of the Air and Waste Management Association*, 67(5):613–622, 2017. ISSN 21622906. doi: 10.1080/10962247.2016.1268982.

T. A. M. Pugh, M. Cain, J. Methven, O. Wild, S. R. Arnold, E. Real, K. S. Law, K. M. Emmerson, S. M. Owen, J. A. Pyle, C. N. Hewitt, and A. R. MacKenzie. A Lagrangian model of air-mass photochemistry and mixing using a trajectory ensemble: The Cambridge Tropospheric Trajectory model of Chemistry And Transport (CiTTyCAT) version 4.2. *Geoscientific Model Development*, 5(1):193–221, 2012. ISSN 1991959X. doi: 10.5194/gmd-5-193-2012.

S. E. Pusede, T. C. VandenBoer, J. G. Murphy, M. Z. Markovic, C. J. Young, P. R. Veres, J. M. Roberts, R. A. Washenfelder, S. S. Brown, X. Ren, C. Tsai, J. Stutz, W. H. Brune, E. C. Browne, P. J. Wooldridge, A. R. Graham, R. Weber, A. H. Goldstein, S. Dusanter, S. M. Griffith, P. S. Stevens, B. L. Lefer, and R. C. Cohen. An Atmospheric Constraint on the NO 2 Dependence of Daytime Near-Surface Nitrous Acid (HONO). *Environmental Science and Technology*, 49(21):12774–12781, 2015. ISSN 15205851. doi: 10.1021/acs.est.5b02511.

K. A. Ramazan, D. Syomin, and B. J. Finlayson-Pitts. The photochemical production of HONO during the heterogeneous hydrolysis of NO2. *Physical Chemistry Chemical Physics*, 6(14):3836–3843, 2004. ISSN 14639076. doi: 10.1039/b402195a.

X. Ren, H. Harder, M. Martinez, R. L. Lesher, A. Oliger, T. Shirley, J. Adams, J. B. Simpas, and W. H. Brune. HOx concentrations and OH reactivity observations in New York City during PMTACS-NY2001. *Atmospheric Environment*, 37(26):3627–3637, 2003. ISSN 13522310. doi: 10.1016/S1352-2310(03)00460-6.

X. Ren, J. E. Sanders, A. Rajendran, R. J. Weber, A. H. Goldstein, S. E. Pusede, E. C. Browne, K.-E. Min, and R. C. Cohen. A relaxed eddy accumulation system for measuring vertical fluxes of nitrous acid. *Atmospheric Measurement Techniques*, 4(10):2093–2103, 2011. ISSN 1867-8548. doi: 10.5194/amt-4-2093-2011.

D. Richter, P. Weibring, J. G. Walega, A. Fried, S. M. Spuler, and M. S. Taubman. Compact highly sensitive multi-species airborne mid-IR spectrometer. *Applied Physics B: Lasers and Optics*, 119(1):119–131, 2015. ISSN 09462171. doi: 10.1007/s00340-015-6038-8.

J. M. Roberts, P. Veres, C. Warneke, J. A. Neuman, R. A. Washenfelder, S. S. Brown, M. Baasandorj, J. B. Burkholder, I. R. Burling, T. J. Johnson, R. J. Yokelson, and J. de Gouw. Measurement of HONO, HNCO, and other inorganic acids by negative-ion proton-transfer chemical-ionization mass spectrometry (NI-PT-CIMS): application to biomass burning emissions. *Atmospheric Measurement Techniques*, 3(4):981–990, 2010. ISSN 1867-8548. doi: 10.5194/amt-3-981-2010.

J. M. Roberts, C. E. Stockwell, R. J. Yokelson, J. De Gouw, Y. Liu, V. Selimovic, A. R. Koss, K. Sekimoto, M. M. Coggon, B. Yuan, K. J. Zarzana, S. S. Brown, C. Santin, S. H. Doerr, and C. Warneke. The nitrogen budget of laboratory-simulated western US wildfires during the FIREX 2016 Fire Lab study. *Atmospheric Chemistry and Physics*, 20(14):8807–8826, 2020. ISSN 16807324. doi: 10.5194/acp-20-8807-2020.

M. A. Robinson, Z. C. J. Decker, K. C. Barsanti, M. M. Coggon, F. M. Flocke, A. Franchin, C. D. Fredrickson, J. B. Gilman, G. I. Gkatzelis, C. D. Holmes, A. Lamplugh, A. Lavi, A. M. Middlebrook, D. M. Montzka, B. B. Palm, J. Peischl, B. Pierce, R. H. Schwantes, K. Sekimoto, V. Selimovic, G. S. Tyndall, J. A. Thornton, P. Van Rooy, C. Warneke, A. J. Weinheimer, and S. S. Brown. Variability and Time of Day Dependence of Ozone Photochemistry in Western Wildfire Plumes. *Environmental Science and Technology*, 55 (15):10280–10290, 2021. ISSN 15205851. doi: 10.1021/acs.est.1c01963.

A. W. Rollins, P. S. Rickly, R. S. Gao, T. B. Ryerson, S. S. Brown, J. Peischl, and I. Bourgeois. Single-photon laser-induced fluorescence detection of nitric oxide at sub-parts-per-trillion mixing ratios. *Atmospheric Measurement Techniques*, 13(5):2425–2439, 2020. ISSN 18678548. doi: 10.5194/amt-13-2425-2020.

T. B. Ryerson, A. E. Andrews, W. M. Angevine, T. S. Bates, C. A. Brock, B. Cairns, R. C. Cohen, O. R. Cooper, J. A. De Gouw, F. C. Fehsenfeld, R. A. Ferrare, M. L. Fischer, R. C. Flagan, A. H. Goldstein, J. W. Hair, R. M. Hardesty, C. A. Hostetler, J. L. Jimenez, A. O. Langford, E. McCauley, S. A. McKeen, L. T. Molina, A. Nenes, S. J. Oltmans, D. D. Parrish, J. R. Pederson, R. B. Pierce, K. Prather, P. K. Quinn, J. H. Seinfeld, C. J. Senff, A. Sorooshian, J. Stutz, J. D. Surratt, M. Trainer, R. Volkamer, E. J. Williams, and S. C. Wofsy. The 2010 California Research at the Nexus of Air Quality and Climate Change (CalNex) field study. *Journal of Geophysical Research Atmospheres*, 118(11):5830–5866, 2013. ISSN 21698996. doi: 10.1002/jgrd.50331.

F. Sakamaki, S. Hatakeyama, and H. Akimoto. Formation of nitrous acid and nitric oxide in the heterogeneous dark reaction of nitrogen dioxide and water vapor in a smog chamber. *International Journal of Chemical Kinetics*, 15:1013–1029, 1983. doi: 10.1002/kin.550151006.

A. Sandu and R. Sander. Technical Note: Simulating Chemical Systems in Fortran90 and Matlab with the Kinetic PreProcessor KPP-2.1. *Atmospheric Chemistry and Physics*, 6 (1):187–195, 2006. ISSN 1680-7316. doi: https://doi.org/10.5194/acp-6-187-2006.

G. Sarwar, S. J. Roselle, R. Mathur, W. Appel, R. L. Dennis, and B. Vogel. A comparison of CMAQ HONO predictions with observations from the Northeast Oxidant and Particle Study. *Atmospheric Environment*, 42(23):5760–5770, 2008. ISSN 13522310. doi: 10.1016/j.atmosenv.2007.12.065.

N. K. Scharko, U. M. E. Schütte, A. E. Berke, L. Banina, H. R. Peel, M. A. Donaldson, C. Hemmerich, J. R. White, and J. D. Raff. Combined Flux Chamber and Genomics

Approach Links Nitrous Acid Emissions to Ammonia Oxidizing Bacteria and Archaea in Urban and Agricultural Soil. *Environmental Science and Technology*, 49(23):13825–13834, 2015. ISSN 15205851. doi: 10.1021/acs.est.5b00838.

K. Sekimoto, A. R. Koss, J. B. Gilman, V. Selimovic, M. M. Coggon, K. J. Zarzana, B. Yuan, B. M. Lerner, S. S. Brown, C. Warneke, R. J. Yokelson, J. M. Roberts, and J. De Gouw. High-and low-temperature pyrolysis profiles describe volatile organic compound emissions from western US wildfire fuels. *Atmospheric Chemistry and Physics*, 18(13):9263–9281, 2018. ISSN 16807324. doi: 10.5194/acp-18-9263-2018.

R. E. Shetter and M. Müller. Photolysis frequency measurements using actinic flux spectroradiometry during the PEM-Tropics mission: Instrumentation description and some results. *Journal of Geophysical Research: Atmospheres*, 104(D5):5647–5661, 1999. ISSN 01480227. doi: 10.1029/98JD01381.

D. Simpson, C. Andersson, J. H. Christensen, M. Engardt, C. Geels, A. Nyiri, M. Posch, J. Soares, M. Sofiev, P. Wind, and J. Langner. Impacts of climate and emission changes on nitrogen deposition in Europe: A multi-model study. *Atmospheric Chemistry and Physics*, 14(13):6995–7017, 2014. ISSN 16807324. doi: 10.5194/acp-14-6995-2014.

R. J. D. Spurr. VLIDORT: A linearized pseudo-spherical vector discrete ordinate radiative transfer code for forward model and retrieval studies in multilayer multiple scattering media. *Journal of Quantitative Spectroscopy and Radiative Transfer*, 102(2):316–342, 2006. ISSN 00224073. doi: 10.1016/j.jqsrt.2006.05.005.

A. F. Stein, R. R. Draxler, G. D. Rolph, B. J.B. Stunder, M. D. Cohen, and F. Ngan. Noaa's hysplit atmospheric transport and dispersion modeling system. *Bulletin of the American Meteorological Society*, 96(12):2059–2077, 2015. ISSN 00030007. doi: 10.1175/BAMS-D-14-00110.1.

K. Stemmler, M. Ndour, Y. Elshorbany, J. Kleffmann, B. D'Anna, C. George, B. Bonn, and

M. Ammann. Light induced conversion of nitrogen dioxide into nitrous acid on submicron humic acid aerosol. *Atmospheric Chemistry and Physics*, 7(16):4237–4248, 2007. ISSN 16807324. doi: 10.5194/acp-7-4237-2007.

M. Stemmler, K.and Ammann, C. Donders, J. Kleffmann, and C. George. Photosensitized reduction of nitrogen dioxide on humic acid as a source of nitrous acid. *Nature*, 440(7081): 195–198, 2006. ISSN 14764687. doi: 10.1038/nature04603.

J. Stutz, B. Alicke, and A. Neftel. Nitrous acid formation in the urban atmosphere: Gradient measurements of NO2 and HONO over grass in Milan, Italy. *Journal of Geophysical Research Atmospheres*, 107(22), 2002. ISSN 01480227. doi: 10.1029/2001JD000390.

J. Stutz, H. J. Oh, S. I. Whitlow, C. Anderson, J. E. Dibb, J. H. Flynn, B. Rappenglück, and B. Lefer. Simultaneous DOAS and mist-chamber IC measurements of HONO in Houston, TX. *Atmospheric Environment*, 44(33):4090–4098, 2010. ISSN 13522310. doi: 10.1016/j.atmosenv.2009.02.003.

H. Su, Y. Cheng, R. Oswald, T. Behrendt, I. Trebs, F. X Meixner, M. O Andreae, P. Cheng, Y. Zhang, and U. Pöschl. Soil nitrite as a source of atmospheric HONO and OH radicals. *Science*, 333(6049):1616–1618, 2011. ISSN 1095-9203. doi: 10.1126/science.1207687.

R Svensson, E Ljungström, and O Lindqvist. Kinetics of the reaction between nitrogen dioxide and water vapour. *Atmospheric Environment*, 21(7):1529–1539, 1987. doi: 10.1016/0004-6981(87)90315-5.

N. Theys, R. Volkamer, J. F. Müller, K. J. Zarzana, N. Kille, L. Clarisse, I. De Smedt, C. Lerot, H. Finkenzeller, F. Hendrick, T. K. Koenig, C. F. Lee, C. Knote, H. Yu, and M. Van Roozendael. Global nitrous acid emissions and levels of regional oxidants enhanced by wildfires. *Nature Geoscience*, 13(10):681–686, 2020. ISSN 17520908. doi: 10.1038/s41561-020-0637-7.

J. L. Thomas, J. Stutz, B. Lefer, L. G. Huey, K. Toyota, J. E. Dibb, and R. von Glasow. Modeling chemistry in and above snow at Summit, Greenland – Part 1: Model description and results. *Atmospheric Chemistry and Physics*, 11(10):4899–4914, 2011. ISSN 1680-7324. doi: 10.5194/acp-11-4899-2011.

J. L. Thomas, J. E. Dibb, L. G. Huey, J. Liao, D. Tanner, B. Lefer, R. von Glasow, and J. Stutz. Modeling chemistry in and above snow at Summit, Greenland – Part 2: Impact of snowpack chemistry on the oxidation capacity of the boundary layer. *Atmospheric Chemistry and Physics*, 12(14):6537–6554, 2012. ISSN 1680-7324. doi: 10.5194/acp-12-6537-2012.

K. Toyota, A. P. Dastoor, and A. Ryzhkov. Air-snowpack exchange of bromine, ozone and mercury in the springtime Arctic simulated by the 1-D model PHANTAS - Part 2: Mercury and its speciation. *Atmospheric Chemistry and Physics*, 14(8):4135–4167, 2014. ISSN 16807324. doi: 10.5194/acp-14-4135-2014.

J. Trentmann, R. J. Yokelson, P. V. Hobbs, T. Winterrath, T. J. Christian, M. O. Andreae, and S. A. Mason. An analysis of the chemical processes in the smoke plume from a savanna fire. *Journal of Geophysical Research D: Atmospheres*, 110(12):1–20, 2005. ISSN 01480227. doi: 10.1029/2004JD005628.

S. Trick. *Formation of Nitrous Acid on Urban Surfaces - a physical chemical perspective*. PhD thesis, 2004. URL `https://lib.unnes.ac.id/17153/1/1201408017.pdf`.

C. Tsai, C. Wong, S. Hurlock, O. Pikelnaya, L. H. Mielke, H. D. Osthoff, J. H. Flynn, C. Haman, B. Lefer, J. Gilman, J. De Gouw, and J. Stutz. Nocturnal loss of NOx during the 2010 CalNex-LA study in the Los Angeles Basin. *Journal of Geophysical Research Atmospheres*, 119(22):13,004–13,025, 2014. ISSN 21698996. doi: 10.1002/2014JD022171.

C. Tsai, M. Spolaor, F. S. Colosimo, O. Pikelnaya, R. Cheung, E. Williams, J. B. Gilman, B. M. Lerner, R. J. Zamora, C. Warneke, J. M. Roberts, R. Ahmadov, J. De Gouw,

T. Bates, P. K. Quinn, and J. Stutz. Nitrous acid formation in a snow-free wintertime polluted rural area. *Atmospheric Chemistry and Physics*, 18(3):1977–1996, 2018. ISSN 16807324. doi: 10.5194/acp-18-1977-2018.

T. C. Vandenboer, S. S. Brown, J. G. Murphy, W. C. Keene, C. J. Young, A. A. P. Pszenny, S. Kim, C. Warneke, J. A. De Gouw, J. R. Maben, N. L. Wagner, T. P. Riedel, J. A. Thornton, D. E. Wolfe, W. P. Dubé, F. Öztürk, C. A. Brock, N. Grossberg, B. Lefer, B. Lerner, A. M. Middlebrook, and J. M. Roberts. Understanding the role of the ground surface in HONO vertical structure: High resolution vertical profiles during NACHTT-11. *Journal of Geophysical Research Atmospheres*, 118(17):10,155–10,171, 2013. ISSN 21698996. doi: 10.1002/jgrd.50721.

T. C. Vandenboer, C. J. Young, R. K. Talukdar, M. Z. Markovic, S. S. Brown, J. M. Roberts, and J. G. Murphy. Nocturnal loss and daytime source of nitrous acid through reactive uptake and displacement. *Nature Geoscience*, 8(1):55–60, 2015. ISSN 17520908. doi: 10.1038/ngeo2298.

P. R. Veres, J. M. Roberts, C. Warneke, D. Welsh-Bon, M. Zahniser, S. Herndon, R. Fall, and J. de Gouw. Development of negative-ion proton-transfer chemical-ionization mass spectrometry (NI-PT-CIMS) for the measurement of gas-phase organic acids in the atmosphere. *International Journal of Mass Spectrometry*, 274(1-3):48–55, 2008. ISSN 13873806. doi: 10.1016/j.ijms.2008.04.032.

P. R. Veres, J. M. Roberts, I. R. Burling, C. Warneke, J. De Gouw, and R. J. Yokelson. Measurements of gas-phase inorganic and organic acids from biomass fires by negative-ion proton-transfer chemical-ionization mass spectrometry. *Journal of Geophysical Research Atmospheres*, 115(23):1–15, 2010. ISSN 01480227. doi: 10.1029/2010JD014033.

P. R. Veres, J. M. Roberts, A. K. Cochran, J. B. Gilman, W. C. Kuster, J. S. Holloway, M. Graus, J. Flynn, B. Lefer, C. Warneke, and J. De Gouw. Evidence of rapid production

of organic acids in an urban air mass. *Geophysical Research Letters*, 38(17):1–5, 2011. ISSN 00948276. doi: 10.1029/2011GL048420.

P. R. Veres, J. M. Roberts, R. J. Wild, P. M. Edwards, S. S. Brown, T. S. Bates, P. K. Quinn, J. E. Johnson, R. J. Zamora, and J. De Gouw. Peroxynitric acid (HO2NO2) measurements during the UBWOS 2013 and 2014 studies using iodide ion chemical ionization mass spectrometry. *Atmospheric Chemistry and Physics*, 15(14):8101–8114, 2015. ISSN 16807324. doi: 10.5194/acp-15-8101-2015.

G. Villena, J. Kleffmann, R. Kurtenbach, P. Wiesen, E. Lissi, M. A. Rubio, G. Croxatto, and B. Rappenglück. Vertical gradients of HONO, NOx and O3 in Santiago de Chile. *Atmospheric Environment*, 45(23):3867–3873, 2011. ISSN 13522310. doi: 10.1016/j.atmosenv.2011.01.073.

B. Vogel, H. Vogel, J. Kleffmann, and R. Kurtenbach. Measured and simulated vertical profiles of nitrous acid - Part II. Model simulations and indications for a photolytic source. *Atmospheric Environment*, 37(21):2957–2966, 2003. ISSN 13522310. doi: 10.1016/S1352-2310(03)00243-7.

R. Volkamer, P. Sheehy, L. T. Molina, and M. J. Molina. Oxidative capacity of the Mexico City atmosphere-Part 1: A radical source perspective. *Atmospheric Chemistry and Physics*, 10(14):6969–6991, 2010. ISSN 16807316. doi: 10.5194/acp-10-6969-2010.

R. von Glasow, R. Sander, A. Bott, and P.J. Crutzen. Modeling halogen chemistry in the marine boundary layer 2. Interactions with sulfur and the cloud-covered MBL. *Journal of Geophysical Research*, 107(D17):4323, 2002a. ISSN 0148-0227. doi: 10.1029/2001JD000943.

R. von Glasow, R.and Sander, A. Bott, and P. J. Crutzen. Modeling halogen chemistry in the marine boundary layer 1. Cloud-free MBL. *Journal of Geophysical Research*, 107 (D17):4341, 2002b. ISSN 0148-0227. doi: 10.1029/2001JD000942.

S. Wang, M. M. Coggon, G. I. Gkatzelis, C. Warneke, I. Bourgeois, T. Ryerson, J. Peischl, P. R. Veres, J. A. Neuman, J. Hair, T. Shingler, M. Fenn, G. Diskin, L. G. Huey, Y. R. Lee, E. C. Apel, R. S. Hornbrook, A. J. Hills, S. R. Hall, K. Ullmann, M. M. Bela, M. K. Trainer, R. Kumar, J. J. Orlando, F. M. Flocke, and L. K. Emmons. Chemical Tomography in a Fresh Wildland Fire Plume: A Large Eddy Simulation (LES) Study. *Journal of Geophysical Research: Atmospheres*, 126(18):1–21, 2021. ISSN 21698996. doi: 10.1029/2021JD035203.

J. X. Warner, Z. Wei, L. L. Strow, C. D. Barnet, L. C. Sparling, G. Diskin, and G. Sachse. Improved agreement of AIRS tropospheric carbon monoxide products with other EOS sensors using optimal estimation retrievals. *Atmospheric Chemistry and Physics*, 10(19): 9521–9533, 2010. ISSN 16807316. doi: 10.5194/acp-10-9521-2010.

R. A. Washenfelder, N. L. Wagner, W. P. Dube, and S. S. Brown. Measurement of atmospheric ozone by cavity ring-down spectroscopy. *Environmental Science and Technology*, 45(7):2938–2944, 2011. ISSN 0013936X. doi: 10.1021/es103340u.

A. L. R. Westerling. Increasing western US forest wildfire activity: Sensitivity to changes in the timing of spring. *Philosophical Transactions of the Royal Society B: Biological Sciences*, 371(1696), 2016. ISSN 14712970. doi: 10.1098/rstb.2015.0178.

E. B. Wiggins, B. E. Anderson, M. D. Brown, P. Campuzano-Jost, G. Chen, J. Crawford, E. C. Crosbie, J. Dibb, J. P. DiGangi, G. S. Diskin, M. Fenn, F. Gallo, E. M. Gargulinski, H. Guo, J. W. Hair, H. S. Halliday, C. Ichoku, J. L. Jimenez, C. E. Jordan, J. M. Katich, J. B. Nowak, A. E. Perring, C. E. Robinson, K. J. Sanchez, M. Schueneman, J. P. Schwarz, T. J. Shingler, M. A. Shook, A. J. Soja, C. E. Stockwell, K. L. Thornhill, K. R. Travis, C. Warneke, E. L. Winstead, L. D. Ziemba, and R. H. Moore. Reconciling Assumptions in Bottom-Up and Top-Down Approaches for Estimating Aerosol Emission Rates From Wildland Fires Using Observations From FIREX-AQ. *Journal of Geophysical Research: Atmospheres*, 126(24), 2021. ISSN 21698996. doi: 10.1029/2021JD035692.

A. P. Williams, J. T. Abatzoglou, A. Gershunov, J. Guzman-Morales, D. A. Bishop, J. K. Balch, and D. P. Lettenmaier. Observed Impacts of Anthropogenic Climate Change on Wildfire in California. *Earth's Future*, 7(8):892–910, 2019. ISSN 23284277. doi: 10.1029/2019EF001210.

G. M. Wolfe, M. R. Marvin, S. J. Roberts, K. R. Travis, and J. Liao. The framework for 0-D atmospheric modeling (F0AM) v3.1. *Geoscientific Model Development*, 9(9):3309–3319, 2016. ISSN 19919603. doi: 10.5194/gmd-9-3309-2016.

K. W. Wong, H.-J. Oh, B. L. Lefer, B. Rappenglück, and J. Stutz. Vertical profiles of nitrous acid in the nocturnal urban atmosphere of Houston, TX. In *Atmospheric Chemistry and Physics*, volume 11, pages 3595–3609, apr 2011. doi: 10.5194/acp-11-3595-2011.

K. W. Wong, C. Tsai, B. Lefer, C. Haman, N. Grossberg, W. H. Brune, X. Ren, W. Luke, and J. Stutz. Daytime HONO vertical gradients during SHARP 2009 in Houston, TX. *Atmospheric Chemistry and Physics*, 12(2):635–652, 2012. ISSN 16807316. doi: 10.5194/acp-12-635-2012.

K. W. Wong, C. Tsai, B. Lefer, N. Grossberg, and J. Stutz. Modeling of daytime HONO vertical gradients during SHARP 2009. *Atmospheric Chemistry and Physics*, 13(7):3587–3601, 2013. ISSN 16807324. doi: 10.5194/acp-13-3587-2013.

L. Xu, J. D. Crounse, K. T. Vasquez, H. Allen, P. O. Wennberg, I. Bourgeois, S. S. Brown, P. Campuzano-Jost, M. M. Coggon, J. H. Crawford, J. P. DiGangi, G. S. Diskin, A. Fried, E. M. Gargulinski, J. B. Gilman, G. I. Gkatzelis, H. Guo, J. W. Hair, S. R. Hall, H. A. Halliday, T. F. Hanisco, R. A. Hannun, C. D. Holmes, L. G. Huey, J. L. Jimenez, A. Lamplugh, Y. R. Lee, J. Liao, J. Lindaas, J. A. Neuman, J. B. Nowak, J. Peischl, D. A. Peterson, F. Piel, D. Richter, P. S. Rickly, M. A. Robinson, A. W. Rollins, T.s B. Ryerson, K. Sekimoto, V. Selimovic, T. Shingler, A. J. Soja, J. M. S. Clair, D. J. Tanner, K. Ullmann, P. R. Veres, J. Walega, C. Warneke, R. A. Washenfelder, P. Weibring, A. Wisthaler,

G. M. Wolfe, C. C. Womack, and R. J. Yokelson. Ozone chemistry in western U.S. wildfire plumes. *Science Advances*, 7(50), 2021. ISSN 23752548. doi: 10.1126/sciadv.abl3648.

C. Ye, H. Gao, N. Zhang, and X. Zhou. Photolysis of nitric acid and nitrate on natural and artificial surfaces. *Environmental Science and Technology*, 50(7):3530–3536, 2016. ISSN 15205851. doi: 10.1021/acs.est.5b05032.

C. Ye, X. Zhou, D. Pu, J. Stutz, J. Festa, M. Spolaor, C. Tsai, C.r Cantrell, R. L. Mauldin, A. Weinheimer, R. S. Hornbrook, E. C. Apel, A. Guenther, L. Kaser, B. Yuan, T. Karl, J. Haggerty, S. Hall, K. Ullmann, J. Smith, and J. Ortega. Tropospheric HONO distribution and chemistry in the southeastern US. *Atmospheric Chemistry and Physics*, 18(12): 9107–9120, 2018. ISSN 16807324. doi: 10.5194/acp-18-9107-2018.

C. Ye, N. Zhang, H. Gao, and X. Zhou. Matrix effect on surface-catalyzed photolysis of nitric acid. *Scientific Reports*, (October 2018):1–10, 2019. ISSN 2045-2322. doi: 10.1038/s41598-018-37973-x.

R. J. Yokelson, S. P. Urbanski, E. L. Atlas, D. W. Toohey, E. C. Alvarado, J. D. Crounse, P. O. Wennberg, M. E. Fisher, C. E. Wold, T. L. Campos, K. Adachi, P. R. Buseck, and W. M. Hao. Emissions from forest fires near Mexico City. *Atmospheric Chemistry and Physics*, 7(21):5569–5584, 2007. ISSN 16807324. doi: 10.5194/acp-7-5569-2007.

R. J. Yokelson, J. D. Crounse, P. F. DeCarlo, T. Karl, S. Urbanski, E. Atlas, T. Campos, Y. Shinozuka, V. Kapustin, A. D. Clarke, A. Weinheimer, D. J. Knapp, D. D. Montzka, J. Holloway, P. Weibring, F. Flocke, W. Zheng, D. Toohey, P. O. Wennberg, C. Wiedinmyer, L. Mauldin, A. Fried, D. Richter, J. Walega, J. L. Jimenez, K. Adachi, P. R. Buseck, S. R. Hall, and R. Shetter. Emissions from biomass burning in the Yucatan. *Atmospheric Chemistry and Physics*, 9(15):5785–5812, 2009. ISSN 16807324. doi: 10.5194/acp-9-5785-2009.

C. J. Young, R. A. Washenfelder, J. M. Roberts, L. H. Mielke, H. D. Osthoff, C. Tsai,

O. Pikelnaya, J. Stutz, P. R. Veres, A. K. Cochran, T. C. VandenBoer, J. Flynn, N. Grossberg, C. L. Haman, B. Lefer, H. Stark, M. Graus, J. de Gouw, J. B. Gilman, W. C. Kuster, and S. S. Brown. Vertically resolved measurements of nighttime radical reservoirs in Los Angeles and their contribution to the urban radical budget. *Environmental Science & Technology*, 46(20):10965–10973, sep 2012. ISSN 0013-936X. doi: 10.1021/es302206a.

A. Yuan, B.and Koss, C. Warneke, J. B. Gilman, B. M. Lerner, H. Stark, and J. A. De Gouw. A high-resolution time-of-flight chemical ionization mass spectrometer utilizing hydronium ions (H3O+ ToF-CIMS) for measurements of volatile organic compounds in the atmosphere. *Atmospheric Measurement Techniques*, 9(6):2735–2752, 2016. ISSN 18678548. doi: 10.5194/amt-9-2735-2016.

N. Zhang, X. Zhou, P. B. Shepson, H. Gao, M. Alaghmand, and B. Stirm. Aircraft measurement of HONO vertical profiles over a forested region. *Geophysical Research Letters*, 36(15):1–5, 2009. ISSN 00948276. doi: 10.1029/2009GL038999.

N. Zhang, X. Zhou, S. Bertman, D. Tang, M. Alaghmand, P. B. Shepson, and M. A. Carroll. Measurements of ambient HONO concentrations and vertical HONO flux above a northern Michigan forest canopy. *Atmospheric Chemistry and Physics Discussions*, 12(3):7273–7304, mar 2012. ISSN 1680-7324. doi: 10.5194/acpd-12-7273-2012.

W. Zheng, F. M. Flocke, G. S. Tyndall, A. Swanson, J. J. Orlando, J. M. Roberts, L. G. Huey, and D. J. Tanner. Characterization of a thermal decomposition chemical ionization mass spectrometer for the measurement of peroxy acyl nitrates (PANs) in the atmosphere. *Atmospheric Chemistry and Physics*, 11(13):6529–6547, 2011. ISSN 16807316. doi: 10.5194/acp-11-6529-2011.

X. Zhou, K. Civerolo, H. Dai, G. Huang, J. Schwab, and K. Demerjian. Summertime nitrous acid chemistry in the atmospheric boundary layer at a rural site in New York State. *Journal of Geophysical Research Atmospheres*, 107(21):1–11, 2002. ISSN 01480227. doi: 10.1029/2001JD001539.

X. Zhou, H. Gao, Y. He, G. Huang, S. B. Bertman, K. Civerolo, and J. Schwab. Nitric acid photolysis on surfaces in low-NOx environments: Significant atmospheric implications. *Geophysical Research Letters*, 30(23), 2003. ISSN 00948276. doi: 10.1029/2003GL018620.

X. Zhou, G. Huang, K. Civerolo, U. Roychowdhury, and K. L. Demerjian. Summertime observations of HONO, HCHO, and O_3 at the summit of Whiteface Mountain, New York. *Journal of Geophysical Research*, 112:D08311, 2007. ISSN 0148-0227. doi: 10.1029/2006JD007256.

X. Zhou, N. Zhang, M. TerAvest, D. Tang, J. Hou, S. Bertman, M. Alaghmand, P. B. Shepson, M. A. Carroll, S. Griffith, S. Dusanter, and P. S. Stevens. Nitric acid photolysis on forest canopy surface as a source for tropospheric nitrous acid. *Nature Geoscience*, 4 (6):400–443, 2011. ISSN 1752-0894. doi: 10.1038/ngeo1164.